Applied Physics B (2024) 130:169
https://doi.org/10.1007/s00340-024-08273-2

Applied Physics B
Lasers and Optics

REVIEW

Fluorescence characteristics of organic tracer molecules for planar laser-induced fluorescence in internal combustion engines, Part B: aromatics

Soumyanil Nayek[1] · **Mayank Mittal**[1]

Received: 1 November 2023 / Accepted: 2 July 2024

Abstract
Tracer based planar laser-induced fluorescence (PLIF) has emerged as a powerful in-situ measurement technique with a considerable spatial and temporal resolution for Internal combustion (IC) engines. In PLIF, the emitted fluorescence signals from a tracer molecule are processed to determine distribution of temperature, fuel, residual gases, etc. However, it is imperative to have a thorough understanding of the tracer physical properties and its fluorescence intensity dependencies on excitation wavelength, pressure, temperature and bath gas composition existing inside the combustor for accurate quantitative interpretation. This work consists of a series of two articles providing a detailed review of the existing literature of fluorescence characteristics of various molecules used as tracers in IC engine applications. Due to the overwhelming usage of organic compounds in IC engine environment, the work is restricted to them. Part A of this work is focussed on non-aromatic compounds whereas part B will focus on aromatics (toluene, anisole, naphthalene, 1-methylnaphthalene and fluoranthene). Due to a large energy gap between the excited singlet and triplet states of aromatics, they are highly sensitive to oxygen quenching effects than ketones. Absorption cross-section might increase or decrease with temperature but is insensitive to pressure changes. Fluorescence quantum yield of aromatics show a very strong reduction with increase in temperature but might either increase or decrease with increasing pressure. The pressure sensitivity is found to increase with the number of atoms in a bath gas molecule. Fluorescence spectra are found to undergo redshift with temperature which can be used to measure temperature using 2 colour thermometry. The large fluorescence quenching by oxygen can also be used to directly measure fuel–air ratio using FARLIF methodology. Towards the end several IC engine studies are reviewed to discuss various aspects of mixture formation and temperature distribution.

1 Introduction

1.1 Motivation

Planar laser-induced fluorescence (PLIF) is a non-intrusive technique that uses fluorescent compounds called tracers to measure various parameters in complex flow situations, such as those inside an internal combustion engine cylinder. This method allows for accurate measurements of fuel distribution, exhaust residuals, and temperature without interfering with the flow field. This information is crucial for optimizing combustion to meet emission and fuel efficiency requirements. The effectiveness of PLIF depends on the behaviour of tracer molecules used. However, the fluorescence signals from the tracers are influenced by various factors in the combustion system. Fluorescence signals emitted from a particular region of space is dependent on the tracer concentration, pressure, temperature and composition of the surrounding gases, most of which are unknown in a typical combustion system. It is extremely challenging to measure all of them simultaneously as there is a lack of a-priori calibration data in all these dimensions. Therefore, the key question for all tracer LIF measurements is how to reduce the complexity of the system in a manner that is suitable for obtaining the desired information.

Understanding the physical properties of tracers and their fluorescence signal dependencies is essential. While a previous review has briefly discussed the fluorescence dependency of a handful of molecules at limited pressure and temperature regimes (either only high pressure or only high temperature)

✉ Mayank Mittal
mmittal@iitm.ac.in

[1] Department of Mechanical Engineering, Indian Institute of Technology, Madras, India

Published online: 02 September 2024

[1], this work provides a comprehensive review of various molecules, including discussions on simultaneous high-pressure and high-temperature conditions, which are particularly relevant for internal combustion engines and other combustor applications. Due to its extensive nature, the review work is divided into two parts. In the previous Part A, fluorescence behaviour of non-aromatic tracers (acetone, 3-pentanone, and biacetyl) were covered in detail. In the current article, i.e., Part B aromatic tracers (toluene, anisole, naphthalene, 1-methyl naphthalene, and fluoranthene) are discussed.

1.2 Background

With the advent of optical engines [2–5], optical access was now available inside the combustion chamber through transparent cylinder liner and piston window made of quartz. With optical access, many laser diagnostic techniques quickly became popular for in-cylinder measurements. The ability of PLIF to be species specific and to provide information with a high spatial resolution at a fair signal strength, resulted in it being an extremely popular method for fuel and temperature distribution measurement in IC engine diagnosis and other applications like gas turbine combustors [6] and various fundamental studies [7–10]. Measurements in IC engines are normally carried out in a linear regime where the emitted fluorescence signals are linearly proportional to the incident laser excitation energy. Assuming weak excitation, fluorescence signal (in photons per unit volume) can be calculated from the following equation that was explained by Koch and Hanson (2003) [11]:

$$S_{\mathrm{f}} = \eta_{\mathrm{opt}} \frac{E}{\frac{hc}{\lambda}} n_{\mathrm{abs}}(P,T)\sigma(\lambda,T)\varphi(\lambda,P,T) \tag{1}$$

where η_{opt} is collection optics efficiency, $\frac{hc}{\lambda}$ is the energy of a photon (in J) that is absorbed, E is the laser fluence (J/cm^2), c is the speed of light, λ is the wavelength of the laser light used, n_{abs} is the tracer number density (in molecules/cm^3) which is a function of pressure and temperature, σ is the absorption cross section (cm^2/molecule) which is a function of temperature and wavelength of light used, and ϕ (number of fluorescence photons per absorbed photon) is called the fluorescence quantum yield (FQY) which is a function of pressure, temperature, wavelength and composition of the surrounding gases.

Among these parameters, the absorption cross-section and fluorescence quantum yield are particularly significant in LIF (Laser-induced fluorescence) studies. The fluorescence quantum yield (ϕ) serves as a measure of the likelihood of a molecule in its excited state returning to its ground state by emitting a photon (in other words, undergoing fluorescence). In its excited state, a molecule will tend to revert back to the ground states either upon emission of a photon or by giving up energy in some non-radiative processes. The emitted signals from a sample when produced as a spectrum result in the fluorescence spectrum. When in the excited state, there are several pathways available to the molecule to give up the excess energy. Such pathways are shown in the Jablonski's diagram in Fig. 1. In the diagram, electronic states are demarcated by a numerical as a subscript depicting the degree of excitation along with an uppercase letter 'S' or 'T' referring to either singlet or the triplet state. The thick horizontal line represents the ground vibrational level of an electronic manifold whereas the thin horizontal lines are the higher vibrational levels. The various photophysical processes can be divided into unimolecular (intrinsic to the molecule) or bimolecular (depends on the concerned tracer molecule along with a collider molecule). Furthermore, the processes can also be classified as radiative or non-radiative. When a photon is emitted upon transition between energy states of similar multiplicity then it is called fluorescence,

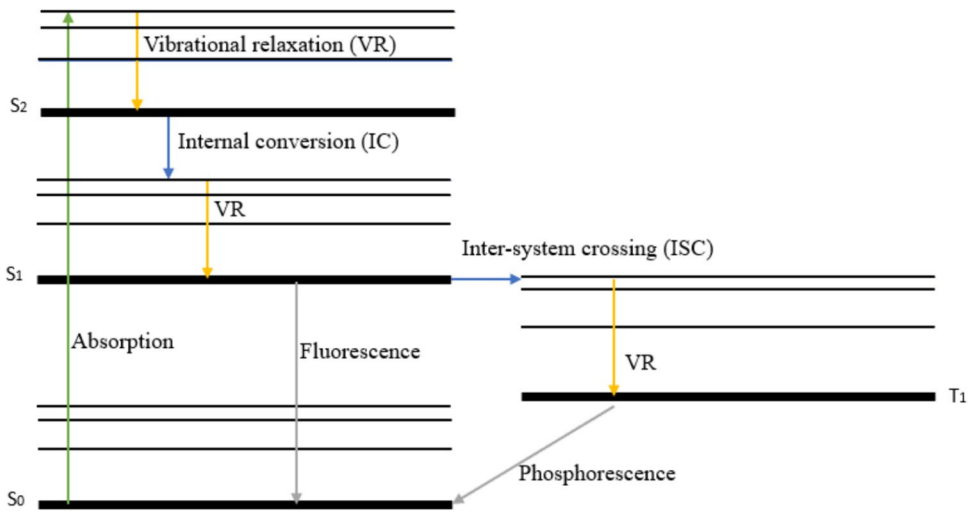

Fig. 1 Jablonski's diagram showing various photo-physical processes

when the multiplicity changes, it is called phosphorescence. In the diagram fluorescence (F) is shown between S_1 and S_0 states and phosphorescence occurs between T_1 and S_0 states. Absorption (A) is shown by a vertical arrow between S_0 and S_2. When the transition occurs without the emission of a photon between states of similar multiplicity then it is called internal conversion (IC) and when multiplicities are different then it is called inter-system crossing (ISC). In the diagram, IC is shown between S_2 and S_1 whereas ISC is shown between S_1 and T_1.

All the processes mentioned till now were intrinsic to the excited molecule and required no participation from any bath gas molecule. Apart from these unimolecular processes, there exists bimolecular pathways by which an excited molecule can give up energy and avoid fluorescence. This is called fluorescence quenching (not shown in the diagram). When an excited molecule and a bath gas molecule approach each other, they interact in a way so that the excited molecule loses energy and ends up in the ground singlet state thus effectively reducing the fluorescence yield. In addition, some collisions might only lead to relaxation of the excited molecules down the manifold. The vibrational energy lost due to several collisions with the surrounding bath gas molecules might manifest itself as a rise in kinetic energy of the collider species. This interaction is called vibrational relaxation (VR). VR in the diagram is shown by a transition to the lower vibrationally excited states in the S_1 state. It does not eliminate fluorescence as the molecule still remains in the excited singlet state unlike fluorescence quenching where the molecule ends up in the ground singlet reducing the fluorescence yield. These photophysical processes occurring in an excited state molecule are only briefly discussed in this article since these are discussed quite extensively in part-A of this work. For detailed discussion of these processes, one can refer [12–14]. To understand the importance of tracer molecules and their required characteristics, one can refer to part A of this work.

FQY is expressed as [15]:

$$\phi = \frac{k_{rad}}{k_t + \sum_i k_i q_i} \tag{2}$$

Here, k_{rad} represents fluorescence rate, $k_t (k_t = k_{rad} + k_{nr})$ is the summation of rates of all intramolecular deactivation processes occurring in the excited state molecule (k_{nr} represents non-radiative rate) and the summation term represents rate of collisional quenching (k_i) with different quencher molecules with concentration (q_i). Note that k_t and k_i have different units. In the absence of quenching, $\phi_0 = \frac{k_{rad}}{k_t}$. Since the intensity is proportional to FQY, therefore, $\frac{\phi}{\phi_0} = \frac{I}{I_0}$. Assuming, oxygen quenching is dominant among all other quenching mechanisms, the lifetime of an excited molecule can be approximated by a first order time constant expressed as:

$$\tau_{eff} = \frac{1}{k_t + k_{O_2} q_{O_2}} \tag{3}$$

Therefore, $\phi = \tau_{eff} \times k_{rad}$ (from Eq. (2)). In the absence of quenching, the lifetime reduces to $\tau_0 = \frac{1}{k_t}$. Expressing the signal ratios in terms of fluorescence lifetime value, we obtain [13]:

$$\frac{I_0}{I} = 1 + k_{SV} q_{O_2} \tag{4}$$

where k_{SV} is referred to as the Stern–Volmer coefficient. Mathematically,

$$k_{sv} = \frac{k_{O_2}}{k_f + k_{nr}} \tag{5}$$

The plots of $\frac{I}{I_0} - 1$ are referred to as Stern–Volmer plots and are important to study quenching as will be observed later. Incidentally, k_{SV} represents the relative strength of quenching with respect to other intramolecular deactivation processes. This will particularly be helpful to study the applicability of FARLIF (Fuel–air ratio LIF) [16] technique at certain conditions of temperatures and pressures. Mathematically FARLIF methodology is explained using Eq. (6) from the study of Koban et al. [17].

$$S_{\mathrm{fl}}\left(T, n_{\mathrm{oxy}}\right) \sim n_{\mathrm{tracer}}\, \sigma_{\mathrm{abs}}(T) \frac{k_{\mathrm{fl}}(T)}{k_{\mathrm{tot}}(T) + \widetilde{k}_{\mathrm{q}}^{\mathrm{oxy}}(T) n_{\mathrm{oxy}}} \sim g(T) \frac{n_{\mathrm{tracer}}}{n_{\mathrm{oxy}}} \tag{6}$$

If the oxygen quenching rate ($\widetilde{k}_{\mathrm{q}}^{\mathrm{oxy}}(T) n_{\mathrm{oxy}}$) far outweighs the sum of the fluorescence rate and the intramolecular deactivation rates ($k_{\mathrm{tot}}(T)$) in Eq. (6), then the fluorescence signal is directly proportional to the ratio of the tracer number density to the oxygen number density giving information about fuel–air ratio. The temperature term $g(T)$ arises from the various remaining temperature dependent terms like absorption cross-section, fluorescence rate and oxygen quenching rate constant. Required calibrations can be performed to evaluate $g(T)$ for various temperatures at a known fuel–air ratio which can then be used to correct the signals in the presence of appreciable spatial in-cylinder temperature variation.

1.3 Roadmap through the paper

This paper is organised as follows. After a brief discussion on PLIF and the relevant photophysical processes, the article immediately begins to discuss the fluorescence characteristics of the mentioned aromatic molecules. The molecules are classified into mono-, di- and poly-aromatic compounds.

Depending on their usage and the amount of literature available, a few molecules from each group were selected to be reviewed in this work. From mono-aromatics, toluene and anisole were chosen to represent the group and are separately discussed in Sects. 2 and 3 respectively. Section 4 covers di-aromatic molecules from which naphthalene and its methyl derivative 1-methylnaphthalene were selected for review. Section 5 aims to discuss fluorescence characteristics of a poly-aromatic molecule. Fluoranthene was chosen for this purpose; to the best of our knowledge, it is the only poly-aromatic compound which has found usage as a fluorescent tracer in IC engine along with an availability of literature on parametric study of fluorescence characteristics. However, this selection should not be treated as complete as there are various other molecules like triethylamine (TEA), difluoro benzene (DFB), 1,2,4-trimethyl benzene (TMB), N,N-dimethylaniline (DMA), etc., that could not be included in this work due to either lack of usage in IC engine studies or due to lack of studies in fluorescence characteristics. It is to be noted that a detailed discussion of the fluorescence models, their various parameters and optimisation is not a focus of this work. Interested readers can refer the original works cited here. Nonetheless, the model results and the physics behind them are explained here.

After bringing out the relevant photophysical processes that occur in the excited state of all the molecules, Sect. 6 discusses the various concepts involving PLIF of both aromatic and non-aromatic molecules for usage in in-situ measurement of temperature and fuel distribution inside IC engines. In it, techniques like in-situ calibration and FARLIF for fuel distribution imaging, whereas two tracer, two line and two-colour techniques for temperature imaging, are explained. At the end, a brief discussion about high-speed measurements is also provided. Various relevant PLIF studies are discussed to highlight the utility of these techniques in understanding various processes behind mixture formation in IC engines. The article is then concluded with the discussion of several key insights obtained in this work. A summary of physical properties of discussed tracers is provided in Table 1. It is to be noted that all the figures reported in this work for fluorescence signals and FQY values are obtained from studies which were performed at a constant tracer number density.

2 Toluene

Toluene is perhaps the most widely used aromatic tracer. Since aromatic compounds are present in a significant amount in the naturally occurring fuels, with a strong fluorescence signal and high susceptibility to oxygen quenching, a proper characteristic of their fluorescence signals offers some unique advantages which can be exploited to unveil detection schemes like the FARLIF technique. In unleaded gasoline toluene is present in a significant amount of 35% by vol [38] and in a small amount of 0.25–0.5% by vol in diesel [39]. Reboux et al. [16] suggested that if the oxygen quenching rate is very large as compared to the rates of all other deexcitation mechanisms, then the fluorescence signals become directly proportional to the fuel–air ratio. This method becomes particularly useful when the amount of oxygen present is small or the concentration of oxygen has high variation in the region of interest. The applicability of FARLIF for fuel–air ratio imaging has been demonstrated by various researchers [15, 40]. Reboux et al. [40] used FARLIF to investigate spatial inhomogeneity and cycle-to-cycle variation (CCV) of fuel–air ratio distribution in a PFI (port fuel injection) engine. They reported increased spatial inhomogeneities when injecting against an open intake valve or with cooled intake manifolds due to thick fuel film formation hindering vaporization. CCVs were also higher under these conditions. Sacadura et al. [41] utilized FARLIF to investigate mixture formation in both PFI and DI (direct injection) modes. In DI mode, two injection timings were tested: early injection during the intake stroke and late injection during the compression stroke to create a stratified mixture. In PFI mode, the mixture appeared spatially uniform, especially during the compression stroke, with fluorescence intensity increasing with equivalence ratio. A progressive flame front indicative of premixed combustion was observed, with flame speed increasing with overall equivalence ratio. In DI mode with early injection, a uniform fuel–air mixture was found

Table 1 Physical and thermodynamical properties of toluene, anisole, naphthalene, 1-methylnaphtahlene and fluoranthene

Physical properties	Toluene	Anisole	Naphthalene	1-methylnaphthalene	Fluoranthene
Molecular weight (g/mol)	92.1 [1]	108.13 [18]	128.17 [19]	142.2 [20]	202.25 [19]
Density (g/cc)	0.87 at 25 °C [1]	0.9956 at 18 °C [21]	1.162 at 20°C [22]	1.02 at 20°C [23]	1.252 at 0 °C [23]
Boiling point (°C)	110.6 [1]	155.5 [21]	218 [24]	245 [25]	384 [26]
Heat of vapourization at 25 °C (kJ/mol)	38 [27]	46.84 [28]	54.6 [29]	65.1 [30]	86.8 [31]
Heat of combustion (MJ/mol)	3.95 [1]	3.78 [28]	5.15 [32]	5.78 [33]	7.91 [34]
Vapour pressure @ (amb. temp.) (mbar)	29 [35]	3.6 [35]	0.024 [35]	0.09 [36]	1.23 [37]

due to longer mixing times, resulting in gradual flame front evolution resembling premixed combustion. However, late injection in DI mode led to highly stratified mixture distribution with significant CCV, characterized by unevaporated fuel droplets and rich mixture regions. Equivalence ratio in the vapor phase ranged from 0.3 to 2, indicating varying degrees of mixing. Flame images in DI mode lacked a distinct flame front, suggesting a diffusion flame, with regions exhibiting premixed flame or flamelets surrounding droplets. These flamelets gradually consumed the droplets as they evaporated, leading to diffusion flames and soot formation due to incomplete mixing. Frieden et al. [42] used toluene along with 3-pentanone for measurement of oxygen distribution in the cylinder of a gasoline direct injection engine. This method simultaneously determined the fuel number density and equivalence ratio distribution. Manipulating both the images provided oxygen distribution which is especially important when there is a high degree of recirculation of exhaust gas residuals. With the help of a number density balance, the exhaust gas amount inside the cylinder could be deduced.

Apart from measurement of fuel–air ratio, fluorescence signals from toluene can also be used to measure in-cylinder temperature. A very useful single laser two colour fluorescence thermometry was demonstrated by Luong et al. [43] using toluene as a tracer in a direct injection spark ignition engine. Willman et al. [44] studied the temperature distribution in an optical engine using two-colour thermometry and compared the cycle-to-cycle variation of temperature distribution for PFI and GDI modes using different blending ratios of toluene with iso-octane. Proper orthogonal decomposition (POD) was applied to quantify CCV and they found that GDI mode showed higher variability than the PFI mode in their particular engine configuration. Gessenhardt et al. [45] also performed temperature imaging using two-colour thermometry. They found that the temperature distribution is relatively uniform in the compression stroke, whereas in the intake stroke, the distribution was more non-uniform due to the presence of exhaust gas residuals and their mixing with the incoming fresh cooler charge. Similarly, Peterson et al. [46] performed two-colour thermometry using toluene to study the temperature evolution in the compression and expansions strokes. In the late compression stroke near TDC, the temperature distribution was mostly found to be homogeneous, whereas in the expansion stroke, some inhomogeneities were observed due to the appearance of cooler regions especially near the cylinder head and cylinder walls in the particular engine configuration. The cooler regions then were found to grow as the expansion stroke proceeds. Toluene also finds a wide usage in PLIF studies in diesel engines [47–52]. Many of these studies were carried out using a mixture of iso-octane and n-heptane as the surrogate fuel. For the success of these techniques, it is very important to have a thorough understanding of toluene fluorescence and its behaviour with changing pressure, temperature and bath gas composition under engine relevant conditions. This forms the subject matter of discussion in the following sections.

2.1 Absorption cross-section

Toluene is a single methyl substitution of a benzene ring and its molecular structure can be seen in Fig. 2. Toluene is the first of the aromatic compounds we are about to discuss. One of the fundamental differences in the absorption spectrum of ketones and aromatic compounds is the nature of the electronic transition. Whereas the transition in ketonic compounds is the $\mathbf{n} \rightarrow \boldsymbol{\pi}^*$, the transition in aromatic compounds is $\boldsymbol{\pi} \rightarrow \boldsymbol{\pi}^*$. An electron from the delocalized bonding orbital of a carbon–carbon group is excited to the anti-bonding orbital. This results in a significantly higher absorption cross-sections [53] of aromatic molecules than their ketonic counterparts. Toluene has an absorption cross-section which ranges from about 240–290 nm for the S_0 to S_1 transition, (Fig. 2) [54]. At temperatures less than 600 K, the absorption spectrum of toluene shows several features that vanish at higher temperatures. Koban et al. [54] performed experiments for absorption cross-section measurements in both a shock tube and in a constant volume chamber. For the shock tube, the measurements were in a temperature range of 600–1200 K and a pressure range of 0.9–2.4 bar. Whereas, in the flow cell, temperature range was between room temperature and 950 K at atmospheric pressure.

Toluene absorption spectrum is found to increase in strength and broaden with increasing temperature. The results of [54] is compared with Burton and Noyes (1968)

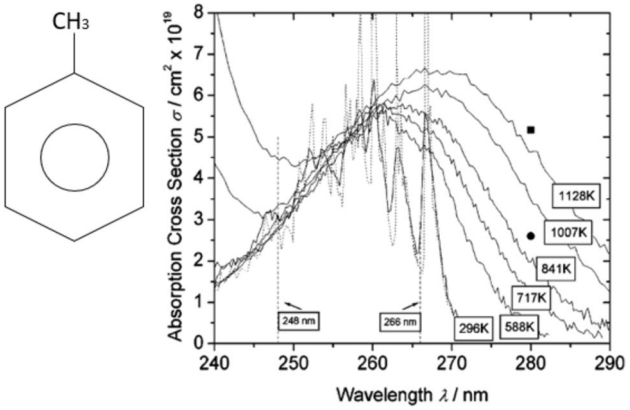

Fig. 2 Schematic diagram of toluene molecule is shown in the left image. The right image shows the absorption cross-section from the works of Koban et al. (2004) [54]. Circle represents data at 800 K and square is at 1200 K Hippler et al. [55]. Dotted lines represent room temperature absorption spectrum from the works of Burton and Noyes [56]. Adapted from [54] with permission from the Royal Society of Chemistry

[56] which is represented as dotted lines in Fig. 2 and are explained here. Two of the most common laser wavelengths used for toluene are 248 and 266 nm. These wavelengths are indicated by vertical dotted lines. The spectrum is quite insensitive to pressure changes. The temperature broadening effect also results in the loss of features in absorption spectrum at higher temperatures. The maxima is found to shift towards longer wavelengths and is found at 268 nm at 1125 K. The Full width at half maximum (FWHM) increases from 20 nm at 600 K to 40 nm at 1100 K due to the broadening effect. Another important phenomenon that can be observed is the stronger symmetry allowed S_0 to S_2 transition which is found to grow and broaden with temperature so much so that it merges with S_0 to S_1 transition at significantly higher temperatures in the shorter wavelength region. The longer wavelengths thus show a significant increase with temperature whereas the shorter wavelengths are highly temperature insensitive until the merging of S_0 to S_2 transition after which, they are expected to show a considerable increase in magnitude.

Figure 3 [54] shows the temperature variation of absorption cross-section for the 248 and 266 nm wavelengths. Previous work of Richardson et al. [57] closely match for 248 nm and are systematically lower for 266 nm whereas Burton and Noyes values are consistent. Cross-section for 248 nm show a temperature independence till 950 K. Thus, the cross-section value for 248 nm is constant with a value of $3.1 \pm 0.2 \times 10^{-19}$ cm^2. After 1000 K, there is a steep increase in the cross-section value due to a gradual merging with the S_0 to S_2 transition. Cross-section for 266 nm shows a linear increase with temperature in a range of 300–550 K by a factor of 2.5. After 550 K, the increase becomes slow. The room temperature cross-section value for 266 nm lies in a minima region near the peak of 266.8 nm (Fig. 2). With rising temperature, the profile broadens leading to an initial linear increase. However, after 550 K, the features in spectrum vanish and the further slower rise is mainly due to the overall growth and broadening of the spectrum. Similar results were also obtained by Wermuth and Sick [58] who used a small bore motored optical engine to study the absorption cross-section of toluene in the temperature range of 300–650 K. They reported a temperature independence of absorption cross-section for 248 nm in the studied temperature range and a steady increase for 266 nm which after 600 K shows temperature insensitivity within experimental scatter. The redshift with temperature can be explained as molecules in the ground state occupying higher vibrational energy levels at higher temperature reducing the energy needed for transition into the excited electronic state. The overall growth of the spectrum can be explained as improved Franck–Condon factors arising due to deviation from perfect symmetry conditions at higher temperatures. These are similar behaviour to the ketonic counterparts.

2.2 Fluorescence signal variation

Figure 4 shows the fluorescence spectrum of toluene in a nitrogen bath gas at a total pressure of 1 bar following an excitation of 248 nm. At room temperature, the spectrum extends from 260 to 400 nm with a maximum at 280 nm. Figure 4 also shows the temperature dependence of spectrum. Since the signal strength decreases with temperature, respective spectra are normalised to their maximum values to compare the relative shapes. With increasing temperature,

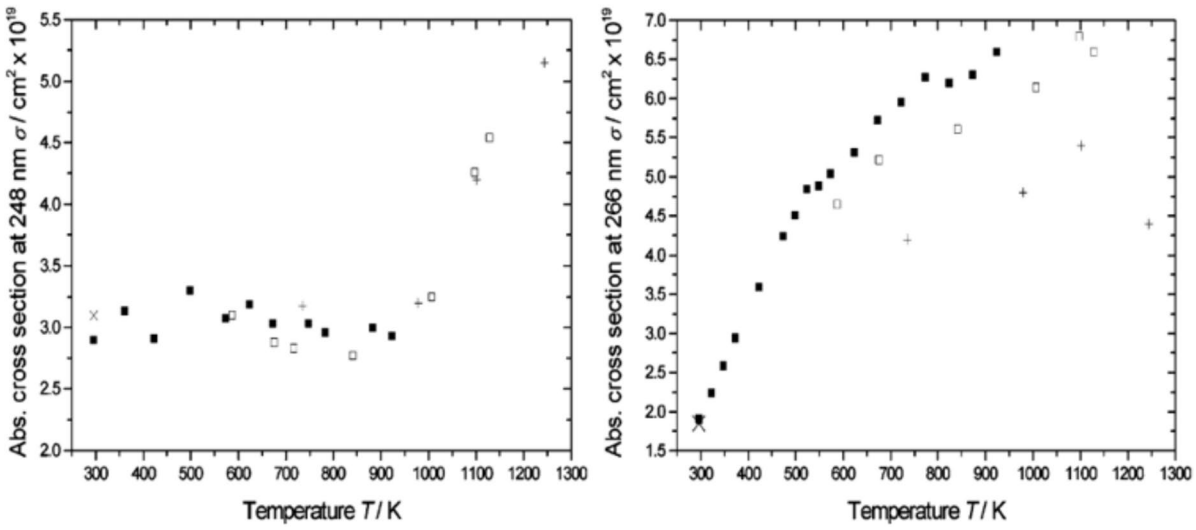

Fig. 3 (from ref [54]) Plots showing the dependence of absorption cross-section with temperature for toluene at 248 nm (left image) and 266 nm (right image). Filled squares represent flow cell data, hollow squares represent shock tube data, 'plus' signs are from Richardson et al. [57] and 'cross' signs are from Burton and Noyes [56]. Adapted from [54] with permission from the Royal Society of Chemistry

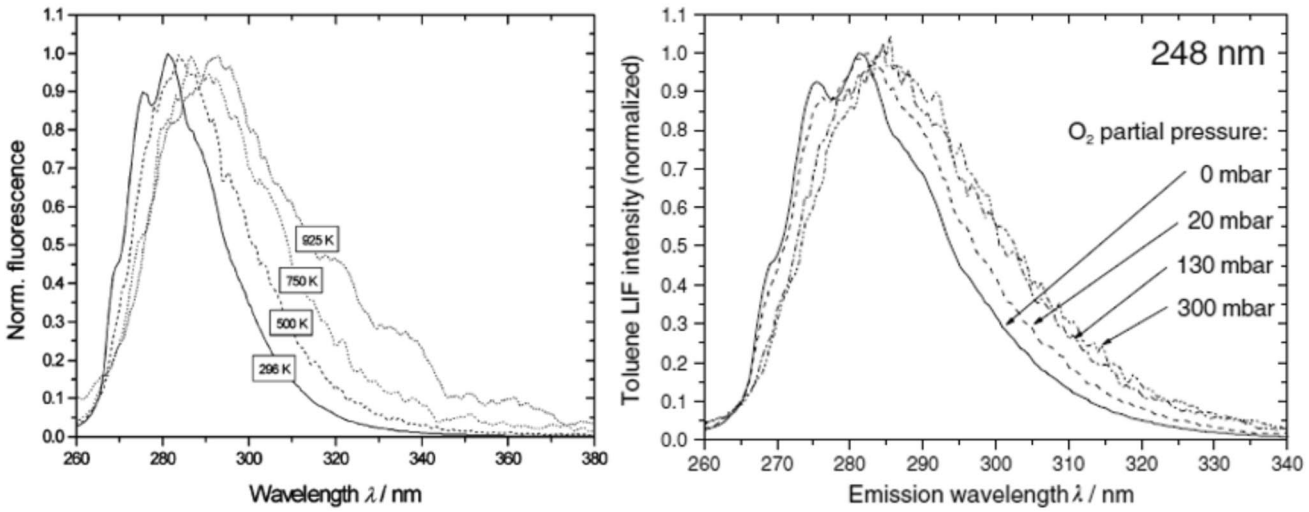

Fig. 4 Left image [54] shows the temperature dependence of fluorescence spectrum. Adapted from [54] with permission from the Royal Society of Chemistry. Right image [59] shows the oxygen partial pressure dependence. Both the spectra were obtained at 248 nm excitation at 1 bar total pressure

a redshift is observed for about 2 nm per 100 K with an apparent red-shifting of the fluorescence peak. The tail end of the spectra becomes stronger with temperature with respect to the peak. The fluorescence spectra is more broadband than the absorption spectra. The observed features at higher temperature is due to noise as the signal levels are very low at these temperatures. The fluorescence spectra at room temperature was found to have identical shape for both 266 and 248 nm excitation [54]. However, the redshift is more pronounced for 248 nm excitation.

Figure 4 also shows the normalised fluorescence spectrum dependence on oxygen partial pressure at room temperature, 1 bar total pressure using nitrogen/oxygen bath gas and 248 nm excitation. It is observed that at 248 nm excitation, the spectrum undergoes a redshift with increasing oxygen partial pressure showing that some of the longer wavelength transitions experience lower relative quenching signifying lower Stern–Volmer coefficients. However, the redshift saturates at high enough oxygen partial pressure beyond which no apparent redshift is observed. For room temperature, the saturation oxygen partial pressure was found to be 200 mbar. Similar behaviour was observed at higher temperatures with the maximum red-shift occurring at room temperature. At varying temperatures and oxygen partial pressures, the redshift from individual effects overlap. In nitrogen bath gas, both 248 and 266 nm have same spectral shapes. However, with increasing oxygen partial pressure, the spectrum remains unchanged for 266 nm excitation within the investigated range of conditions. According to Rebeaux et al. [16], if quenching rate constant far exceeds the non-radiative rate constant, then the fluorescence signals will be independent of pressure beyond a threshold value and the signal strength will be directly proportional to equivalence ratio (the underlying assumption behind FARLIF). They showed that this was the case for 248 nm excitation at room temperature beyond a pressure of 3 bar. However, the Stern–Volmer coefficients at different wavelengths vary and also reduce with increasing temperatures and such an assumption may not hold true at higher temperatures especially in the compression stroke of an IC engine where simultaneous high pressures and temperatures are produced.

Figure 5 shows the Stern–Volmer plots for toluene in the presence of nitrogen/oxygen bath gas at a total pressure of 1 bar and varying oxygen partial pressures from the work of Koban et al. [59]. The excitation laser used was 266 nm and the temperature was also varied to study the effects. The Stern–Volmer plots are inverse signal ratio plots which are used to show the quenching effect of a collider species. The slopes of the plots is the Stern–Volmer factor which itself is a ratio of the quenching rate and non-radiative rate. Therefore, the relative importance of quenching and non-radiative rates can be compared from Stern–Volmer plots. Each curve in Fig. 5 is an isotherm. It can be seen that with increasing temperature, the slope reduces signifying a reduction in the Stern–Volmer coefficient. At higher oxygen partial pressures at higher temperatures like 625 K in Fig. 5, the curve also deviates from linearity. The non-linearity signifies a change in Stern–Volmer coefficient at the same temperature. Similar studies were also conducted for 248 nm excitation by [59] in the same environment as that for 266 nm excitation. It was found that Stern–Volmer coefficient decrease with increasing temperatures. Unlike 266 nm, where deviation from linearity is observed only at 625 K, for 248 nm, the deviation

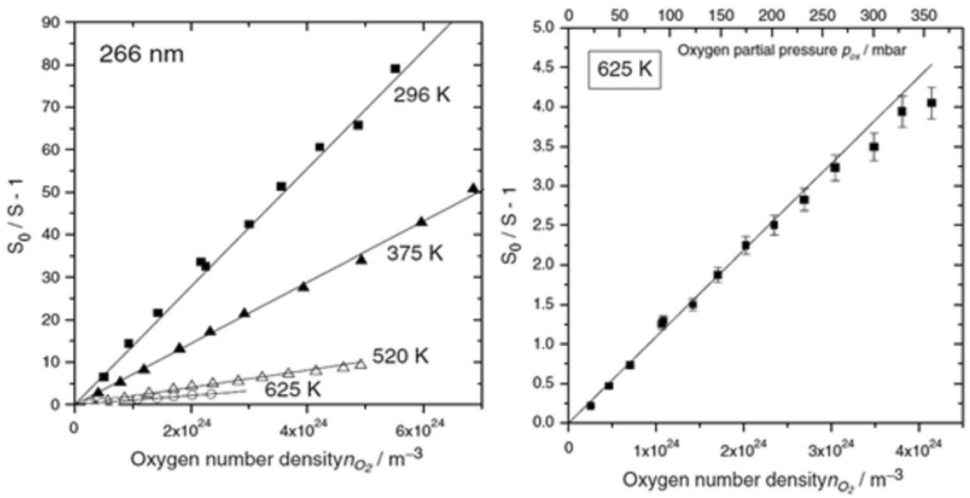

Fig. 5 (from ref [59]) Left image shows the temperature dependence of Stern–Volmer curves whereas the right image shows the magnified curve for 625 K. The total pressure was always maintained at 1 bar using a nitrogen and oxygen mixture

is observed at all temperatures. The plots for 248 nm are not shown for conciseness.

Figure 6 shows the dependence of FQY on temperature in the range from 300 to 950 K normalised at room temperature from the works of Koban et al. [54]. The measurements were carried out in a flow cell with nitrogen bath gas at 1 bar total pressure for 2 different excitation wavelengths of 248 and 266 nm. Toluene was maintained at 5 mbar pressure. It was found that the FQY reduces with increasing temperature for both the wavelengths. The decrease for 266 nm was found to be exponential up to 3 orders of magnitude within 600 K whereas for 248 nm, the decrease was found to be steeper than 266 nm within 600 K and the decrease was slower at higher temperature. Burton and Noyes [56] found that the absolute FQY for toluene at 266.8 nm is 0.3 and 0.09 for 248 nm at room temperature and a total low pressure of toluene at 23 mbar. FQY at 266 nm was given by a single exponential best fit relation valid in the temperature range of 300–950 K at 1 bar total pressure whereas for 248 nm, a biexponential curve fit was developed. Though the decrease in FQY with temperature was expected as the molecule occupies higher vibrational levels with increasing temperature, this was not sufficient to explain the rapid decrease in FQY with temperature.

Cheung in his PhD thesis [60] studied the pressure dependence of toluene FQY at 248 and 266 nm excitation. In this study, in a flow cell, a mixture of nitrogen and toluene was prepared with a fixed toluene partial pressure and varying nitrogen pressure, to vary the total pressure. Two different partial pressures of toluene (11 and 22 mbar) were used. A total pressure of up to 5 bar was achieved. It was found that at 248 nm, the FQY increased with total pressure

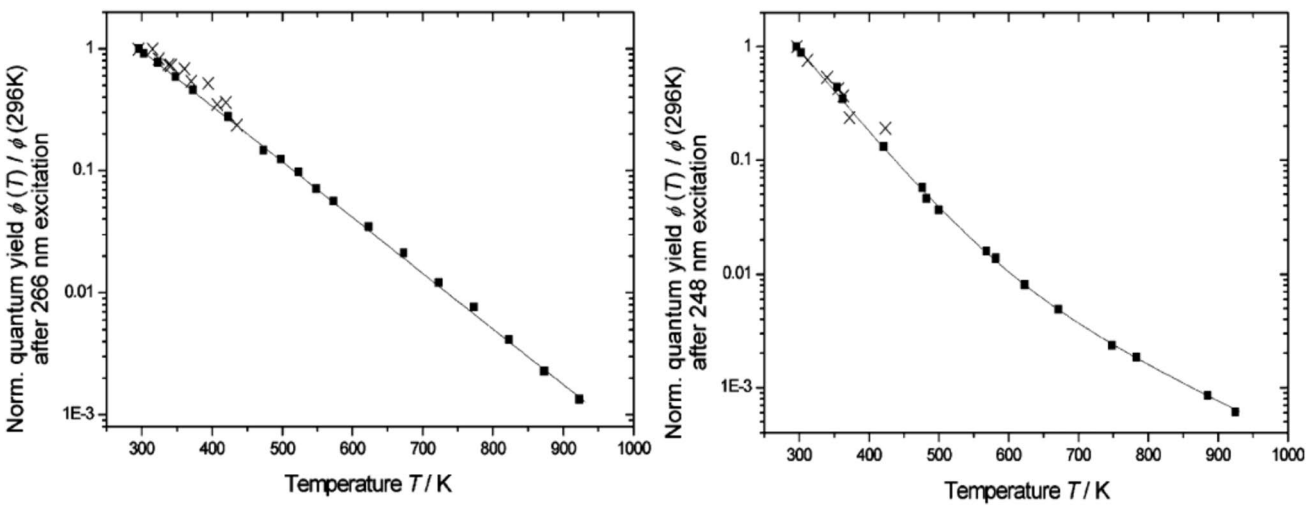

Fig. 6 (from ref [54]): plots depicting the normalised FQY dependence with temperature. Left image shows for 266 nm excitation and the right image shows for 248 nm excitation. Reprinted from [54] with permission from the Royal Society of Chemistry

like their ketonic counterparts. Similar increment in relative FQY for toluene with increasing pressures at 248 nm in a nitrogen environment at 296 K was reported by Yoo et al. [61]. On the contrary, at 266 nm, the FQY decreased with increasing pressure [60]. Normalised fluorescence quantum yield is plotted for 248 nm and 266 nm (Fig. 7) from the works of Koban et al. [59] with varying amounts of oxygen partial pressures along with nitrogen such that the total pressure sums up to 1 bar. Each curve is an isotherm. The FQY values are normalised at a 296 K for pure nitrogen bath gas. Thus, these curves can depict the nature of absolute FQY curves. It is observed that 248 nm results in a lesser FQY than 266 nm. With increasing temperature at a particular oxygen partial pressure, the FQY values are found to decrease. With increasing oxygen content, the effect of quenching can be clearly discerned as the FQY values monotonically decrease. Finally, at very high oxygen partial pressures, the quenching effect was found to get saturated.

Devillers et al. [62] measured the redshift of fluorescence spectra in terms of shift in the centre of gravity of fluorescence spectrum while operation in an optical IC engine at 248 nm laser excitation. They observed that the shift in centre of gravity wavelength towards longer wavelength was more for bath gases containing oxygen. The shift in centre of gravity wavelength increased linearly for increasing pressure and temperature in the optical engine. After 400 °C and 15 bar, a large shift in wavelength was observed corresponding to a significant deviation form the linear behaviour. In terms of fluorescence signal intensity, the authors concluded that toluene fluorescence in nitrogen is 25 times stronger than air at room temperature but the fluorescence signal is only three times stronger than nitrogen at a combined high temperature and pressure region around 350 °C. This suggests the importance of high pressure and high temperature fluorescence behaviour of toluene.

Till now, toluene fluorescence studies were discussed pertaining to either high temperature atmospheric pressure or ambient temperature high pressures. Faust et al. [63] performed fluorescence studies in the combined high temperature high pressure regime at 266 nm laser excitation. The authors covered a pressure range of 1 to 10 bar and a temperature range of 296–700 K for nitrogen bath gas and from 296 to 900 K for air bath gas. The results they obtained are plotted in Fig. 8 where variation in effective lifetime of fluorescence emission is shown. For nitrogen bath gas, they observed that the lifetimes decrease with increasing temperature and the decrease is found to be stronger at higher pressures. At 296 K, the effective lifetime curve is found to be more or less pressure insensitive. However, at elevated temperatures, the lifetimes are found to decrease with increasing pressure. Data from Rossow [64] is also shown for comparison. When the bath gas was replaced by carbon-dioxide, the quenching effect was found to be enhanced by about 5% as compared to nitrogen bath gas. For air bath gas, it was found that due to high oxygen partial pressures, the lifetime values were shorter than nitrogen bath gas. At a constant temperature, the lifetime values were found to reduce with increasing pressure, with the effect becoming more visible at lower temperature. The effect of quenching due to oxygen was found to saturate around 10 bar total pressure or an oxygen partial pressure of 2 bar. With increasing temperature, the lifetime values remain relatively insensitive at lower temperature but then start decreasing after a certain threshold temperature. At higher pressures, this threshold temperature value also was found to increase. For comparison purposed, the model proposed by Koban et al. [59] was plotted. Agreement was better at low pressure of 1 bar. At higher pressures, large deviations were observed since the model was developed for pressures above 1 bar.

Discussion

In order to understand the fluorescence characteristics of aromatic compounds and to use the fluorescence data in PLIF experiments, it was necessary to develop models for predicting the fluorescence signals. For this purpose, the non-radiative and radiative rate's dependence on vibrational energy level of the excited singlet manifold needs to be understood. Apart from these, the aromatic compounds are also more sensitive to oxygen quenching unlike their ketonic

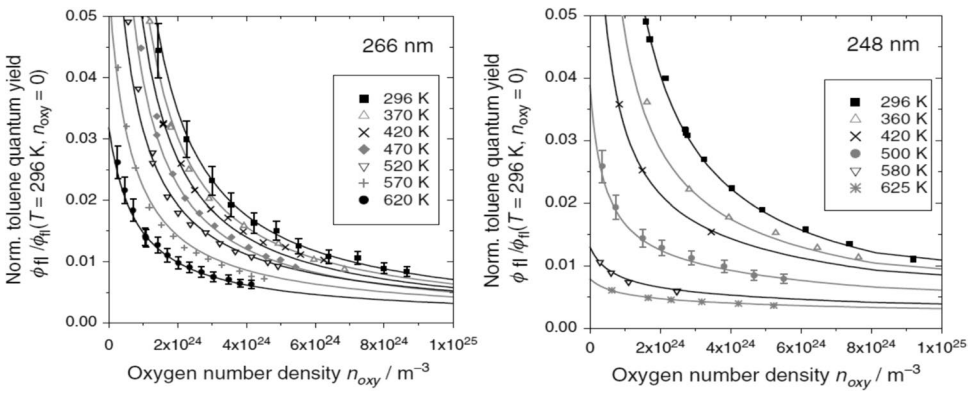

Fig. 7 (from ref [59]) Plots showing the dependence of fluorescence signal intensity with increasing oxygen partial pressures. The left image is for 266 nm and the right image is for 248 nm. Each isotherm is normalised to the intensity value at 296 K in a pure nitrogen bath gas

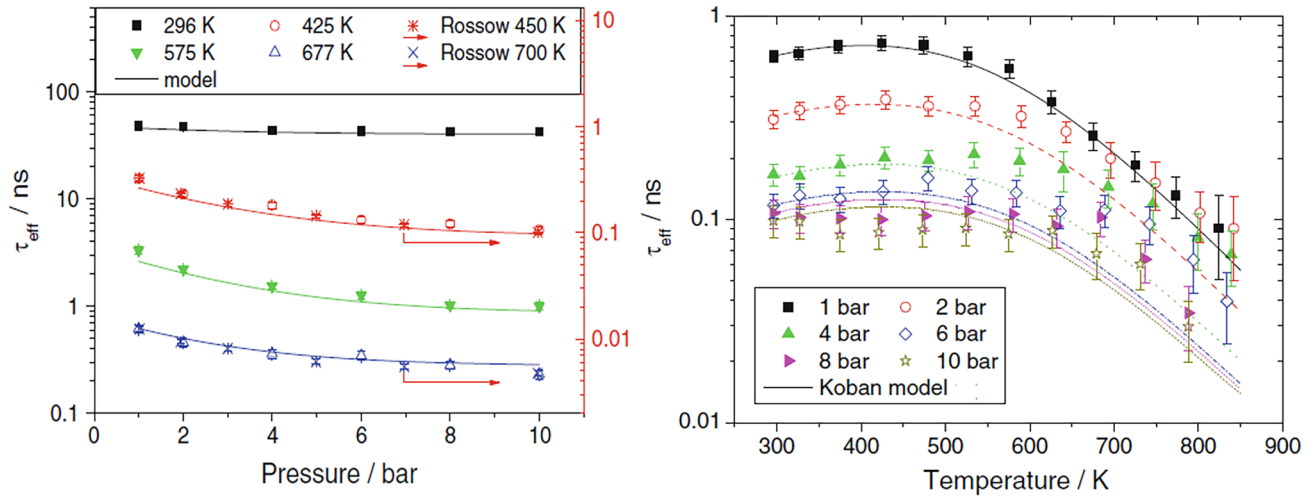

Fig. 8 (from ref [63]) Plots showing the dependence of effective fluorescence lifetime values with varying temperature and pressure. Left image shows the variation in a nitrogen bath gas whereas the right image shows variation in air bath gas. Solid lines in nitrogen plot shows data predicted by Faust model [63] and lines in air bath gas shows data predicted by Koban model [59]. Data from Rossow [64] is also plotted

counterparts. This is due to the larger energy gap between the excited singlet and triplet states of the molecule which upon collision with a ground triplet state oxygen molecule makes a larger amount of energy available for exciting the oxygen molecule into an excited singlet from the ground triplet state [1]. Upon excitation of a toluene molecule due to laser absorption, there is a competition between several intra and intermolecular radiative and non-radiative processes. The Stern–Volmer (SV) factor (k_{SV}) and FQY are very useful to compare the relative strength of different processes. k_{SV} is the slope of the Stern–Volmer plots which for oxygen collider were presented in Fig. 5. It compares the oxygen quenching and total non-radiative decay rates. The quenching rate is proportional to the collision frequency which itself has a weak temperature dependence [59].

Any bimolecular collision dependent quenching can be represented by a Stern–Volmer plot that is typically linear in nature if the fluorescence takes place from a single vibrational level. With increasing temperature, the ground state distribution is modified as a larger fraction of molecules occupy the higher vibrational levels of the ground electronic state. For a constant excitation wavelength, a fixed amount of energy is added to such molecules resulting them in ending up into still higher vibrational levels of the excited singlet after laser absorption. Thus, decreasing excitation wavelength or increasing temperature results into the ground state molecules being excited into higher vibronic levels. Depending on the spacing of the electronic levels, for certain aromatic molecules, sufficiently lower wavelengths can result in the excitation to the second excited electronic level. Thus, apart from the quenching rate, the temperature and wavelength dependency of SV factors will be decided by the dependency of non-radiative decay rates on excess vibrational energy in the excited singlet state. Frerichs et al. [65] studied the dependency of non-radiative rates and fluorescence rate on excitation energy. They found that the total non-radiative rate increases with excitation energy. Furthermore, the fluorescence rate was observed to increase slightly and then become constant with excitation energy. Farmanara et al. [66] determined the rate of internal conversion from second excited singlet state to the ground singlet state. 70% of such excited toluene molecules were found to undergo this transition and 30% of the remaining molecules underwent internal conversion to the first excited singlet and then transitioned to the ground singlet.

Figure 9 shows the Jablonski's diagram for absorption after 248 and 266 nm excitation. The ground state singlet and excited state singlet are represented as S_0 and S_1 respectively. The excited triplet state T_1 is also shown. Upon excitation with 266 nm, the excitation is very close to the zero vibrational level of the excited singlet since the 266.8 nm excitation value corresponds to the 0–0 transition [56]. The 248 nm wavelength results in excitation to higher vibrational levels of S_1. Burton and Noyes [56] concluded that when the excitation is to a lower vibrational energy very close to the zero level of excited singlet state, inter-system crossing and fluorescence are the dominant photophysical processes with their respective yields adding up to unity. Inter-system crossing is shown at lower levels in Fig. 9. Furthermore, with the increase of vibrational levels with decreasing excitation wavelengths, another process begins to dominate which is so fast that it even overshadows the effects of vibrational relaxation. The distinctive features of Stern–Volmer plots can be explained now.

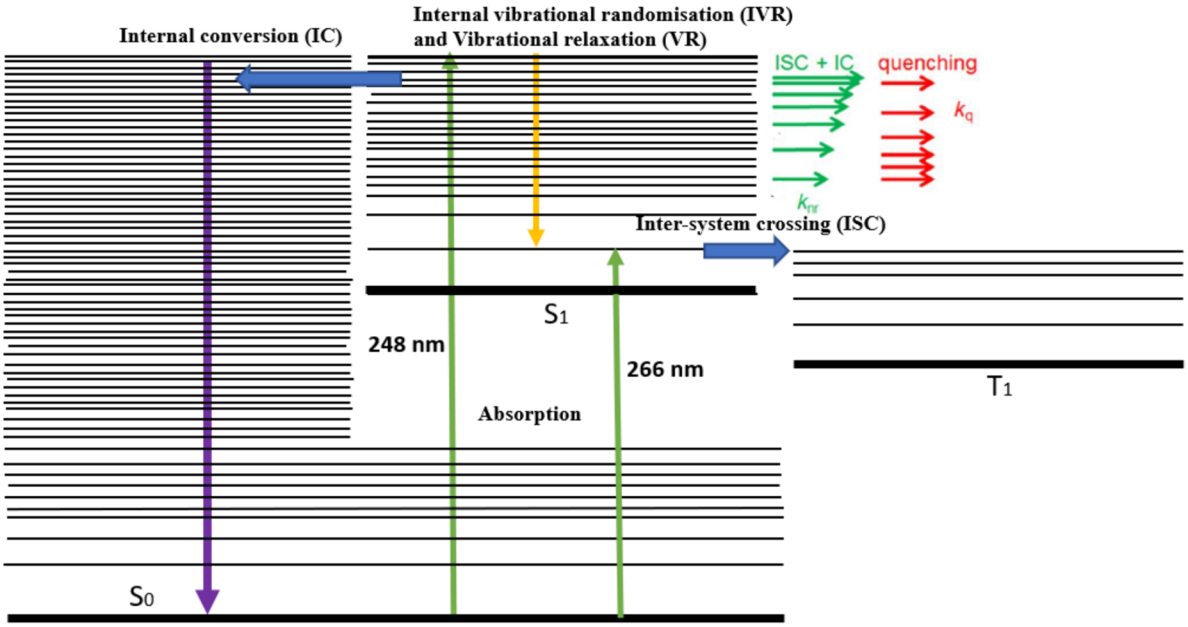

Fig. 9 Jablonski's diagram showing the above discussed photophysics relevant for toluene molecule

The slope of the SV plots referred to as the Stern–Volmer factor is found to reduce with increasing temperatures. At higher temperatures, the molecule gets excited to a higher vibrational level of S_1 state. Since the quenching is weakly dependent on temperature [59] and the non-radiative rate increases with vibrational energy level (relative strengths shown by the arrow sizes in green and red), the SV factor which is basically a ratio of these two rates essentially shows a decline for 266 nm excitation. For 248 nm excitation, similar trends are observed. The rapid decrease of FQY in Fig. 6 in nitrogen bath gas could not be explained by an increasingly efficient inter-system crossing rate with vibrational energy levels. In the literature, a third decay mode or channel was used to explain this observation. Jacon et al. [67] found bi-exponential decay rate of fluorescence for wavelengths shorter than 250 nm. The shorter time scale was due to a fast third decay channel and the longer-lived component was similar to those measured by Koban et al. [59] and was attributed to be dominated by inter-system crossing. The third decay channel appears beyond a certain threshold of energy which is specific to a particular molecule [67]. Koban et al. [59] tried to explain the non-linearity in SV plots above 300 K at 248 nm and above 500 K for 266 nm by hypothesizing that the fluorescence decay was occurring from two different levels- one dominated by relatively slower ISC resulting in long lived components and the other dominated by the very fast third decay channel resulting in short lived components. The authors suggested that the third decay channel can be internal conversion from S_1 to S_0 state since it was observed at high excitation energies for other aromatic compounds like naphthalene [68] and benzene [69]. Faranmara et al. [66] noted that at 202 nm there is significant IC and the effective lifetime was around 4 picoseconds. For ISC dominated states the effective lifetime is of the order of nanoseconds.

Even after selective excitation, more than one vibrational energy level can be populated. Jacon et al. [67] and Koban et al. (2005) [59] suggested that even for monochromatic excitation, both optically active and inactive vibrational modes might get populated due to anharmonic coupling. Furthermore, more than one states can also be populated by laser excitation which is never strictly monochromatic. There can also be intramolecular vibrational randomization (IVR) which can result in many optically dark vibrational levels being populated by energy redistribution from an optically active level as it is shown in Fig. 9, keeping the total molecular energy to be constant. IVR occurs rapidly if the density of states is high and there is a high degree of energy localisation. IC becomes dominant at higher energy levels and Smalley (1983) [70] indicated that the onset of IC coincide with onset of IVR. Thus, excitation with shorter wavelengths, or at higher temperatures, result in the redistribution of energy among levels part of which are dominated by IC and the other dominated by ISC. States dominated by IC has shorter fluorescence lifetime making those levels less sensitive to oxygen quenching and the resulting decrease in slope of the SV plots. It is important to emphasize the difference between IVR and VR. Loss of excess vibrational energy from the excited molecule can take place through a unimolecular fast process ($10^{11} \sim 10^{13}\ s^{-1}$) known as IVR and through a slower

process ($10^9 \sim 10^{11}$ s^{-1}) based on energy transfer to bath gas molecules due to collisions known as vibrational energy transfer (VET) [64]. Strictly speaking both VET and IVR contribute to vibrational relaxation where the molecule loses excess vibrational energy until it reaches the thermalised level. However, in literature the term VR is used to address only intermolecular collision process (or VET) and therefore, for consistency in this text the term VR will be used to represent only the intermolecular collision and the term IVR will be used to address only the intramolecular process similar to the work of Rossow [64]. Both IVR and VR are shown combined in Fig. 9.

Based on this Koban et al. (2005) [59] proposed a model where they predicted FQY values by estimating the fraction of molecules in vibrational levels dominated by IC and ISC. They then summed up the individual fluorescence yields of both the energy levels to determine the total fluorescence yield. However, since oxygen quenching is dominant, they assumed that the other major gas has a negligible effect. From Figs. 4 and 7, it is seen that oxygen effect saturates at higher oxygen partial pressures. Thus, the model was restricted to bath gas pressures of 1 bar with varying oxygen content until saturation of oxygen quenching is observed. Since this model was restricted to 1 bar total pressure, it is insufficient to explain the pressure effects of the bath gases on toluene fluorescence as observed by [60] and in Fig. 8. Faust et al. (2013) [63] tried to modify the Koban model by introducing a pressure correction term in absence of oxygen to predict FQY at pressures greater than 1 bar. However, even this modification was found to be insufficient since it could not give proper results for air bath gas at simultaneously elevated temperature and pressure regimes. The authors suggested that phenomenological model as prepared by Thurber [71] and Koch [72] for ketonic compounds could be used to better predict the FQY of toluene. Rossow (2011) [64] tried to modify the step-ladder model for acetone and 3-pentanone (refer part A) to explain the pressure effects observed for toluene. According to the model, FQY (ϕ) for toluene is evaluated by Eq. (7) which calculates the sum over all N vibrational levels in the excited singlet state occupied by an average molecule as it decays. The decay of the molecules from higher vibrational levels is considered to be a multi-step process. Level 1 represents the highest vibrational level in the excited state manifold, level N is a vibrational level that is very close to the thermalised level at which the summation is stopped, and vibrational energy levels intermediate between level N and level 1 are referred to as *ith* energy level. For a certain vibrational level E, contribution to the total FQY is calculated by the effective FQY from that level, which shows the probability of fluorescence in contrast to other decay pathways, multiplied by the likelihood of the molecule decaying to level E before fluorescing or undergoing intersystem crossing.

$$\Phi = \frac{k_{\mathrm{fl}}}{k_{\mathrm{fl}}+k_{\mathrm{vib}}+k_{0_2}+k_{nr,1}} + \sum_{i=2}^{N-1}\left[\frac{k_{\mathrm{fl}}}{k_{\mathrm{fl}}+k_{\mathrm{vib}}+k_{0_2}+k_{\mathrm{nr},i}}\prod_{j=1}^{i-1}\left(\frac{k_{\mathrm{vib}}}{k_{\mathrm{fl}}+k_{\mathrm{vib}}+k_{0_2}+k_{\mathrm{nr},j}}\right)\right] + \frac{k_{\mathrm{fl}}}{k_{\mathrm{fl}}+k_{0_2}+k_{\mathrm{nr},N}}\prod_{j=1}^{N-1}\left(\frac{k_{\mathrm{vib}}}{k_{\mathrm{fl}}+k_{\mathrm{vib}}+k_{0_2}+k_{\mathrm{nr},j}}\right) \tag{7}$$

In Eq. (7), the first term represents contribution from the vibrational level N, the last term accounts for the contribution from the thermalized level, and the summation term consists of contribution from the various intermediate levels. From a vibrational energy level, various energy transferring processes are assumed to take place, the rates of which are denoted in the Eq. (7). k_{fl} represents the fluorescence rate constant and is assumed to be constant with vibrational energy level. $k_{\mathrm{nr},i}$ represents the non-radiative decay rate at the *ith* energy level. The non-radiative decay rates can be measured from the experimental effective lifetime data at very low pressures (ex: 10 mbar in carbon-dioxide from [73]) as at such low pressures there will be very less collisions resulting in insignificant vibrational relaxations. Thus, assuming a constant fluorescence rate constant in a non-quenching environment, the non-radiative rate constants were estimated as a function of vibrational energy. k_{0_2} represents the quenching rate constant due to oxygen and is proportional to the oxygen number density and the probability of quenching also increases with increasing vibrational energy level. k_{vib} represents the rate constant for vibrational relaxation. It is to be noted that the model does not include IVR and only accounts for VR. As will be seen, newer step-ladder models (like the one proposed for anisole by Wang et al. [74]) contains separate terms for VR and IVR.

Rossow relaxed the assumption of unidirectional energy transfer from the excited molecule to the bath gas molecule and adopted a bi-directional energy transfer. At a particular temperature, an average thermalized energy level was then associated with a molecule. The difference in the thermal energy levels in both the singlet states was calculated for different temperatures. If the energy corresponding to the laser excitation is smaller than this above-mentioned value then the molecule will end up in a state that is lower than the thermalised level. This is called photo-induced cooling. Under such circumstances, the molecule gets heated up from collisions with the surrounding bath gas. This causes the molecule to climb higher up in the electronic manifold. As higher vibronic levels have a lower FQY value, this will lead to a decrease in FQY with increasing pressure. This pressure related reduction in FQY occurs for wavelengths equal to the 0–0 transition or longer. If the laser excitation is sufficiently large, then the molecule ends up in a vibrational energy level higher than the thermalised level. This will result in the loss of vibrational energy of the toluene molecules upon collisions with bath gas molecules. This type of collisions that

increase FQY values was reported by Hippler et al. [75]. The molecule will drop down inside the electronic manifold to lower vibrational levels leading to a progressive increase of FQY. This sort of pressure related stabilisation was seen in the ketonic compounds as well [76–78]. This explains the decrease of FQY for toluene for 266 nm excitation with increasing nitrogen bath gas pressure whereas for 248 nm, an increase is observed. The difference in the thermalised energy for both the singlet states increases with temperature. Such calculations were performed for naphthalene by Rossow. It is expected that a similar phenomenon holds for toluene as well. With increasing energy gap, the laser excitation wavelength required reduces for excitation to the thermalised level. Therefore, with a constant laser excitation, the photo-induced cooling effect should be increasing with increasing temperature. Therefore, at higher temperatures, the pressure induced destabilisation or decrease of FQY values (also fluorescence lifetime) should show an increase. This behaviour is observed for toluene at 266 nm in Fig. 8 in a nitrogen bath gas. In the figure, the fluorescence lifetime value was found to be insensitive to pressure increment at lower temperature but showed large drop at higher temperatures.

3 Anisole

The second mono-aromatic compound we will be discussing in this section is anisole (or methoxybenzene). Anisole molecule consists of a methoxy group that is substituted on a benzene ring (molecular structure is shown in Fig. 10). One of the earliest studies of anisole fluorescence signals for diagnostics purposes was performed by Hirasawa et al. [79]. The authors had compared various tracer molecules including anisole in nitrogen bath gas at 290 K and atmospheric pressure and found that the fluorescence intensity of aromatic molecules was about two orders of magnitude higher than the ketonic counterparts. Anisole exhibited the highest amount of fluorescence signal intensity. Furthermore, Faust et al. [80] observed that in comparison to toluene, anisole has a stronger Stokes shift than toluene (10–15 nm more redshift of the fluorescence spectrum peak in comparison to toluene). Along with this, a 63% larger FQY and 50 times stronger absorption cross-section than toluene, a large improvement in signal to noise ratio can be expected for anisole under identical imaging conditions [80]. A stronger absorption cross-section will also enable a lower doping vol% which will further restrict the influence of tracer addition on measured engine performance. Along with the mentioned advantages, the cheap, non-toxic and non-carcinogenic nature of anisole, it becomes quite attractive as a tracer for LIF imaging.

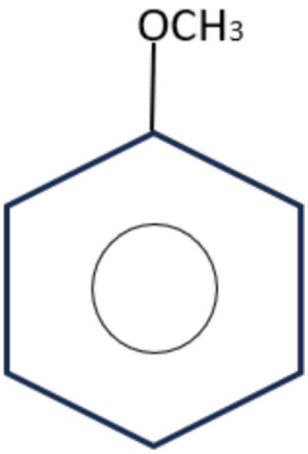

Fig. 10 Schematic diagram of anisole (methoxybenzene) molecule

Based on this, anisole was used in PLIF studies to measure fuel–air distribution in the works of Laichter and Kaiser [81] and Kranz et al. [82]. Kranz et al. [82] performed PLIF imaging in a PFI engine for IVC (Intake valve closed) injection where initially a rich fuel mixture enters the cylinder in the early intake stroke followed by a very lean charge [83]. Turbulent structures were observed in the initial mixing phase of the rich charge with the in-cylinder residual gases. Later on, the rich mixture cloud was found to convect with the existing strong clockwise tumble vortex. Laichter and Kaiser [81] performed both PIV and PLIF to study the causes of CCV of flame propagation. They found that in PFI mode, the flow field near the spark plug had a strong impact on subsequent combustion speed, whereas for GDI mode, the flow field and flame propagation were found to be uncorrelated and the equivalence ratio distribution became more important. A similar strong dependency of combustion variability on CCV of flow fields in PFI engines was also observed in the works of Hokimoto et al. [84]. Anisole as a tracer for PLIF studies has received attention quite lately and therefore there are very limited number of works involving it for measuring fuel distribution. It is however expected that its use will grow owing to its promising characteristics.

Nonetheless, it has also found usage in temperature measurement owing to its strong fluorescence signal intensity. One of the earliest temperature distribution studies using anisole PLIF was performed by Tran et al. [85] in a rapid compression machine (RCM) where the measurement was able to characterise the non-homogeneous temperature distribution. Kranz et al. [82] performed two colour thermometry using anisole as a fluorescence tracer in a PFI engine operated with methane. The authors found that as the injection timing was during closed valve, initially, the incoming charge was found to be quite rich with a low temperature as compared to the in-cylinder gases at 60 CAD ATDC of intake stroke. The high temperature region was therefore located near the piston due to a displacement of the hot gases from the cylinder head

region by incoming charge. Later on, at 220 CAD, unexpectedly, the rich mixture region showed high temperature. This was because in IVC injection for PFI engines, entry of a rich mixture happens in the early intake stroke followed by nearly pure air. The initial rich mixture mixes well with the surrounding hot gases and gets heated while the following fresh charge is mostly cold at a lower temperature. Towards the end of compression stroke, mostly a homogeneous mixture was observed. Recently, Shahbaz et al. [86] performed two-colour thermometry in a metal engine with endoscope access using anisole. They studied temperature distribution starting from the compression stroke to the gas exchange process. The authors observed that during compression stroke, the temperature distribution is mostly uniform other than a localised high temperature region around the hot spark plug. In the gas exchange process, at − 20 CAD ATDC of intake, residual gases at 450 K were located near the intake valve. The residuals were found to be displaced at intake TDC by an incoming cooler fresh charge. Interestingly at 20 CAD, the residuals show a higher temperature than that at intake TDC due to their mixing with hot exhaust gases that have re-entered into the cylinder from exhaust manifold due to backflow. At 40 CAD, an overall cooling of both the fresh charge and residuals was observed due to mixing with new cooler fresh charge and gas expansion due to piston downward motion.

3.1 Absorption cross-section

Anisole has a large absorption cross-section of 3.35×10^{-18} cm^2 at 296 K for 266 nm laser excitation [87] owing to the strong $\pi \rightarrow \pi^*$ transition. The 0–0 energy gap for anisole for S_0 to S_1 transition is about 36,394 cm^{-1} [88]. Anisole has an absorption spectrum ranging from 240–310 nm centred at around 270 nm [87]. Figure 11 shows the absorption spectrum of anisole at various increasing temperature. The plot to the left in Fig. 11 was obtained by Zabeti et al. [87] and shows two distinct measurements of absorption spectrum: one in a shock tube with 7 nm spectral resolution (solid lines) and another in a flow cell with a high spectral resolution of 0.2 nm (dotted lines). At low temperatures, the spectrum of anisole shows some features at low resolution which can in turn be seen as having several sharp peaks at high resolution. Tran et al. [18] also observed such features in anisole absorption spectrum and reported three different peaks at 266, 272 and 278 nm. There are a few temperature impacts that can be directly discerned from the plot. With an increase in temperature, the fine structures are lost gradually as can be seen in the high resolution 573 K that matches closely with the low-resolution curve at 565 K. Tran et al. [18] found that from 773 K onwards, the absorption spectrum loses its structure and becomes a continuous broadband spectrum. This type of loss in structure of absorption spectrum was also observed for toluene from 600 K [54]. Interestingly, there is also redshift and broadening as was observed in toluene and other ketonic compounds (refer part A of this work). At increased temperature, more molecules occupy the thermally excited higher vibrational levels in the ground state that makes absorption possible at larger wavelengths resulting in the broadening of the spectrum towards the red side of 0–0 transition. The resulting broadening then results in the loss of structure.

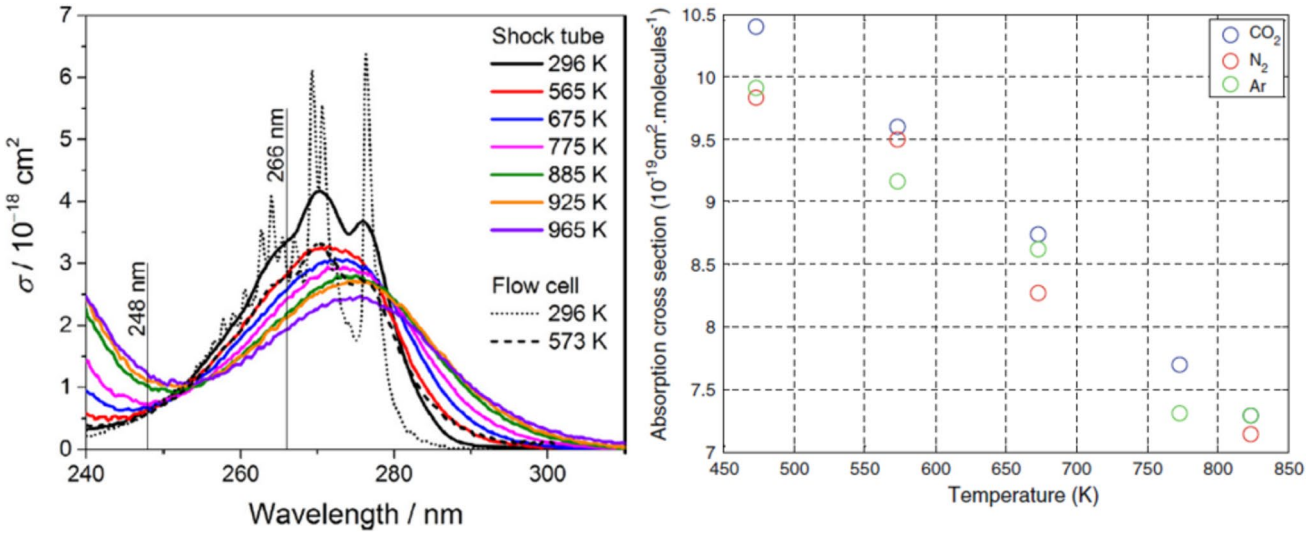

Fig. 11 Left image (from ref [87]) shows the plots of absorption spectrum at various temperatures for anisole. Adapted from [87] with permission from Elsevier. Right image (from ref [18]) shows the variation of absorption cross-section at 266 nm with increasing temperature in nitrogen, air and carbon-dioxide bath gases

A peculiar temperature effect that is contrary to other commonly used tracer molecules is the reduction in the value of absorption cross-section for anisole at 266 nm with an increase in temperature. This can clearly be seen from the spectrum plots in Fig. 11. Tran et al. [18] also studied the temperature effect and found a similar reduction in cross-section values at different bath gases for 10 bar pressure which are shown in the right side plot of Fig. 11. The reason for this behaviour is not clear as of now. At very low wavelengths (smaller than 248 nm) one can observe from absorption spectrum plots in the left image of Fig. 11, an increase in the absorption cross-section just as in the case of toluene. This might be due to the gradual broadening of S_0 to S_2 spectrum that eventually merges with the S_0 to S_1 spectrum. From the spectrum, it is clear that at 248 nm, the absorption cross-section values should increase with temperature. However, unlike 266 nm, dedicated cross-section plots as a function of temperature is not available for 248 nm.

3.2 Fluorescence signal variation

Faust et al. [80] obtained the fluorescence spectrum of anisole at varying temperatures ranging from 296 to 977 K at 1 bar pressure with nitrogen as the bath gas and their results are shown in the left image of Fig. 12. Their experiments were performed at 266 nm laser excitation. Anisole has a fluorescence spectrum ranging from 270 to 360 nm with a peak at around 290 nm at 296 K. As previously mentioned, anisole has got a larger Stokes shift than toluene. This can be observed from the fluorescence spectrum plots in Fig. 12 where the room temperature fluorescence spectra are provided for both toluene and anisole. The spectrum at room temperature lacks structure and has a general broadband shape. The FWHM is measured to be 32 nm at 296 K close to the value of 30 nm as measured by Hirasawa et al. [79]. The fluorescence intensity is also found to reduce with increasing temperature. Zabeti et al. [87] found a reduction in the fluorescence intensity by about three orders of magnitude in a temperature range of 296–980 K. At 12 bar pressure in a carbon-dioxide bath gas, Tran et al. [18] found that the signal reduces by a factor of fifty in the temperature range of 473–823 K. The reduction in fluorescence intensity with temperature is a common phenomenon among the tracer molecules and is mainly due to the increase in non-radiative de-excitation processes at elevated temperatures. Such a reduction in signal intensity is not apparent from the fluorescence spectra shown in Fig. 12 as the spectra are normalised to their respective maximum intensity at a given temperature. This is done in a way to better depict the red-shift that is occurring with increasing temperature. However, the fluorescence spectra provided in the works of Tran [18] and Zabeti [87] are normalised to a fixed reference value (the maximum value of the fluorescence intensity recorded at the lowest temperature of their respective works), a reduction in the fluorescence signal intensity can be clearly seen in the relevant plots in those works. In Fig. 12, at higher temperatures of 875 and 977 K, the fluorescence spectra plots are found to show a different shape along with some fine structures in contrast to the broadband shape at lower temperature curves. Faust et al. explained that at high temperature, the fine structures are due to noise that now become more obvious at the reduced fluorescence intensity. Furthermore, the change in spectra shape at 875 and 977 K was due to pyrolysis of anisole molecule. The pyrolysis products also fluoresce because of which the respective spectra overlap giving a different overall shape to the fluorescence spectra.

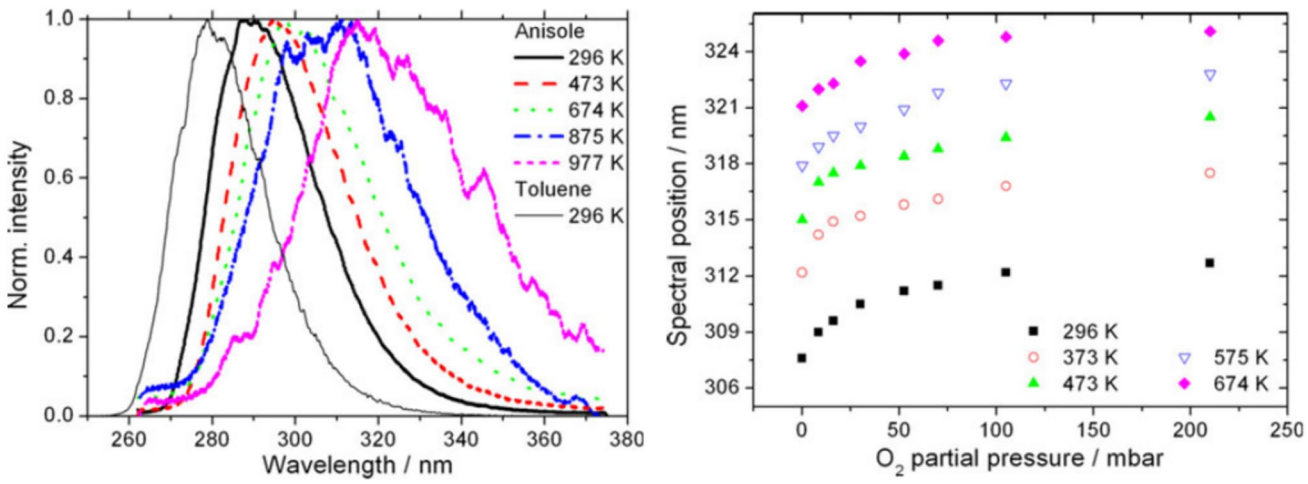

Fig. 12 (from ref [80]) Left image shows the plots of fluorescence spectra at various temperatures for anisole. Right image shows the redshift of fluorescence spectra at 266 nm with increasing temperature and oxygen partial pressures. The fluorescence signals are collected at a constant anisole number density of 5×10^{22} m^{-3} in the measurement volume

The pyrolysis effect of anisole is further corroborated from the fluorescence spectra provided by Zabeti et al. [87] where such change in fluorescence spectra shapes is not observed even at 980 K by preventing pyrolysis of anisole with shorter residence times in a shock tube.

With an increase in temperature, the fluorescence spectra are found to broaden and exhibit redshift. This is clear from the fluorescence spectra curves in Fig. 12. The redshift is due to the excitation of additional vibrational levels from higher available energy at larger temperatures [18]. The redshift was found to be about 3 nm [80], 2.5 nm [18], 2.8 nm [87] per 100 K. Additionally, a redshift in the fluorescence spectra is also witnessed by Faust et al. [80]. They determined the fluorescence spectra at various oxygen partial pressures (till 210 mbar) along with nitrogen keeping the total bath gas pressure constant at 1 bar. The measured redshifts are plotted in the right image of Fig. 12. The plots show the redshifts both due to increasing temperature and oxygen partial pressures in bath gas. The oxygen partial pressure is increased in steps such that the bath gas changes from pure nitrogen to air. A redshift of 5 nm was found at 296 K across the range of oxygen partial pressures used. The excitation wavelength used was 266 nm. However, as discussed in the previous section, in contrast to anisole, toluene did not show any oxygen induced redshift at 266 nm rather the redshift was observed at 248 nm. Additionally, Tran et al. [18] also did not observe oxygen induced redshift of fluorescence spectra of anisole. The reason for this apparent inconsistency is not clear at the moment. From Fig. 12, it can be seen that the redshift saturates at about 100 mbar of oxygen and also the amount of redshift due to oxygen addition reduces at elevated temperatures. From, fluorescence spectra obtained at 296 K with 1 bar total pressure in nitrogen bath gas (figure not included here), Faust et al. [80] observed that addition of oxygen does not result in broadening of spectra.

In addition to the redshift, another effect of temperature, observed, was the decrease in fluorescence signal strength for anisole. Since fluorescence signal is dependent on the product of absorption cross-section and FQY, it is important to understand the individual effect of temperature on both the quantities. Absorption cross-section at 266 nm for anisole was found to decrease with increasing temperature as was discussed earlier. Therefore, this definitely has a role to play in the reduction of fluorescence signal. Figure 13a shows the plots of both fluorescence signal and absorption cross-section at 266 nm with temperature. The study was performed by Zabeti et al. [87] in a nitrogen bath gas at 1 bar. From the plots, it is observed that over the temperature range considered, the reduction in fluorescence signal is about three orders of magnitude whereas the absorption cross-section reduces only by a factor of two. Therefore, the strong reduction in fluorescence signal must be due to a strong reduction in FQY. Relative FQY plots are shown

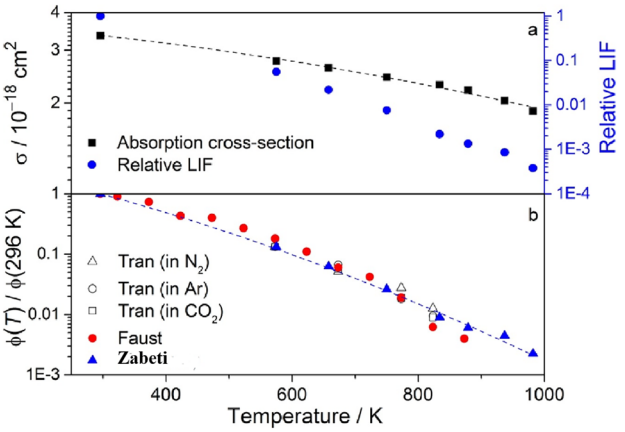

Fig. 13 (from ref [87]) **a** Plots show the absorption cross-section and relative fluorescence signal obtained by normalising the LIF signal with the corresponding value at the lowest temperature in 1 bar nitrogen bath gas for 266 nm excitation. **b** Plots show the relative FQY in nitrogen at 1 bar pressure (Faust et al. [80] and Zabeti et al. [87]), nitrogen in 4 bar pressure (Tran et al. [18]). Adapted from [87] with permission from Elsevier

in Fig. 13b in non-quenching bath gases like in nitrogen at 1 bar pressure [80, 87], nitrogen at 4 bar pressure [18]. It is found that the relative FQY reduces roughly exponentially by a factor of about 450 in a temperature range of 296 to 980 K.

Another way to characterise the fluorescence behaviour is to use effective lifetime values. Since $\phi = \tau_{eff} \times k_{rad}$, and normally k_{rad} doesn't vary much with respect to the vibrational levels, the lifetime values are proportional to absolute FQY values. Therefore, the variation in effective lifetime values should be similar to the variation in absolute FQY values. The absolute FQY value of anisole is 0.36 [89]. This can be observed in Fig. 14 where the lifetime values in ns are plotted as a function of temperature at different pressures in a nitrogen bath gas. The study was performed by Faust et al. [80] and they found that the lifetime values decreased from 13.3 ns at 296 K to about 0.05 ns at 875 K at 1 bar pressure. The slope of reduction was found to be higher at the elevated temperature regime as can be clearly seen from the plot. Furthermore, pressure was found to have a minimal impact at lower temperatures while it increased slightly after 600 K. Overall, the authors concluded that the effect of pressure in nitrogen bath gas is lower than toluene for 266 nm excitation. Further description of impact of pressure on anisole lifetimes will be provided shortly.

The right image in Fig. 14 shows the plots of effective lifetimes with increasing oxygen partial pressure at various temperatures. The total pressure maintained was 1 bar with nitrogen and oxygen mixture. In the x-axis, oxygen partial pressure increases from zero (indicating pure nitrogen) to 210 mbar (indicating air). For zero partial pressure, the

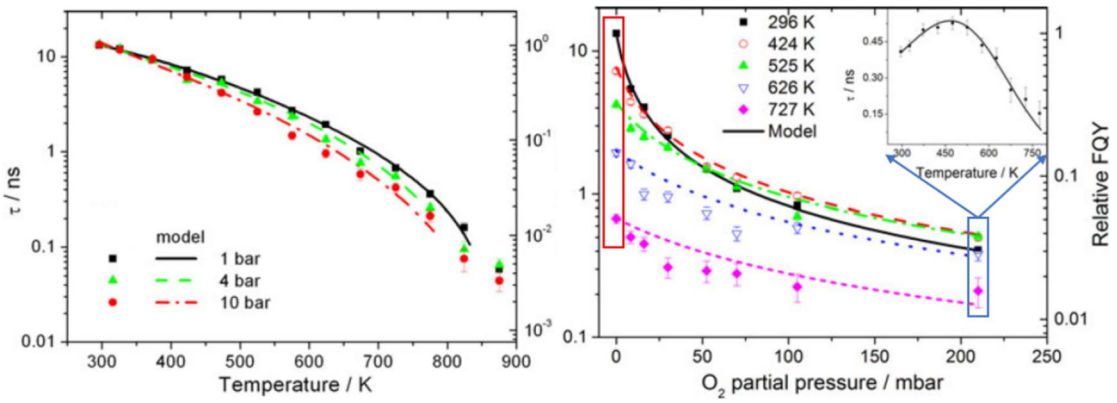

Fig. 14 (from ref [80]) Left image shows the effective anisole lifetime in pure nitrogen bath gas at 1, 4 and 10 bar with increasing temperatures. Right image shows the effective lifetime of anisole in nitrogen and oxygen mixtures with different oxygen partial pressures for increasing temperature. The total pressure is kept constant at 1 bar. FQY results obtained from the model developed by [80] are plotted in the left-hand axis of both the figures

effective lifetime can be seen to show a monotonic decrease with increasing temperature as highlighted by the red box. This is consistent with the monotonic decrease obtained as in the left image of Fig. 14. In general, oxygen containing bath gases introduce quenching effect that reduces lifetime. The effective lifetime of anisole at room temperature reduces from 13.3 ns in nitrogen to 0.4 ns in air. In contrast to pure nitrogen bath gas, in air the fluorescence lifetime values show a different behaviour with increasing temperature. This can be seen for 210 mbar (highlighted by blue box). There is a non-monotonic behaviour in which the lifetimes first increase followed by a decrease with increasing temperature. This can be better seen in the exploded figure in top right corner as demarcated by blue arrows in the figure. The isotherms show a decrease in effective lifetime with increasing oxygen partial pressure suggestive of an enhanced quenching rate with increasing oxygen concentrations. Similar quenching effects were also seen in the study of Tran et al. [18] where they observed a fluorescence signal decrease of 12.5 times from pure nitrogen to nitrogen and oxygen mixture (20% oxygen mole fraction). When oxygen quenching is the dominant de-excitation mechanism, it has the potential to be used in fuel–air mixture distribution imaging using FARLIF technique. The amount of oxygen quenching can be quantified using Stern–Volmer plots as was already shown for toluene. Such plots were obtained by both Faust [80] and Tran [18]. Figure 15 shows the Stern–Volmer plots for anisole as obtained by Faust et al. [80] for a 1 bar total pressure. The plots are observed to be straight lines with no apparent deviation from linearity. The slopes of the plots is the Stern–Volmer factor (k_{SV}) is a ratio of the quenching rate and non-radiative de-excitation rate. The slope is found to reduce with increasing temperatures. At higher temperatures, the molecule gets excited to a higher vibrational level of S_1 state. Since the quenching is weakly dependent on

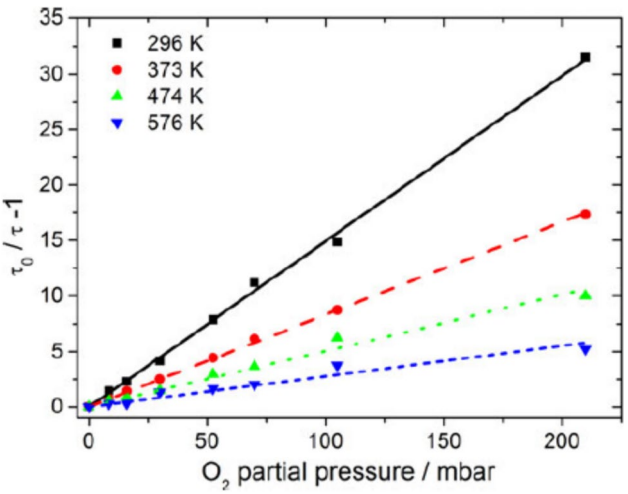

Fig. 15 (from ref [80]) Stern–Volmer plots for anisole at 1 bar total pressure with oxygen as the collider molecule

temperature [59] and the non-radiative rate increases with vibrational energy level, the SV factor which essentially shows a decline for 266 nm excitation.

In addition to temperature and bath gas, pressure also has an influence on the FQY values and thus needs to be studied. Figure 16 shows the variation with respect to pressure changes. The left image of Fig. 16 shows the variation of effective lifetime values as obtained from the study of Benzler et al. (2015) [73] at different temperatures with an increasing pressure till 1 bar in a nitrogen bath gas. The lifetime values show an increase at lower temperatures of 298 and 355 K and a decrease at higher temperatures of 405 and 475 K. The pressure sensitivity shows a decrease from 298 to 355 K and then an increase from 405 to 475 K. Also, with increase in pressure, the lifetime values seem to reach a saturation level for 298 and 355 K whereas no such thing

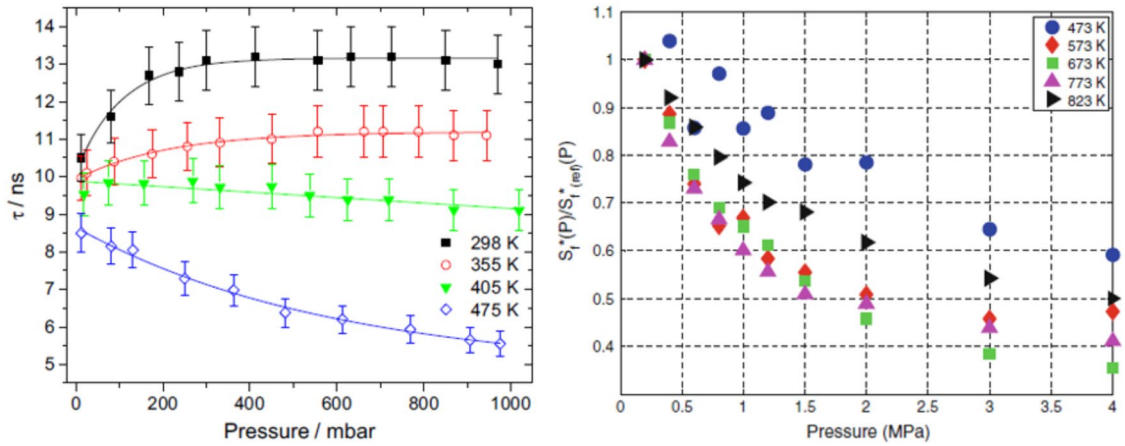

Fig. 16 Left image (from ref [73]) shows the effective anisole lifetime in pure carbon-dioxide bath gas till 1 bar pressure with increasing temperatures. Right image (from ref [18]) shows the relative fluorescence signals of anisole in carbon-dioxide bath gas with different pressures for increasing temperature

was observed for 405 and 475 K as the lifetime values are found to be in a steady decrement regime. For engine relevant conditions, fluorescence characteristics of anisole in combined high pressure and high temperature regimes need to be studied. Tran et al. (2014) [18] plotted the fluorescence signal variation for a temperature range of 473–823 K across a large pressure range from 2 to 40 bar at 266 nm laser excitation in carbon-dioxide bath gas. Each isotherm in the right image of Fig. 16 are obtained at a constant molecular density of 2.58×10^{16} molecule cm^{-3} m and are then normalised to their respective fluorescence signals at 2 bar. Unlike in the lower temperature cases, here a monotonic decrease in the fluorescence signals is observed with increase in pressure for all the temperatures concerned. Since the absorption-cross section values are insensitive to pressure changes, the change in fluorescence signals must be due to the change in FQY values. This suggests that in the temperature range of 473–823 K, the FQY shows a monotonic decrease with increasing pressures. Also, since each isotherm is normalised to a distinct value, the curves basically show a sensitivity to pressure changes. The sharper the fall, the more sensitive is the curve. Note that the relative FQY information obtained from these curves is different from the effective lifetime plots which are basically a measure of the absolute FQY values. From the plot, it can be observed that with increasing temperature, the isotherms become more sensitive to pressure changes. The sharpness of the fall becomes maximum at around 673 K and then starts to fall thereafter. The curve at 823 K is only more sensitive than the isotherm at 473 K. Furthermore, Tran et al. [18] also plotted the variation in relative FQY in different non-quenching bath gases (figure not shown here) like nitrogen, argon and carbon-dioxide at 4, 10 and 30 bar bath gas pressures. The authors found that there was no apparent influence of different bath gases on the evolution of anisole FQY in the temperature range of 473–823 K.

Discussion

Fluorescence models were developed for anisole molecule using the database created by the above discussed works. Such models can be used to perform quantitative studies using fluorescence imaging. Normally, there are three types of fluorescence models. An empirical or phenomenological model is developed using curve-fits to the experimentally obtained data and are valid in the same experimental pressure and temperature ranges. Such curve-fits involve low computational effort and help in analysing the experimental data. Faust et al. (2013) [80] developed such a model for anisole to compute relative FQY (FQY at 296 K and 1 bar pressure in nitrogen bath gas at 266 nm excitation will be unity). The model consisted of a product of three terms, the first of which accounted for FQY dependence with respect to temperature in 1 bar nitrogen bath gas, the second term accounted for pressure effects (other than 1 bar) in a nitrogen bath gas and the third term accounted for oxygen quenching using Stern–Volmer factors. The model results are shown in Fig. 14, where the model predicted FQY values are plotted with the experimental values. The model shows good agreement with experimental values at 1 bar nitrogen bath gas till 850 K and till 750 K for higher pressures. This shows that the model doesn't perform well for combined high pressure and high temperature regime. Furthermore, for oxygen containing bath gases, the model was tested for oxygen and nitrogen mixtures with total pressure of 1 bar and with oxygen partial pressures till 210 mbar. The right image of Fig. 14 compares the experimental data and the model predicted FQY values. It is found that the agreement is good for curves till 525 K. For higher temperatures, significant deviations are observed. This is explained by the fact that

at temperature beyond 600 K, the Stern–Volmer curves are no longer represented as straight lines [80] and thus there is no single Stern–Volmer factors (as the slope changes) at such temperatures. The inherent weakness of this model is the constant SV factor assumed at a particular temperature. The deviation from non-linearity of SV plots has also been observed with toluene at temperatures higher than 600 K for 266 nm excitation and at all temperatures for 248 nm excitation. The reason for the non-linearity is expected to be the same as that for toluene. At such high temperatures, there will be onset of internal conversions which will be further facilitated by internal vibrational randomisation. As a result, there will be occupation of various energy levels part of which will be dominated by IC (lower quenching probability due to shorter lifetimes) and others that will be dominated by ISC (larger probability of oxygen quenching). This results in a deviation from linearity of SV plots. Therefore, at higher vibrational energy levels (populated at higher temperatures), the rates of non-radiative de-excitation increases with temperatures and especially above 600 K where appreciable IC occurs. This greatly increases the non-radiative de-excitation rates especially after 600 K. This is very well observed in the effective lifetime plots of Fig. 14 which show a sudden drop after 600 K.

To understand the pressure dependency, vibrational relaxations (VR) need to be considered that arise from the collision of bath gas molecules with the excited state molecule. It is important to note that the absorption cross-section values remain unaffected by pressure changes. Therefore, any observed variation in fluorescence signal with pressure is solely attributable to the pressure dependence of FQY. This is true for the right image of Fig. 16. Elevated pressures lead to heightened rates of intermolecular vibrational relaxation due to more frequent collisions. During these collisions, molecules in their excited states lose energy and transition to lower vibronic levels within the S_1 state occurs. At these lower vibronic levels, the rates of ISC decrease, consequently increasing the FQY value. As higher pressures result in more collisions and enhanced vibrational relaxation, this accounts for the observed increase in FQY values with rising pressures. This is especially true for ketones (refer part A) where the energy gap between the 0–0 vibrational levels for S_0 to S_1 transition is lesser than aromatics (this has previously been explained to be the reason behind heightened oxygen quenching observed in aromatics). For anisole, the gap is about 36,394 cm^{-1} [88] and it is about 30,440 cm^{-1} for acetone [90]. The energy corresponding to 266 nm excitation is 37,594 cm^{-1} [73]. So, for anisole at room temperature, the energy provided by the molecule is more than the 0–0 band gap. Therefore, an increase in the effective lifetime curve can be seen with increasing pressures in the left image of Fig. 16 at the room temperature of 298 K.

In order to understand the influence of temperature on the pressure dependency of FQY, it is important to understand the behaviour of energy gap between the thermalised levels of S_0 to S_1 states. At a particular temperature, an average thermalized energy level can be associated with a molecule as shown in Fig. 9. If, the energy gap between the two thermalised levels of S_0 to S_1 states is less than the energy provided by laser excitation, then the molecule upon vibrational relaxation will drop down to the thermalised energy level in S_1 state showing an increase in FQY. But, Benzler et al. (2015) [73] found that the energy gap between the thermalised levels increases with increasing temperature mainly due to a larger shifting of thermalised energy level of S_1 state to higher energies due to a higher density of vibrational energy states in S_1. Therefore, the excess energy provided by laser excitation to anisole should begin to decrease with increasing temperatures. This would then result in a lowering of pressure dependency as can be observed in the effective lifetimes curve at 355 K of Fig. 16. With further increase in temperature, at a certain point the energy gap between the two thermalised levels of S_0 to S_1 states will become more than the energy provided by laser excitation. Then the molecule upon vibrational relaxation will be excited to a vibrational level lower than the thermalized level of S_1 state commonly referred to as photo-induced cooling. This was also observed earlier for toluene molecule. Under such situation, upon collision with the surrounding bath gases, the molecule gains energy and moves higher up to the thermalised level. This results in a decrease of FQY with increasing pressures at such temperatures. This can also be seen for temperatures of 405 and 475 K in the effective lifetime plots of Fig. 16. Therefore, when the molecules are excited farther away from the thermalized level, a large pressure sensitivity is observed. Once the molecule has reached the thermalized level upon collision, no further change in FQY values are observed with further increase in pressure.

From above 400 K, there will be pressure induced reduction of FQY values which will directly result in reduction of fluorescence signal values. This is observed in the right image of Fig. 16 where all the curves are found to show a decline with increasing pressure. Here, each plot is normalised to its respective value at 0.2 bar pressure in nitrogen bath gas. Therefore, the curves can be used to compare the relative sharpness or alternatively the pressure sensitivity. The sharper the fall, the more pressure sensitivity is observed at that temperature. Thus, from the curves it is seen that the pressure sensitivity (sharpness of the fall) increases from 473 K, becomes maximum at a certain temperature and then again reduces at 823 K. This type of a non-monotonic behaviour in pressure sensitivity is also observed for acetone in the works of Hartwig et al. [91, 92] (refer part A) under combined high temperature and high pressure regimes. This can be explained by the decreasing collision rates at higher

temperatures [80]. It can also be witnessed by the non-monotonic behaviour of anisole fluorescence lifetime values in air with increasing temperature (see Fig. 14) which first increase followed by a decrease with increasing temperature. This can be better seen in the exploded figure in top right corner as demarcated by blue arrows in the right image of Fig. 14. The initial rise in fluorescence lifetime is due to a drop in oxygen quenching from reduced collisions at elevated temperatures after which a drop in fluorescence lifetime is observed due to a faster non-radiative rate at such high temperatures.

As an improvement to the empirical model by Faust et al. [80], Wang et al. (2017) [74] put forth a semi-empirical model similar to the step-ladder model put forward by Thurber [90] and Koch [72] for ketones. According to the model, FQY (ϕ) for anisole is evaluated by Eq. (8) which calculates the sum over all N vibrational levels in the excited singlet state occupied by an average molecule as it decays similar to the model for toluene as discussed in Eq. (7).

$$\Phi = \frac{k_{\mathrm{fl}}}{k_{\mathrm{fl}}+k_{\mathrm{vib}}+k_{0_2}+k_{nr,1}+k_{\mathrm{IVR},1}} + \sum_{i=2}^{N-1}\left[\frac{k_{\mathrm{fl}}}{k_{\mathrm{fl}}+k_{\mathrm{vib}}+k_{0_2}+k_{\mathrm{nr},i}+k_{\mathrm{IVR},i}}\prod_{j=1}^{i-1}\left(\frac{k_{\mathrm{vib}}}{k_{\mathrm{fl}}+k_{\mathrm{vib}}+k_{0_2}+k_{\mathrm{nr},j}+k_{\mathrm{IVR},j}}\right)\right] + \frac{k_{\mathrm{fl}}}{k_{\mathrm{fl}}+k_{0_2}+k_{\mathrm{nr},N}+k_{\mathrm{IVR},N}}\prod_{j=1}^{N-1}\left(\frac{k_{\mathrm{vib}}}{k_{\mathrm{fl}}+k_{\mathrm{vib}}+k_{0_2}+k_{\mathrm{nr},j}+k_{\mathrm{IVR},j}}\right) \tag{8}$$

k_{fl} represents the fluorescence rate constant and is assumed to be constant with vibrational energy level. $k_{\mathrm{nr},i}$ represents the non-radiative decay rates at the *ith* energy level. k_{0_2} represents the quenching rate constant due to oxygen. k_{vib} represents the rate constant for vibrational relaxation and $k_{\mathrm{IVR},i}$ represents the intramolecular vibrational randomization at *ith* energy level. For detailed calculation of every rate constant, one can refer to the original reference [74]. Wang et al. [74] used the semi-empirical model and calculated the normalised fluorescence signal values for combined high pressure and high temperature for anisole over a temperature range from 473 to 823 K and a pressure range from 0.2 to 4 MPa (figure not included). They found that the model was able to predict the decrease in signal values with increasing pressures but the amount of decrease was found to be over-predicted at higher temperatures of around 773 K possibly due to an over-estimation of k_{nr} at the mentioned temperatures. The model predicted a reduction in the FQY values by around two orders of magnitude in the same temperature range. The authors suggested that this might be due to efficient k_{nr} or due to k_{IVR}. Therefore, further refining of the proposed anisole model is needed backed by a more extensive set of experimental studies. One possible modification to the step ladder model of Wang et al. for anisole was proposed by Baranowski et al. [93] where they suggested a modification in the effect of the laser excitation. Wang's model had assumed a complete transfer of the population of S_0 to S_1 states. However, Baranowski et al. suggested that due to a narrow bandwidth laser excitation, only a limited number of possible absorption cross-section transition overlap with the laser bandwidth because of which only a part of the S_0 population is transferred to S_1. Incorporating this change led to a more accurate determination of the thermalised vibrational energy level of S_1.

4 Naphthalene and 1-methylnaphthalene

Till now, mono-aromatic compounds were discussed. In this section, a di-aromatic compound naphthalene and its methylated derivative will be discussed. Naphthalene is a di-aromatic compound and is present in A1 kerosene (1.9% by mass) that is commonly used in aviation [94]. In diesel, the naphthalene content varies from 6.6 to 1600 mg L^{-1} [95]. In unleaded gasoline, naphthalene is present in 1% by vol [38]. Naphthalene vapour was used by Ni and Melton [96] in turbulent nitrogen flows for two dimensional temperature imaging. Kaiser et al. [97] used FARLIF method to determine the qualitative instantaneous single shot and averaged equivalence ratio distribution images for a mesoscale burner using 1-methylnaphthalene as the tracer and dodecane as the surrogate fuel representing JP8 fuels. Naphthalene was used to perform laser induced exciples fluorescence (LIEF) in a swirl flow based lean combustion gasoline engine for imaging mixture formation [98]. Shimizu et al. [98] studied fuel distribution in a Toyota lean burn engine using a swirl control valve. Closing the valve generated high swirl in the cylinder. They injected fuel at 40 CAD ATDC with an equivalence ratio of 0.8 to simulate lean operation and observed the effect of swirl on droplet behaviour. High swirl led to rapid droplet breakup and vaporization, resulting in no droplets by the end of the compression stroke and a mostly homogeneous mixture at 300 CAD. Without swirl, droplets remained localized and less vaporized, leading to inhomogeneous vapor distribution and droplets visible at the end of compression. Fuel droplets also impinged on the cylinder walls in both cases. Controlled high swirl improved mixing, evaporation, and reduced in-cylinder inhomogeneities.

The properties of 1-methylnaphthalene match diesel fuel very well and therefore was used in diesel engine applications. For the purpose of application to PLIF in diesel surrogate fuels, Trost et al. [99] reported that 1-methylnaphthalene is a promising tracer. They used 1-methylnaphthalene as a tracer for a mixture of primary reference fuels for diesel. The authors suggested that at the high pressure and temperature conditions in diesel sprays, there will be limited preferential evaporation as the diesel surrogates and 1-methylnaphthalene are all non-polar molecules. The boiling range and enthalpy of vapourization of 1-methylnaphthalene and diesel fuels match well [20]; 1-methylnaphthalene is also

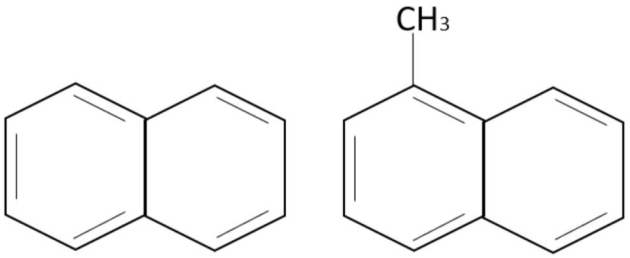

Fig. 17 Schematic diagram of naphthalene molecule is shown in the left image. Right image shows the same for 1-methylnaphthalene

quite stable against pyrolysis at high temperatures [100]. 1-methylnaphthalene is easy to blend owing to its liquid state at room temperature [101] in contrast to naphthalene that is solid. Also, naphthalene is more hazardous than 1-methylnaphthalene. The authors also stated that 1-methylnaphthalene has a higher absorption cross-section than their mono-cyclic counterparts like toluene, a high fluorescence signal intensity, almost linear temperature dependence, a negligible pressure dependence and a high thermal stability which becomes very important as very high temperatures are obtained at the end of the compression stroke of a diesel engine. Naphthalene and 1-methylnaphthalene were used in LIEF for diesel sprays by Melton and Verdiect [102] and Payri et al. [103]. Trost et al. [99] used naphthalene for fuel distribution imaging in an optical diesel engine and were able to study the mixture formation process subsequent to pilot injection. Lind et al. [104] used 1-methylnaphthalene as a tracer to simultaneously determine the temperature and fuel partial density in a diesel spray using an optical injection chamber under relevant conditions found in diesel engines but by using heated nitrogen as bath gas. Lower temperatures and a higher fuel partial density was found at the spray core whereas at the spray periphery, the temperature approached close to the ambient temperature along with a lower fuel partial density owing to higher mixing. Due to the presence of a second ring, the fluorescence spectrum of naphthalene is normally red-shifted from mono-aromatics [64]. Owing to the utility of di-aromatic fluorescence to study both IC engines and gas turbine combustors, it becomes imperative to review the several works that were undertaken to characterize the fluorescence emanating from naphthalene and its derivative 1-methylnaphthalene in this section. Figure 17 shows the schematic diagram of both the molecules.

4.1 Absorption cross-section

Orain et al. [105] measured the absorption cross-section of naphthalene for 266 nm laser excitation and also determined the temperature dependence in a range of 350–900 K. For 266 nm excitation, the photon energy corresponds to about 37,594 cm^{-1}. For naphthalene the energy gap between S_0 and S_2 state is 35,806 cm^{-1} [106]. Hence, 266 nm laser excitation will lead to an excitation into the second singlet state. Orain et al. [105] measured an absorption cross-section between 1.25×10^{-17} and 1.35×10^{-17} cm^2 in the mentioned temperature range. Suto et al. [107] measured the cross-section to be about 1.4×10^{-17} cm^2 at 300 K for 266 nm excitation. Grosch et al. [108] studied the variation of naphthalene absorption spectrum with temperature. They studied the spectrum in the wavelength range of 200–320 nm in a range of temperatures from 297 to 773 K. Two different absorption features was observed in two separate wavelength regimes. Only the longer wavelength regime is presented in this review as most of the excitation wavelengths used in PLIF studies are covered by the longer wavelength region. However, it should be noted that the shorter wavelength part of the spectrum is stronger by an order of magnitude as compared to the long wavelength part. Figure 18 plots the variation of absorption spectrum with increasing temperature. It is observed that at low temperature of 297 K, there are several features in the spectrum. With increasing temperature, the peaks gradually disappear so much so that at 773 K, a smooth featureless curve can be seen. The spectrum also experiences a redshift along with a broadening with temperature which results in a higher absorption cross-section towards the red end of the spectrum. The authors further found that the maximum absorption cross-section wavelength shifts from 210.7 nm at 297 K to 212.6 nm at 773 K with the maximum cross-section value showing a decrease from 4.95×10^{-16} to 3.47×10^{-16} cm^2/molecule.

Quite recently, Retzer et al. [109] have measured the variation of absorption spectrum of 1-methylnaphthalene with temperature. Dry air was used as a carrier gas in the temperature range of 350–500 K and pure nitrogen for 500–850 K. The temperature was varied in steps of 50 K with the pressure being maintained at 0.4 MPa. No surrounding gases effect on absorption cross-sections was observed. The wavelength range considered was from 230 to 330 nm. Figure 18 shows the absorption spectrum of 1-methylnaphthalene. Similar to naphthalene, the spectrum at low temperatures show several features. At 350 K, three peaks at 264, 274 and 285 nm were observed. With increasing temperature, the structures begin to disappear and there is a broadening of the spectrum with a slight redshift a behaviour also witnessed like that for naphthalene. The redshift causes a shift in the maximum value from 274 nm at 350 K to 275 nm at 850 K. The authors suggested that the redshift with temperature is due to the higher vibrational energy at higher temperatures in the ground electronic state. This results in a lesser energy requirement for the excitation to the first excited state. This is manifested as the redshift. The smoothening of the curves with temperature was explained as more molecules were available in the higher vibrational levels and the corresponding reduction in energy gaps between the higher

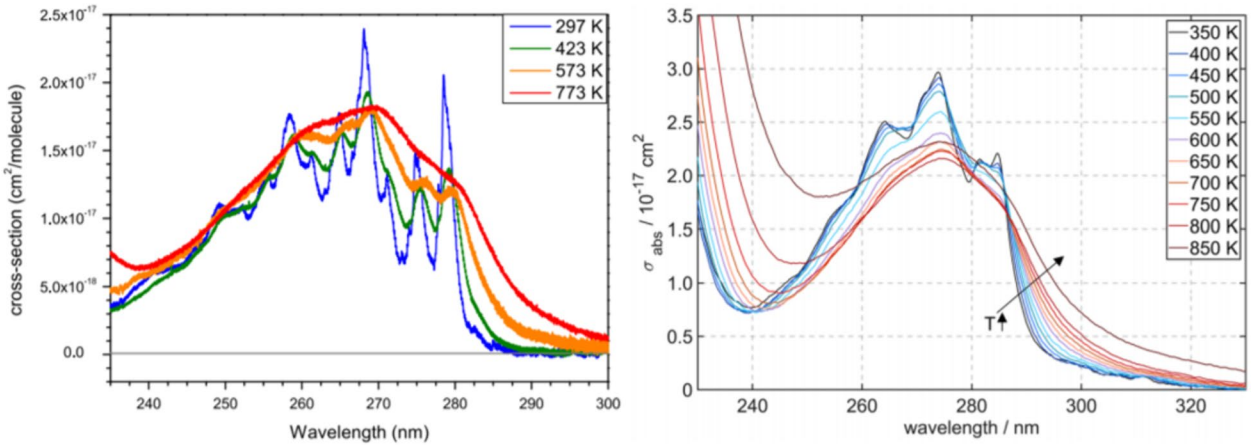

Fig. 18 The left image shows the absorption spectrum of naphthalene from the works of Grosch et al. [108]. Adapted from [108] with permission from Elsevier. The right image shows the same for 1-methylnaphthalene from the works of Retzer et al. [109]

vibrational energy levels. After 800 K, there is a significant overlap of the spectrum from S_0 to S_2 level. This would result in an increase in absorption spectrum in the studied wavelength range at very high temperatures especially after 800 K range. To study the absorption cross-section evolution for 266 nm with temperature, the variation is shown in Fig. 19 for both the compounds from the works of Orain et al. [105] for naphthalene and Retzer et al. [109] for 1-methyl naphthalene.

From the figures, it is clear that the absorption cross-section of 1-methylnaphthalene is greater than that of naphthalene at 266 nm excitation. However, their behaviour looks similar with rising temperatures. For naphthalene, it is observed that the cross-section value doesn't change much and varies non-monotonically. Orain et al. explained this behaviour as a result of the shifting of absorption peaks with temperature owing to the highly featured spectrum. However, Zhang et al. [19] found a linear increase in cross-section value for 266 nm in the temperature range of 673–1373 K whereas the results of Orain et al. show an increase only after 800 K. This further suggests that naphthalene cross-section values show an increasing trend at very high temperatures. For 1-methylnaphthalene, the cross-section at 266 nm doesn't change much in the temperature range of 350–500 K. In this range, the maximum cross-section value is observed at 450 K with a value of 2.45×10^{-17} cm^2. After this, a reduction of about 20% is found in the range of 500–800 K. After 800 K, a rise in cross-section can be seen. This is very similar to the naphthalene behaviour.

4.2 Fluorescence signal variation

For naphthalene, despite the excitation to the second singlet state, the emitted fluorescence signal is mostly emitted from the first singlet state due to rapid internal conversions from S_2 to S_1 state [110]. Figure 20 shows the evolution of fluorescence spectrum with temperature for 266 nm excitation from 350 to 900 K in a nitrogen bath gas at atmospheric pressure with increasing temperature normalised to the individual peak value.

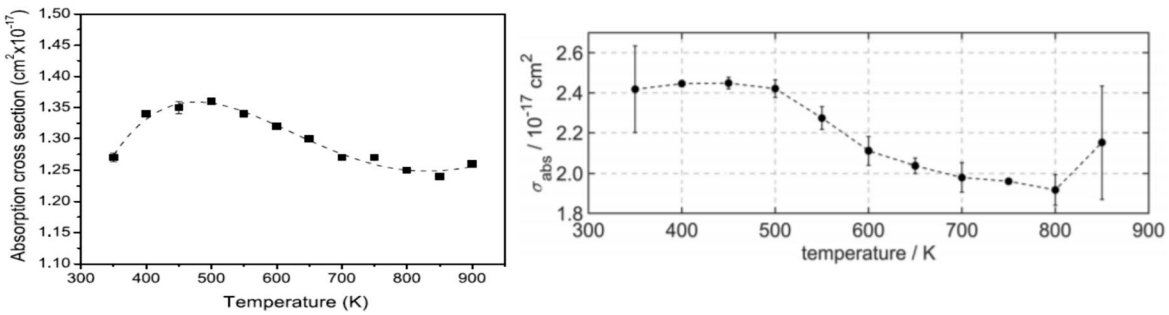

Fig. 19 The left image show the absorption cross-section at 266 nm temperature for naphthalene from the works of [105] and the right image is for 1-methylnaphthalene from the work of [109]

Figure 20 shows the red shifting of spectrum with temperature along with a smoothening of the spectrum at higher temperature. At low temperatures, there is a definite feature that can be observed at 320 and 335 nm. With increasing temperature, the intensity reduces monotonically along with a loss of structure with the spectrum becoming essentially broadband at higher temperatures. The peak intensity is found to shift by 20 nm whereas the redshift is about 5 nm per 100 K. A similar redshift and temperature broadening was also observed in the works of Ossler et al. [111]. They observed that FWHM of naphthalene emission spectrum increases 30 to 50 nm and the peak position shifts from 328 to 348 nm in a temperature range of 430–1210 K. Orain et al. [112] and Koban et al. [54] measured the redshift in the fluorescence spectrum of 124-trimethylbenzene and toluene respectively and found that it is about 2 nm per 100 K. Thus, the di-aromatics are found to be more temperature sensitive to redshift in emission spectrum than mono-aromatics. Uy and Lim [113] observed redshift in naphthalene spectrum with increasing excitation energy even covering to the second or third excited singlet states. Once in the S_2 and S_3 states, there is a rapid Internal conversion after which the molecule ends up in very high vibrational levels of S_1 state as the energy is not lost during transition. The inherent shapes and anharmonicity of the Morse potential curves cause the radiative transition from S_1 to S_0 state to be redshifted and smoother when the fluorescence is from higher vibronic levels. This reasoning was extended by Rossow [64] to explain the redshift with increasing temperature as higher temperatures cause the molecules to occupy higher vibrational levels of S_1 state.

Figure 20 also plots the integrated fluorescence intensity in the wavelength range of 290–400 nm as a function of increasing temperature. Since the absorption cross-section at 266 nm was found to be temperature insensitive, any change in fluorescence signal with temperature can be attributed to a change in FQY. A monotonic drop in signal values is observed with temperature. This can be explained due to increasing non-radiative decay rates with increasing vibrational energy level of first excited singlet. Uy and Lim [113] suggested that with increasing excitation energy, higher vibrational levels are occupied below which there will be a greater number of triplet manifolds opening up many channels of ISC. This would increase the vibronic interactions and with a greater Franck–Condon overlap factors at higher levels, the ISC rate would increase. Enhanced Franck–Condon overlap factors at higher vibrational levels would also lead to enhanced IC. The increasing IC and ISC rates with vibrational level was also indicated by [111]. Orain et al. [105] found that the drop in signal intensity was lesser as compared to mono-aromatics like toluene. Hence, naphthalene fluorescence signal intensity is less temperature sensitive than the mono-aromatics.

Orain et al. [105] reported the variation of fluorescence spectrum with increasing oxygen content in the bath gas at 450 K such that the total pressure was maintained at 0.1 MPa (Fig. 21). Each spectrum is normalised to its maximum value. It is found from Fig. 21 that the fluorescence signal reduces with increasing oxygen partial pressures accompanied with a corresponding redshift. The redshift was found to be about 10 nm when the oxygen mole fraction varies from 0 to 21% and saturates at an oxygen partial pressure of 10–12%. [111] found the redshift to be about 4 nm and [114] found it to be about 7 nm above 500 K. In comparison, for mono-aromatics the redshift observed for 1,2,4-trimethylbenzene is 1 nm [112] for same range of oxygen partial

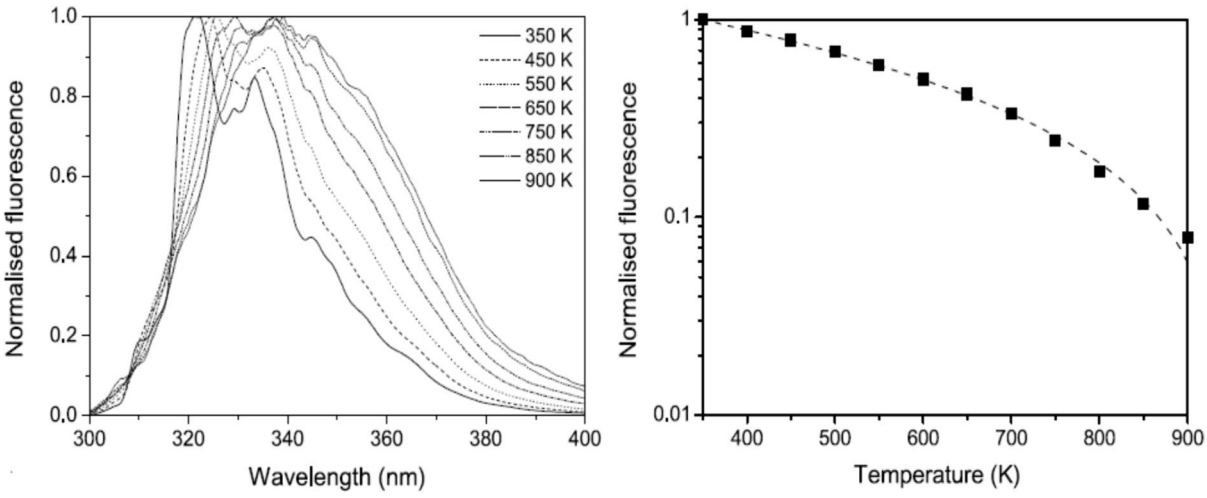

Fig. 20 [105] Left image shows the redshift of naphthalene fluorescence spectra normalised to the respective maximum values with temperature and the right image shows the evolution of fluorescence signal intensity with temperature. Nitrogen was used as a bath gas and the temperature range covered was from 350 to 900 K at 0.1 MPa

pressure and 266 nm laser excitation. The authors also observed that the drop in naphthalene fluorescence intensity is about one order of magnitude larger than the mono-aromatics like 1,2,4-trimethylbenzene. This shows that the effect of oxygen quenching is greater on naphthalene. The authors suggested that since the lifetime in the first excited state is larger for naphthalene than the mono-aromatics, it therefore was more susceptible to oxygen quenching. The structures observed in pure nitrogen bath gas are found to disappear with increasing oxygen partial pressures as they result from fluorescent transitions with a strong coupling between energy levels and hence a correspondingly longer lifetime. This makes it highly susceptible to oxygen quenching. The high oxygen quenching experienced by naphthalene is good news for its applicability in FARLIF technique. Based on this, Orain et al. also obtained Stern–Volmer plots which are not shown here for brevity. The plots were linear and no deviations were observed from linearity unlike toluene Koban et al. [59]. With increasing temperature, the slopes reduced indicating the increase of the relative strength of non-radiative decay rates compared to oxygen quenching. Similar observation was found by Kaiser and Long [114]. The SV factor was found to be 396 bar^{-1} at 450 K. This suggests that di-aromatics are certainly preferable to mono-aromatics from the point of view of FARLIF.

Similar studies about the fluorescence spectrum was carried out for 1-methylnaphthalene. Retzer et al. [20] studied the temperature dependence of fluorescence spectrum for 1-methylnaphthalene in a nitrogen bath gas and with air with an equivalence ratio of 2 (Fig. 22). The temperature range covered is from 398 to 798 K at a pressure of 1 MPa. Each spectrum is further normalised to its maximum value to better depict the redshift. It is observed that the spectrum ranges from 300 to 400 nm at a temperature of 398 K. With increasing temperature, a redshift and broadening is observed for both nitrogen and air and nitrogen mixture. A similar redshift was also observed in the works of Lind et al. [104] where they found that the fluorescence spectrum shows two peaks at lower temperatures and then each peak broadens and merges with ecah other at higher temperatures. The authors reported a redshift of about 4 nm per 100 K. The temperature induced redshift can be explained by a similar reasoning used in the naphthalene context. The redshift is larger in the presence of oxygen. The authors suggested that there is oxygen quenching of 1-methylnaphthalene fluorescence, the rate of which also increases with vibrational energy level. At higher temperature, thus the signals emanating from the higher vibrational levels are easily quenched by oxygen as a result of which, the difference in the spectral shift of the nitrogen and nitrogen and air mixture gradually reduces.

Lind et al. [104] found that the observed redshift in spectrum increases with increasing oxygen content or with decreasing equivalence ratio. Similar results were obtained by Kaiser and Long [114] where they found a redshift due to oxygen presence. The redshift was larger than that observed for naphthalene showing an additional 4 nm per 100 K spectral shift as compared to naphthalene fluorescence

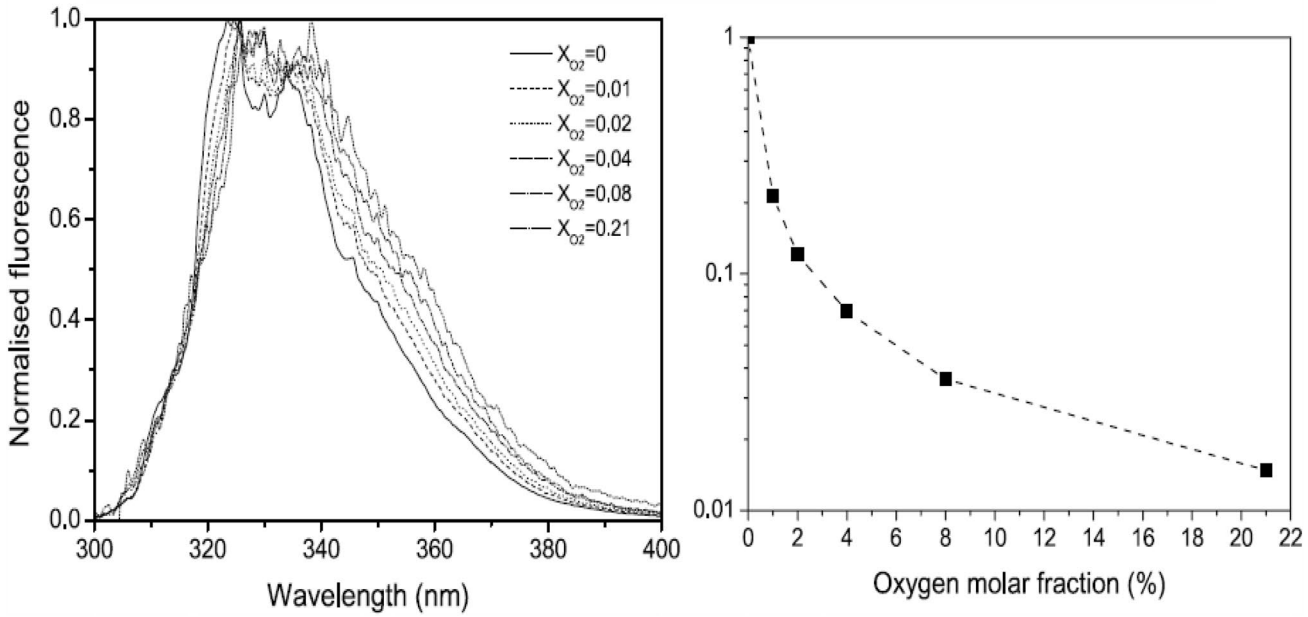

Fig. 21 [105] Left image shows the changes in naphthalene fluorescence spectra each normalised to its own maximum and the right image shows the evolution of fluorescence signal intensity with increasing oxygen content at 450 K

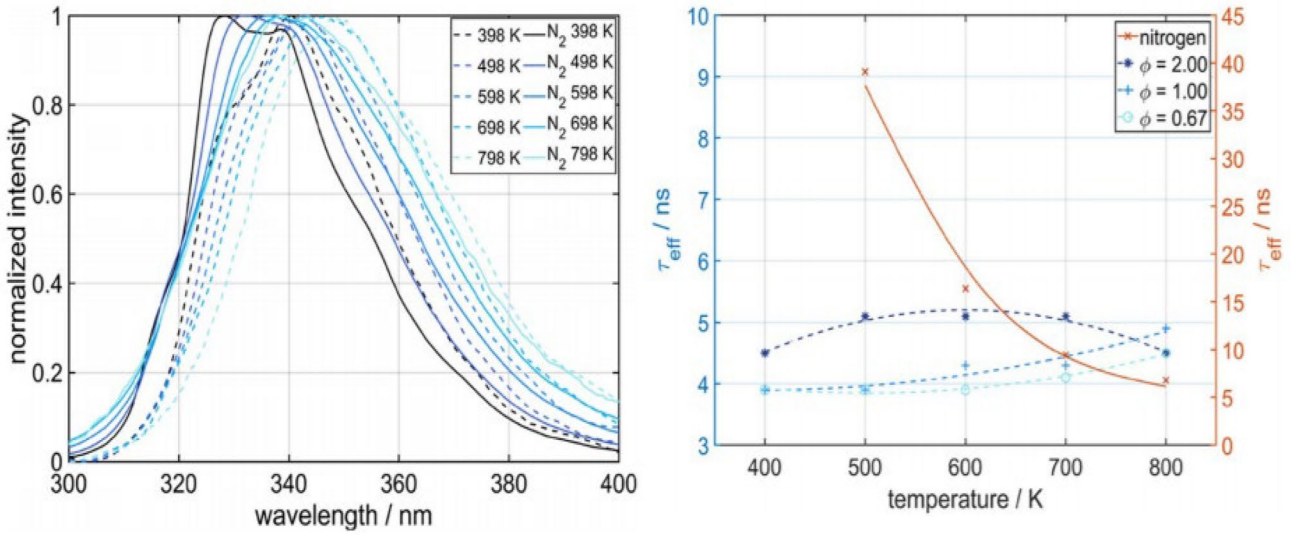

Fig. 22 [20] Left image shows the normalised fluorescence spectrum of 1-methylnaphthalene variation with temperature. Right image shows the variation in lifetime values with temperature in the presence of different bath gases

spectrum. The authors found that the total fluorescence signal for 1-methylnaphthalene with a unity equivalence ratio remains more or less unchanged till 600 K and then decreases monotonically with a futher temperature increase. Figure 22 further plots the effective lifetime data with temperature at varying oxygen concentrations. As seen earlier, effective lifetime data closely corresponds to the variation in absolute FQY. It is observed that in pure nitrogen atmosphere, the decay times reduce with tempertaure increase. The authors suggested that this is due to the increased rates of ISC at higher vibrational levels as it was also seen in the case of naphthalene. The absolute FQY of naphthalene and 1-methylnaphthalene at 293 K is 0.42 and 0.4 respectively [89].

With introduction of oxygen in the bath gas, there is a drastic reduction in effective fluorescence lifetimes suggestive of very high quenching. With decreasing equivalence ratio, a slight reduction in fluorescence lifetimes is also observed. Nonetheless, the decay times do not change much with temperature for all the three equivalence ratios presented due to a strong quenching. The authors also found a strong SV factor further corroborating the high oxygen quenching effect on 1-methylnaphthalene. The SV factor as found by Kaiser and Long [114] was 1410 MPa^{-1} at 500 K. This makes 1-methylnaphthalene a suitable compound for FARLIF technique. However, since FARLIF depends on the strength of oxygen quenching, care must be taken for applicability at high temperatures. As it was seen for toluene, the non-radiative decay rates grow with temperature so much so that they become comparable to oxygen quenching rates. In this context, SV factor for 1-methylnaphthalene was observed to reduce at higher temperatures with the SV factor being 369 MPa^{-1} at 800 K [114].

Retzer et al. [20] studied the applicability of FARLIF methodology for equivalence ratio determination using 1-methylnaphthalene fluorescence. They studied the effect of temperature and pressure on fluorescence signals from 1-methylnaphthalene from the point of view of its applicability in FARLIF measurements. The results are shown in Fig. 23. The equivalence ratio in the study was varied by changing the amount of oxygen in the chamber and by adding nitrogen to maintain the required total pressure of the bath gas. The curves in the left image of Fig. 23 plots the fluorescence signal intensity variation in the temperature range of 498–798 K and at various equivalence ratios ranging from 0.66 to 3.33. The pressure was maintained constant at 1 MPa. Every signal is normalised to 1 MPa and 498 K at $\phi = 1$. This will enable to compare the signal strengths at various conditions. It was found that the linear relationship of signal with equivalence ratio was obtained for $\phi = 0.6–1.66$. At higher equivalence ratios, the curves show a diminishing slope and deviation from linearity. Thus, deviation from FARLIF is observed at higher equivalence ratios. This is due to the lesser oxygen content at higher ϕ values indicative of lower oxygen quenching and the growing importance of other non-radiative deactivation rates.

At a particular equivalence ratio, the evolution of the signal with temperature shows a non-monotonous variation. This is observed from the changing slope and offset of the calibration curves. In a temperature range of 498 to 648 K, the slope and offset of each curve increases and at temperatures above 648 K, the slope and offset again start to decrease. The authors suggested that the initial rise is

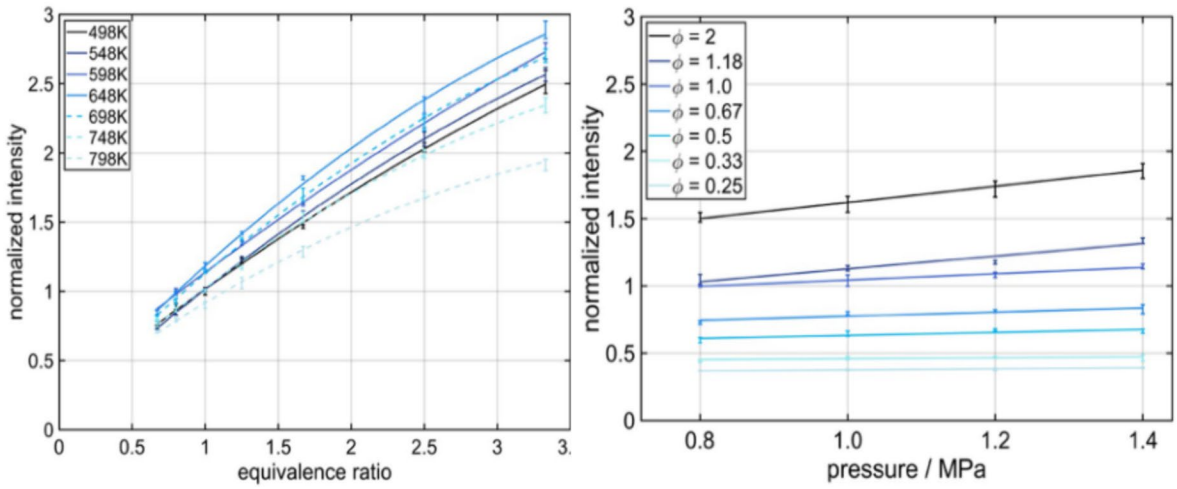

Fig. 23 [20] Normalised fluorescence signal intensities for 1-Methylnaphthalene. Left image shows the intensity variation at 1 MPa with temperature from 498 to 798 K for different equivalence ratio at a fuel partial density of 12.6 g/m^3. Right image shows the intensity variation at 498 K with varying equivalence ratio in a pressure range of 0.8–1.4 MPa at a fuel partial density of 6.7 g/m^3

due to signals becoming stronger due to a slightly increased absorption cross-section and increased broadening of the fluorescence spectrum with temperature. The fall at higher temperatures is due to a fall in signal strength due to a slightly reduced absorption cross-section and a reduction in FQY which more than compensates for the spectral widening. Another possible explanation provided is that with initial increase in temperature, the oxygen number density decreases causing a reduced quenching effect. The signal increase due to quenching reduction outweighs the decreasing effect of increased ISC with temperature, Hence, a signal rise is seen in the beginning. However, at very high temperatures, the large values of ISC (and possibly also IC at temperatures above 750 K) outweighs the decreased oxygen quenching effect and leads to a sharp drop in FQY value which results in a decrease of signal strength. This non-monotonous behaviour is seen for $\phi = 2$ curve of Fig. 22. This non-monotonic behaviour has also been observed by Faust et al. [63] for naphthalene. Furthermore, Trost et al. [99] plotted the normalised fluorescence signals for 1-methylnaphthalene over a temperature of 473–873 K at pressures of 1,2 and 3 MPa. The authors found that the decrease in fluorescence signal with temperature is almost linear with a reduction by factor 10 in the specified temperature regime. On the contrary, the dependence of pressure is very less (less than 15% signal increment) in the given pressure regime.

The right image of Fig. 23 shows a similar study performed at a constant temperature of 498 K and in a pressure range of 0.8–1.4 MPa with a fuel partial density of 6.7 g/m^3. The equivalence ratio was varied from 0.25 to 2. Each data point is normalised to the signal value at $\phi = 1$ and at a pressure of 0.8 MPa. It is found that at the lower equivalence ratios, no significant changes in signal intensity was observed in the range of $\phi = 0.25$–0.67. At higher equivalence ratios (from $\phi = 1$), the signal values are found to increase with pressure. For $\phi = 2$, a 25% increase in signal value was observed. The authors suggested that this increase in signal at higher ϕ values was due to lower oxygen content. This will result in a reduced oxygen quenching accompanied with a higher vibrational relaxation with increasing pressure. The higher relaxations due to intermolecular collisions increase the FQY value resulting in a stronger signal strength.

Figure 24 shows the evolution of naphthalene fluorescence spectrum with pressure at 450 K. The pressure range covered is from 0.1 to 3 MPa. The spectra are normalised to the maximum intensity value at 0.1 MPa. It is found that with increasing pressure, the fluorescence signal intensity monotonically increase for 266 nm excitation. No distortion of the spectrum shape is observed with the features effectively being preserved across the entire pressure range. The fluorescence signal intensity shows a steep increase till 0.7 MPa and more or less stabilises at a constant value after 2 MPa showing a change in signals by 1% in between 2 and 3 MPa. Since the absorption cross-section is both pressure insensitive and dependence on temperature is low, the change in signals is mainly due to variation in FQY. It is thus observed that the signal value increases and then stabilises for high pressure regimes. This means that the FQY undergoes pressure stabilisation unlike toluene which show a pressure destabilisation at 266 nm excitation.

Figure 25 plots the lifetime components of naphthalene and 1-methylnaphthalene from the works of Benzler et al. [73]. They used a 266 nm of picosecond laser excitation to obtain time resolved measurements of fluorescence intensity under a low-pressure regime of 1 mbar to 1 bar under various

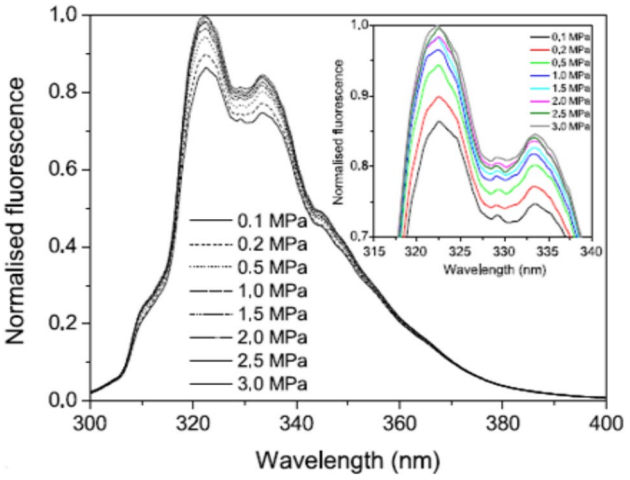

Fig. 24 [105]: Image shows the changes in naphthalene fluorescence spectra normalised to the maximum value of 3 MPa spectrum. Nitrogen was used as a bath gas and the pressure range covered was from 0.1 to 3 MPa at 450 K

temperatures. The authors attempted to determine the intrinsic photophysical rate constants pertaining to the non-radiative fluorescence decay processes in an environment of low pressures which would result in very less collisions for negligible vibrational relaxation rates. Upon a combination of a fixed laser wavelength and different temperatures, excitation to different vibrational levels of the excited electronic state could be achieved. Since fluorescence lifetime is directly proportional to FQY, the plots in Fig. 25 is also representative of the variation of absolute FQY. It was observed that the fluorescence from both the naphthalene compounds, shows a mixture of a short- and long-lived lifetime components. The long lifetime component was from the S_1 state whereas the short-lived component was expected from the S_2 state. Due to small energy gaps between S_2 and S_0 states, the second excited state was accessible with 266 nm excitation. Both were plotted as a function of pressure. However, in this article, only fluorescence from the S_1 state is discussed.

Discussion

In Fig. 25, each line is an isotherm as is indicated in the graph. It is observed that the with increasing pressure, the lifetime values increase suggesting an increase of FQY with pressure until it reaches a saturation for both naphthalene and 1-methylnaphthalene. The amount of increase also reduces with increasing temperature. The stabilization of FQY is due to excessive energy present in the laser excitation which is much more than the 0–0 transition energy. This leaves the molecule at a much higher energy level than the thermalised energy level of S_1. This results in increased vibrational relaxation with increasing pressure to the thermalised level from the initially laser populated level. With increasing temperature, the thermalised level of S_1 increases faster than that of S_0 increasing the 0–0 transition energy [73]. This reduces the excess energy available for vibrational relaxation as was explained in the toluene and anisole sections. This is manifested as the reduced FQY rise at larger temperatures and an early arrival of the saturation.

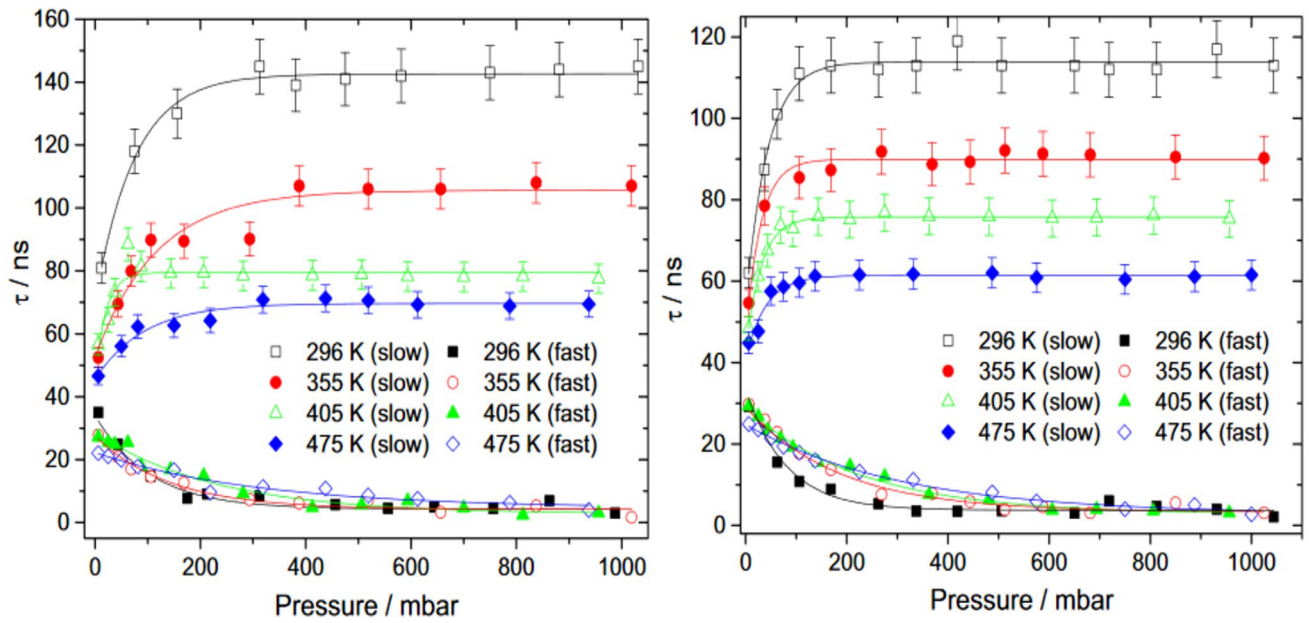

Fig. 25 [73] Fluorescence lifetime is plotted at a low pressure range from 10 mbar till 1 bar in a carbon-dioxide bath gas at 266 nm laser excitation for various temperatures. The left image is for naphthalene and the right image is for 1-methylnaphthalene. Both the slow and fast lifetime components are plotted

In order to model naphthalene relative FQY, Faust et al. [63] tried to modify the model proposed by Koban et al. [59] for toluene. Since the Koban model was limited to 1 bar total pressure, for higher pressures a multiplicative term was included that would consider the effect for higher pressures but would become unity at 1 bar total pressure. To accommodate the high fluorescence quenching by oxygen molecule, another factor was incorporated to account for the effect of variation of oxygen partial pressure and variation of SV factor with temperature. However, the curve fitting was limited to the experimental condition in that particular work and showed poor fitting with the experimental data at pressures above 1 bar. Benzler et al. [73] tried to explain their experimental results for a number of aromatic molecules using a step ladder model like that for the ketones. A photophysical cascade model for naphthalene similar to the one for toluene was developed by Rossow [64]. The functional dependence of both radiative and non-radiative decay rates were derived from low pressure fluorescence yield and lifetime measurements at room temperature at varying excitation wavelengths from the works of Hseih et al. [115]. For high pressure limit, data from Hall et al. [116] was used and for methane bath gas, data from Beddard et al. [117] was used. The model evaluates absolute FQY values at a temperature of 296 K and for 248 nm excitation with varying pressure. It predicts a low pressure and a high-pressure limit of FQY for different bath gas compositions. Bath gases of pure naphthalene and varying amounts of naphthalene concentration in nitrogen and methane gases were compared. It is found that with increasing complexity of the collider in terms of mass or the number of atoms present, the deviation from low pressure is observed earlier. This is due to the colliders become increasingly efficient. This behaviour was also observed for ketones (refer part A of this work).

Left image of Fig. 26 [64] plots the model predicted variation of absolute FQY as a function of excitation wavelength and pressure in nitrogen bath gas at 450 K. Both the high pressure and low-pressure limits can be identified. The high-pressure limit is wavelength independent in contrast to the low pressure. This result is very similar to those found for the ketonic compounds (refer part A of this work). A decrease in FQY with pressure for 308 nm is observed due to the phenomenon of photo-induced cooling. Therefore, the pressure effects can be studied either by varying temperature at a fixed laser excitation or at a fixed temperature at varying laser excitation. Benzler et al. [73] used the first methodology in their pressure effects study whereas Rossow used the second approach to develop plots for naphthalene. Both however successfully explained the pressure effects. In Fig. 26, two different pressure limits- high pressure and low pressure can be identified for FQY. At very low pressures, the collisions become rare and the fluorescence emanates from a vibrational level which is determined by the combination of temperature and excitation wavelength. This low value of FQY is the low-pressure limit. On increase of pressure, the collisions become significant and the FQY value deviates from the low-pressure limit. It then rises with pressure and at very high-pressure levels, reaches a high- pressure limit. This is due to the molecule being relaxed to the thermalized level of the excited electronic state. Both these limits are independent of the bath gas composition. The absolute FQY value of naphthalene in the low pressure limit was 0.35 and for

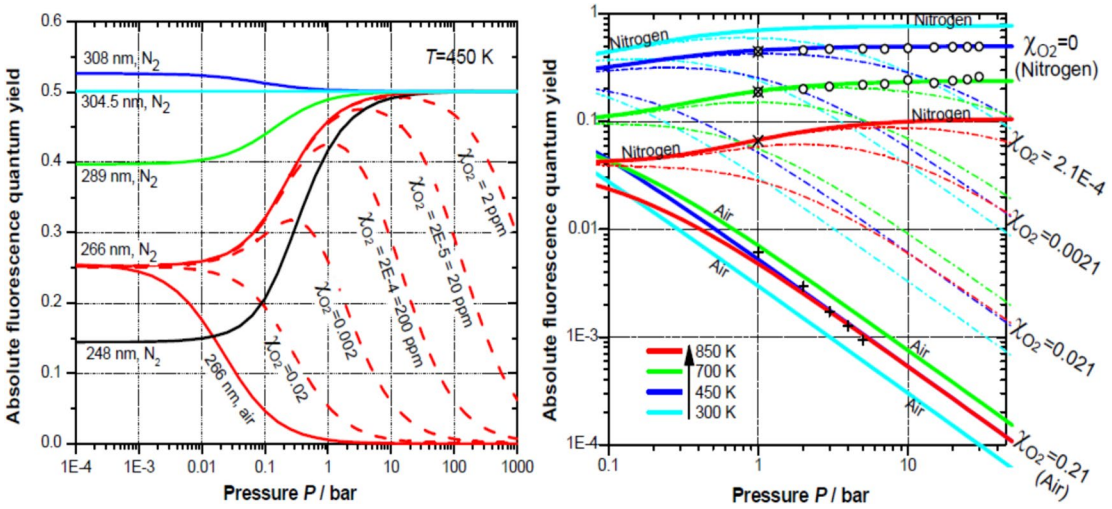

Fig. 26 [64] Model predicted pressure dependence of absolute FQY for naphthalene. Left image plots the dependence of FQY on excitation wavelength in nitrogen and varying oxygen content at 266 nm at 450 K. Right image shows the co position variation with different temperature at 266 nm excitation Reprinted with permission from Dr. Bjorn Rossow and Dr Frederic Grisch

high pressure limit was 0.79 at 248 nm excitation in the work of Hall et al. [116].

For 266 nm, a bath gas composition dependence is shown in the left image of Fig. 26. The dotted red lines are for different partial pressures of oxygen. With a mixture of oxygen and nitrogen, the FQY values are found to increase, reach a peak and finally decrease. The different behaviour is due to the quenching by oxygen. Since for 266 nm, there is a considerable vibrational excess energy associated, there is a competition between vibrational relaxation and oxygen quenching. At low total pressures and low oxygen concentration, there is a very less interaction with oxygen molecules resulting in a very small quenching. This leads to a complete dominance of vibrational relaxation causing the FQY to increase at low pressures. However, with increasing pressure, when the number of collisions with oxygen molecules become appreciable, then the quenching effect starts to appear, as a result of which a peak is observed followed by a monotonic decline in the FQY value. As the oxygen concentration increases, the quenching effect starts to overpower vibrational relaxation. As a result, the threshold pressure value after which quenching begins to dominate, gets shifted to lower pressures with increasing oxygen content. So much so that with air as a bath gas, there is no rise in FQY value. The curve begins to decrease right from the point where it starts to deviate from the low-pressure limit.

The right image of Fig. 26 shows the absolute FQY variation with pressure at 266 nm excitation and at 4 different temperatures of 300, 450, 700 and 850 K. The composition of bath gas is also varied from nitrogen to air with various proportions of oxygen in between. The temperature dependence of high- and low-pressure limits are observed where both decrease with increasing temperature. Pure nitrogen shows an increase of FQY value whereas pure air shows a monotonic decrease with pressure. The intermediate composition curves depart from the nitrogen curves at various pressure. The higher the oxygen content, earlier the deviation. The low-pressure limit is wavelength dependent whereas the high-pressure limit is wavelength independent. The low-pressure limit is determined by the vibronic level in which the electron is excited from the ground state. The excited state vibronic level is determined by temperature and energy content of the photon. Therefore, low pressure limit changes for different combinations of temperature and excitation wavelength. But high-pressure limit is found to vary only with temperature. This limit for FQY is achieved when fluorescence arises from the vibrationally relaxed level of excited singlet state. The vibrationally relaxed level in turn is determined by the surrounding temperature. Higher the temperature, higher is the energy of the vibrationally relaxed level because of the modified Boltzmann distribution in the excited electronic state. Therefore, high pressure limit changes with temperature. Since non-radiative decay rates are faster from the vibronic levels which are higher in energy; with increasing temperature, the high-pressure limit decreases as can be seen. At high temperatures, the FQY high pressure limits are lower and at a particular pressure, the FQY value reduces monotonically with increasing temperature. Hence, the isotherms for fluorescence signals are shifted progressively downward with temperature.

Finally, for comparing naphthalene and 1-methylnaphthalene, it is important to understand the effects of methylation as 1-methylnaphthalene is the methylated derivative of naphthalene. Orain et al. [105] studied the changes in fluorescence behaviour due to methyl substitution by comparing naphthalene, 1-methylnaphthalene and 1,3-dimethylnaphthalene. They found that as the number of methyl substitutions increase, the fluorescence spectrum gets redshifted. This happens due to reducing symmetry of the initially symmetric molecule upon methyl group additions which further hinders the forbidden transition [118]. Additionally, the increased number of methyl groups also increase the fluorescence signal due to a higher fluorescence rate constant [118]. The decrease of fluorescence signals with temperature increase is progressively more pronounced for 1,3-dimethylnaphthalene. Therefore, the temperature sensitivity gets enhanced. Oxygen was found to have a similar effect on all the three compounds with a high amount of quenching. The oxygen induced fluorescence spectrum redshift of 1-methylnaphthalene is 4 nm larger than naphthalene [114]. However, the SV factor of 1-methylnaphthalene at 450 K for 266 nm excitation was found to be 370 bar^{-1}, a value slightly less than naphthalene.

5 Fluoranthene

Till now, in the aromatic compounds the discussion was limited to the mono and di-aromatic ring compounds. The final section dealing with individual organic tracer is about fluoranthene. It is a poly-aromatic hydrocarbon with a five membered ring sandwiched between a single membered and double membered benzene ring. Figure 27 shows the schematic diagram of a fluoranthene molecule.

Fluoranthene has certain inherent advantages from a fluorescent tracer point of view. It has got a high thermal stability and a decent amount of fluorescent signals over a wide range of temperature and pressure observed in the works of Kuhni et al. [119]. Ni and Melton [120] used fluoranthene as the fluorescent tracer to obtain 2D images of fuel partial pressure and air partial pressure in a gaseous methane jet. Equivalence ratio maps were calculated from these images. The authors however suggested that the applicability of their method should be for an isothermal system due to the lack of data regarding the temperature influence of fluoranthene fluorescence lifetimes. Meyer et al.

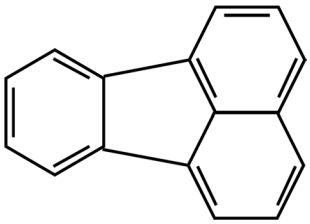

Fig. 27 Schematic diagram of fluoranthene molecule

[26] used fluoranthene as a tracer for performing PLIF to study fuel–air distribution in a PFI engine. They selected fluoranthene due to its high signal strength and low static, temperature and concentration quenching [26]. However, its fluorescence is significantly affected by oxygen quenching. After suitable correction of the signals, they could obtain images for air fuel ratio at different engine speeds, equivalence ratios and injection timings [26]. They investigated the effect of engine speed on mixture formation by quantifying the inhomogeneities in fuel–air ratio distribution in terms of standard deviation. They observed that the standard deviation showed a monotonic decrease with increased speeds due to enhanced turbulence intensity at higher speeds. They also found that in the studied equivalence ratio range, the spatial inhomogeneities increase as the overall equivalence ratio is made leaner. Finally, CCV in fuel distribution was found to increase when fuel is injected during open intake valve due to shorter available mixing times. As fluoranthene displays features for a potential tracer and its fluorescence can provide information about PAH formation and soot precursors [119], the current section discusses about its fluorescence behaviour. However, there is a very limited information available about the parametric study of fluoranthene fluorescence to the author's knowledge at the time of preparing this article. Hence, a major focus of this section will be to provide a detailed review of those works.

5.1 Absorption cross-section

Figure 28 shows the absorption spectrum of fluoranthene as determined by Kuhni et al. [119]. The spectrum has got several features which correspond to excitation till different singlet states. The absorption peak near 270–280 nm was denoted as transition from S_0 to S_4 state by Ruth and Wick [121]. The peak near 320 to 350 nm was attributed to both S_0 to S_3 and S_0 to S_2 transitions by Kolc et al. [122]. The spectrum longer than 400 nm can be associated with S_0 to S_1 transition [123]. Kuhni et al. [119] determined the spectrum at 3 different temperatures of 473, 573 and 673 K in a nitrogen atmosphere at 0.2 MPa. The authors observed an increase in absorption cross-section with temperature. Figure 28 also shows the dependence of the absorption cross-section on temperature at 266 and 355 nm. The plots show that the cross-section increases by 1.5% per unit temperature at 266 nm and by 3.5% per unit temperature at 355 nm. The temperature was extended in this plot till 873 K and each plot is normalised to its respective value at 473 K.

5.2 Fluorescence signal variation

Fluoranthene shows the phenomenon of dual fluorescence where fluorescence occurs from both the first and second

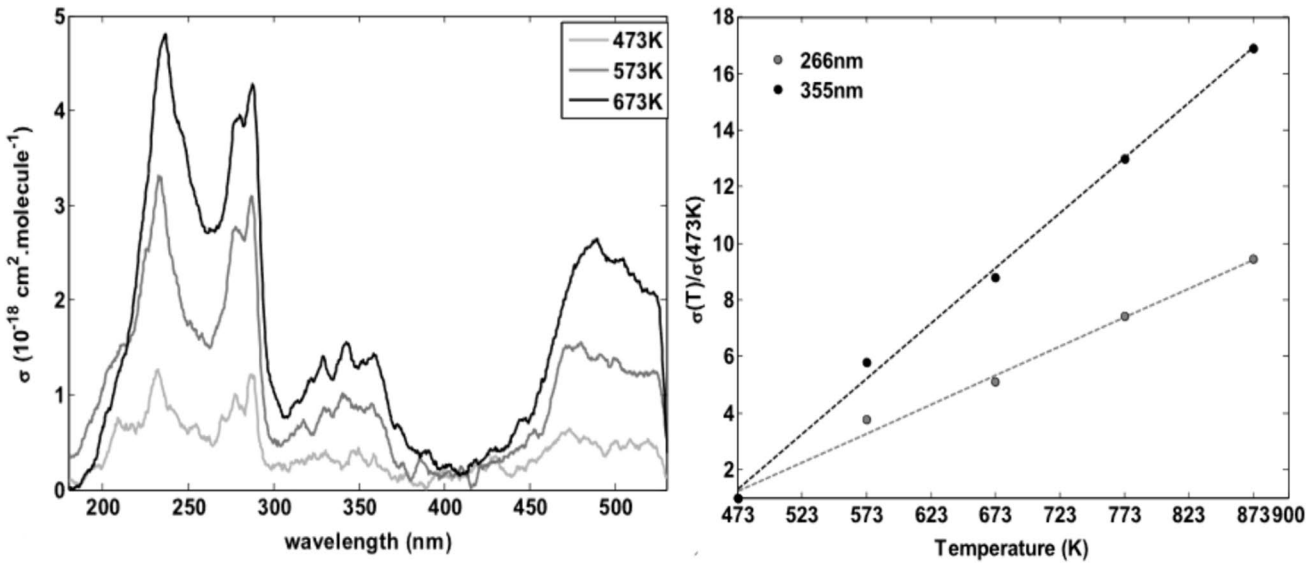

Fig. 28 (from ref [119]) Left image shows the variation of fluoranthene absorption spectrum with temperature and the right image shows the evolution of absorption cross-section with temperature

excited singlets to the ground electronic level. Philen and Hedges [124] have described the properties of the initial two excited singlet states of fluoranthene. The fluorescence from the S_1 state takes place between 405 nm and about 540 nm and has a duration of 58 ns, whereas the fluorescence from the S_2 state happens in the range of 370–395 nm and lasts for approximately 143 ns. Bark and Force [125] found that fluoranthene vapour in the absence of collisions shows fluorescence from both the first and second excited singlet states. This behaviour is in contrast to other complex molecules where the internal conversion from higher singlet states to S_1 state is very rapid resulting in fluorescence only from the S_1 state. The authors suggested that the rate of internal conversion between first and second singlet states is very slow so that fluorescence from S_2 is able to compete with it. The unusually slow internal conversion was explained due to a large change in bond lengths of molecules between the first and second singlet states affecting adversely affecting the Franck–Condon overlap factor. However, most of the fluorescence is contributed by deexcitation from the first excited singlet state and the distinct fluorescence emission from the second excited singlet state is visible only at very low pressures where there is a very little collision process [123]. Therefore, the discussions provided in this section will mainly deal with fluorescence from the first excited singlet state. Bark and Force (1993) [126] also stated that the fluorescence spectra shape for polynuclear aromatic hydrocarbons in solutions does not change with excitation wavelength and the decay lifetimes is normally independent of the emission wavelengths.

Figure 29 [119] shows the fluoranthene fluorescence spectrum. It ranges from 380 to 600 nm with a maximum at 450 nm corresponding to the de-excitation from S_1 to S_0 states. Furthermore, the excitation wavelength has no effect on the fluorescence spectrum domain and the wavelength at which the peak is observed. The temperature dependence of fluorescence intensity can be identified from the figure. It is found that with increasing temperature, the fluorescence intensity diminishes. Each spectrum is normalised to the maximum value at 473 K. The authors also plotted the variation of fluorescence intensities after suitable normalisation with the absorption cross-section which is also temperature dependent. The obtained values are then again normalised to their respective reference values at 473 K and then plotted with temperature for different pressures at 266 nm excitation wavelength in Fig. 29. Therefore, the curves essentially show the FQY variations. The plots show a decreasing behaviour with increasing temperature and the decrease is found to be larger at lower pressures. This same trend was also observed for 355 nm wavelength. The decrease was found to be about two orders of magnitude in the studied temperature range. The authors suggested the decrease could be attributed to the increased ISC rates at higher vibrational levels at higher temperatures. However, just like toluene, the transition in fluoranthene also involves $\pi \rightarrow \pi^*$ transition. Therefore, the authors indicated that the drastic decrease in FQY values

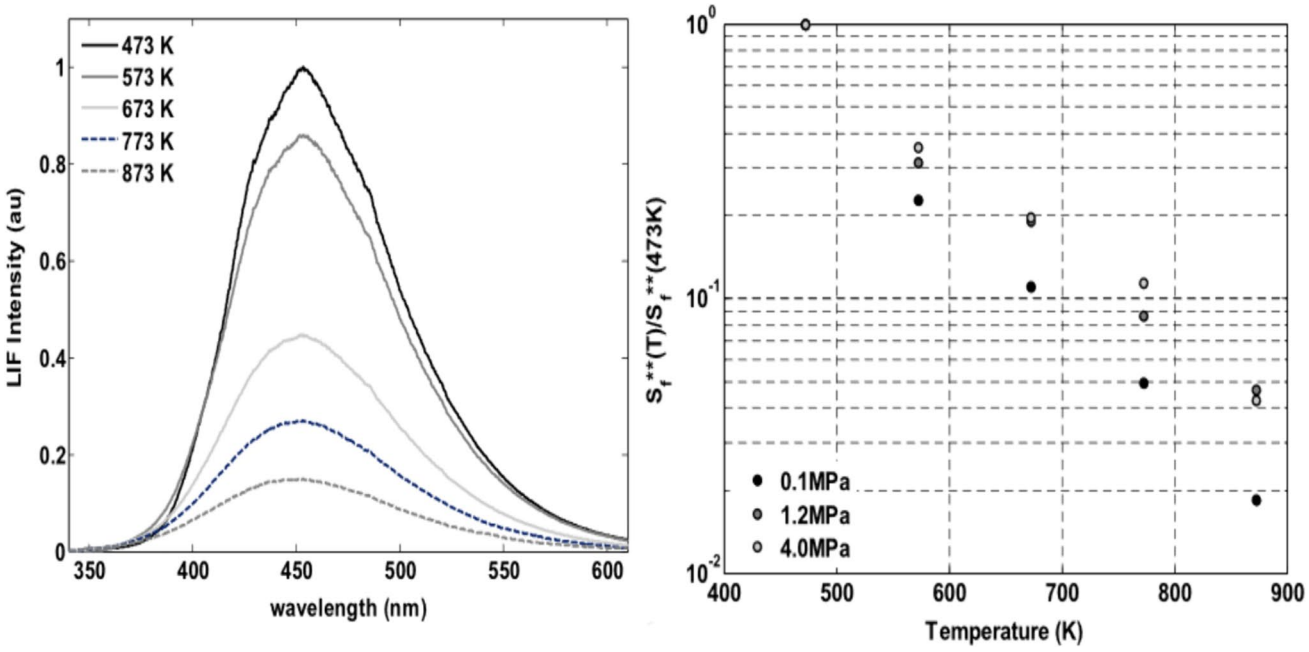

Fig. 29 (from ref [119]) Left image plots the fluorescence spectrum at different temperatures. The right image plots the normalised intensity values at three different pressures for 266 nm excitation in a nitrogen bath gas normalised at 473 K

is not just solely the result of ISC like it was suggested for toluene by Koban et al.

Figure 30 shows the pressure dependence of fluorescence signals. Fluorescence signal intensity was normalised with respect to the corresponding values at 0.1 MPa value for 266 nm excitation. Since the reference values used for normalisation are different, only the relative sharpness of the curves can be compared with each other and not the absolute magnitudes of the intensity. It is observed that with increasing pressure, the signal intensity increases. Since the absorption cross-section is insensitive to pressure, the behaviour of each isotherm is dictated by the behaviour of the FQY values at that temperature. The FQY increases with pressure due to the vibrational relaxation effect which results in an increase in number of excited fluoranthene molecules to fluoresce from the lower vibrational levels which have a correspondingly higher value of FQY. The signals increase with pressure, become saturated at a certain threshold pressure which again depends on the temperature. The signal intensity increases with pressure from about 0.1 to 1.5 MPa after which it either becomes constant or increases marginally depending on the temperature. This shows the approach of a limit of vibrational relaxation or the high-pressure limit values of FQY just like the ketones.

At higher temperature, some non-monotonous behaviour can be seen in the figure due to large standard deviations of the data points at high temperatures. Furthermore, the isotherms at higher temperatures and lower wavelengths seem to be more pressure sensitive. This is expected as the excitation energy increase results in a higher vibrational level which correspondingly provides more room for vibrational relaxation enhancing the pressure sensitivity. Similar results were also obtained for 355 nm excitation. However, the phenomenon of the pressure sensitivity increase with temperature, reaching of a maximum limit and then decrease of sensitivity with further temperature increase is not seen in the case of fluoranthene unlike that observed for acetone by Hartwig et al. [91] (refer part A). Therefore, further studies on high temperature high pressure regimes of fluoranthene fluorescence needs to be carried out.

Till now, the bath gas was fixed at nitrogen which is inert with respect to fluorescence quenching. Kuhni et al. also studied the influence of bath gas on fluorescence signal intensity. Bath gases like nitrogen, argon, carbon-dioxide, and ambient air were used for fluorescence study. Carbon-dioxide was chosen due to its presence in the exhaust gas residuals in IC engine cylinders. The fluorescence signal intensity was studied in these bath gases for a pressure range of 0.1–4 MPa and at a temperature of 473–873 K. Studies were also carried out in air for the same pressure range at a temperature of 473 K. Fluorescence quenching was observed only in air bath gas. The remaining three bath gases show an increase in fluorescence signals with pressure as expected. Figure 30 shows the variation of fluorescence signal with pressure for nitrogen, carbon-dioxide and argon at 266 nm excitation. Each curve is normalised to the respective value at 0.1 MPa and the temperature was fixed at 673 K. The curves show a similar pressure trend. The signals seem to increase with pressure quite significantly till 1.5 MPa after which it increases sparsely till 4 MPa. The relative sharpness of the curves shows the pressure sensitivity. Thus, nitrogen shows the maximum sensitivity and argon the least. The curve for carbon-dioxide is intermediate to both the curves. On comparison with the ketonic tracers [76], the pressure sensitivity should be increasing as the collider species consists of an increased number of atoms becoming

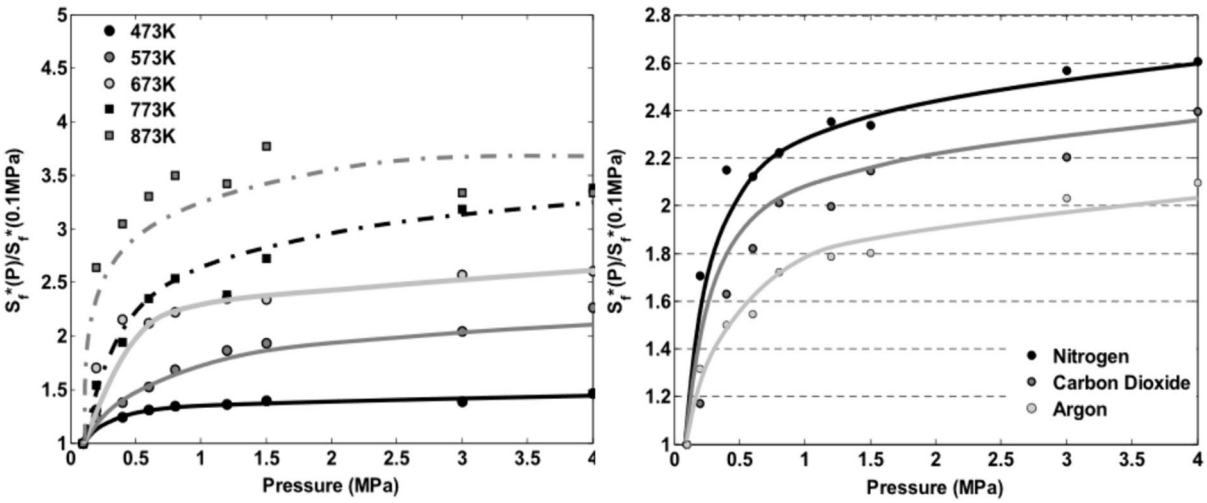

Fig. 30 (from ref [119]) Left image plots the normalised fluorescence signal variation with pressure at different temperatures in nitrogen bath gas. The right image plots fluorescence signals at 673 K for different pressures and non-quenching bath gases. Both the data are at 266 nm excitation

more complex. With this understanding, the sensitivity in carbon-dioxide bath gas should have been highest among all the studied bath gases. The reason for this discrepancy is not clear as of now and more studies are needed in this domain.

Presence of oxygen in bath gas is expected to reduce the fluorescence signal intensity due to quenching. The reduction in signals is due to the oxygen assisted inter-system crossings providing an additional pathway for the de-excitation of the excited fluoranthene molecules. Kuhni et al. found that the fluorescence signals reduce by about 80% in between 0.1 and 1.2 MPa of air bath gas at 473 K. Figure 31 shows the normalised fluorescence signal plotted with respect to 0.1 MPa signal level at both 266 and 355 nm excitation.

However, the study of fluoranthene fluorescence requires further data as the data provided by Kuhni et al. is the only work where a detailed parametric study was performed according to the author's knowledge. A step ladder model similar to the ketones was attempted by Zhang et al. [19] for fluoranthene. The model predicted FQY values matched well in the temperature range of 673–1373 K at one atmosphere pressure. However, the prediction of FQY values were limited to this condition only. Therefore, more data is needed to prepare a FQY model as it was done for the previous tracers and also to validate the above discussed work.

6 Application in IC engines

Till now, the individual fluorescence characteristics of tracer molecules were discussed in both the articles (part A and part B) of this work. The current section provides a brief overview of the applications of PLIF in IC engine

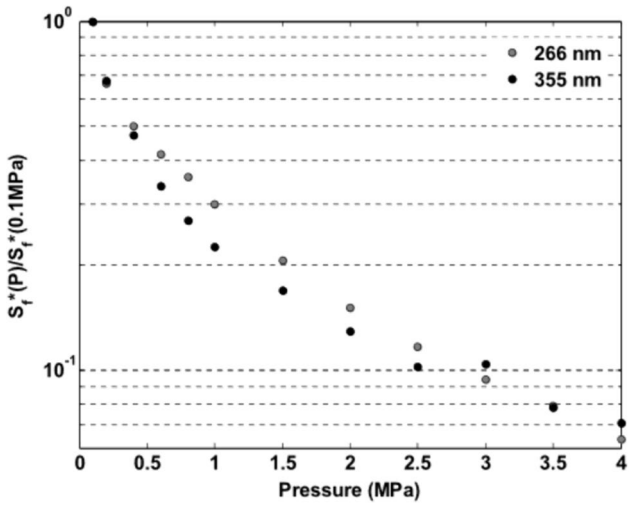

Fig. 31 (from ref [119]) Variation of fluorescence signal with pressure at different temperatures in air bath gas at 473 K

studies. As discussed, PLIF is effectively used to study both fuel–air mixture distribution and evaluate in-cylinder temperature distribution. In some cases, PLIF signals have further been used to measure the in-cylinder distribution of residual gases. For carrying out such measurements, various methods can be adopted depending on the characteristic behaviour of the tracer that is selected. For fuel distribution measurement, in-situ calibration [84, 127] and fuel–air ratio laser-induced fluorescence (FARLIF) [40, 41, 128] has been used. If fuel concentration is of interest, then carbonyl compounds find extensive usage due to their relative oxygen quenching insensitivity. This makes the fluorescence signals insensitive to composition changes. FARLIF requires that oxygen quenching is the preponderant photophysical process and thus requires a class of compounds which has a very high propensity to oxygen quenching. Aromatic compounds become very useful in this regard. Schulz and Sick [1] have explained the difference in the quenching sensitivity of these two classes of compounds due to the difference in the energy gaps between the excited singlet and triplet manifolds. The larger the energy gap, the more is the probability of quenching. Aromatic compounds have a much larger energy gap as compared to the ketonic compounds. Furthermore, the low energy gap in carbonyl compounds result in a very fast ISC rates.

In-situ calibration for fuel distribution imaging

In this method, at a particular crank angle, a series of images are captured with a specially prepared homogeneous mixture for different equivalence ratios. Such images are referred to as flatfield images. These fluorescence images have already incorporated the effects of variations in pressure and temperature with crank angle on fluorescence signals and no additional corrections regarding them are required (images have to be corrected for background noise and laser shot-to-shot fluctuation though). The flatfield images can then be temporally averaged and the strength of the fluorescence signal in the average corrected flatfield image obtained can be related to the equivalence ratio maintained. Now, the equivalence ratio can be varied to obtain different average flatfield images of varying mixture strength. These average images can be used to check the linearity of the signal with respect to the fuel concentration resulting in a calibration curve for a particular crank angle. Such fluorescence intensity curves can then be used to quantify the fluorescence signals in the region of interest at that specific crank angle. This same procedure can be repeated for all the desired crank angles and similarly every crank angle will have a separate calibration curve. It should however be noted that such flatfield images are also used for calibration during imaging of fuel–air ratio and in-cylinder temperature, topics which will be discussed shortly. Using the in-situ calibration technique as described above, calibration curves can be obtained for different crank angles

as shown in Fig. 32 (from ref [129]). Pradheep et al. [127] used this technique to study mixture distribution inside a PFI engine using 3-pentanone as the tracer. They determined the quantitative fuel–air mixture distribution under part throttle and low speed engine condition at different swirl planes in a small bore PFI engine. It was observed that the mixture was found to be richer near the intake valve and to the area opposite to the spark plug. Both spatial inhomogeneities and cycle-to-cycle variations (CCV) were observed to be high during the intake stroke but they reduced considerably towards the end of the compression stroke. A significant amount of fuel was also found to travel downwards along with the piston. Weaver et al. [130] also used this technique to perform fuel distribution imaging for a cold start study in a PFI engine. Their work can be referred to for the detailed image processing methods and relevant equations.

Fujikawa et al. [129] conducted PLIF experiments to visualize the fuel distribution at different crank angles during the compression stroke in a PFI engine. The results showed that the dual-injector setup where both the intake ports have an individual injector resulted in a more homogeneous fuel distribution compared to the single-injector setup where only one of the intake ports was provided with an injector. For a single injector configuration, a fuel stratification was obtained with rich mixture close to the engine side with the fuel injection port and this stratification was maintained mainly due to the existence of a tumble flow. The authors concluded that adjusting the ratio of injected fuel quantities from the two injectors could effectively control fuel distribution within the combustion chamber. A strong rotary motion of flow (like swirl and tumble) results in enhanced mixing in the plane of flow but limits mixing in a plane perpendicular to the flow along its cylinder axis [83]. Therefore, a strong swirl flow results in stratification along the cylinder axis which is referred to as axial stratification and a strong tumble flow causes stratification across tumble planes referred to as barrel stratification. In Fujikawa et al., a strong tumble flow essentially produced barrel stratification and restricted mixture on one side of the engine.

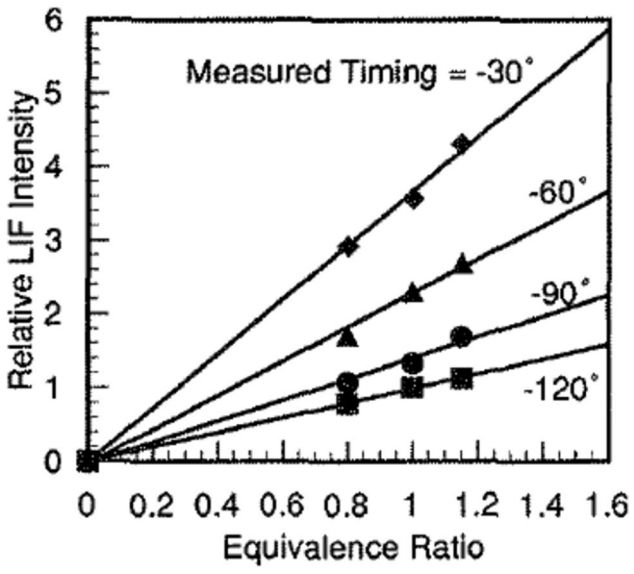

Fig. 32 (from ref [129]) Relative fuel intensity plotted as a function for different equivalence ratios at different crank angles. Reprinted from [129] with permission from SAE International

Lean burn methods are proposed for both Port fuel injection (PFI) and Direct injection (DI) engines to meet stringent emission standards and improve fuel economy. However, achieving combustion stability in lean burn mode at part loads is challenging. Researchers have focused on in-situ measurements of fuel–air mixture near the spark plug as well as CCV of fuel–air mixture distribution. Johansson et al. [131] conducted PLIF studies in a PFI engine, linking CCV in combustion to variations in mixture distribution at the spark plug. Berckmuller et al. [132] performed quantitative studies in a lean burn PFI engine, finding that cycles with richer mixtures at the spark plug resulted in higher combustion pressures. Garg et al. [133] did qualitative PLIF studies in a small-bore PFI engine at low load (25% throttle opening) and low speed (1200 rpm) conditions in a swirl plane and found significant CCV of mixture distribution. Further investigations by Hokimoto et al. [84] using simultaneous PLIF and TR-PIV techniques revealed that near the spark plug, where flame development occurs, the equivalence ratio during low load cycles was lean, leading to slower flame growth. Additionally, a reverse tumble flow opposing the main flow was observed for lowest load cycles, causing the spark plug region to become increasingly devoid of fuel mixtures. Haramiishi et al. (2019) [134] found that CCV in combustion is influenced by CCV in mixture distribution and turbulence kinetic energy (TKE) distribution. They noted that variation in TKE, due to changes in tumble vortex centre, was more significant than variation in fuel concentration regarding combustion CCV. This is because in PFI engines, where fuel has more time to mix with air, CCV in fuel distribution is lower. However, in DI engines, where the fuel has very less time to mix, CCV in fuel distributions are expected to have a stronger impact on combustion CCV.

In the aforementioned studies in PFI engines, laser frequency of the order of 10 Hz was enough to study mixture formation. In order to study the combustion CCV in stratified DI mode, images are captured in the order of milliseconds to study spray behaviour and subsequent mixture formation. This requires high speed lasers that can produce beams at kHz ranges. Smith and Sick [135] tried to obtain fuel distribution images for consecutive crank angles in the same cycle in a gasoline direct injection engine. They used a high-speed CMOS camera and a high repetition Nd-YAG laser capable of producing pulsed lasers at 355 nm at

12 kHz. They therefore used biacetyl as a tracer as 355 nm falls well within its absorption spectrum (see part A). They studied the fuel distribution in a spark ignited direct ignition engine with images being taken at an interval of 1 CAD. With such a high temporal resolution, the authors could track the motion of fuel plumes inside the cylinder in a particular engine cycle. The resulting motion could clearly suggest the persisting squish and counter-clockwise tumble flow. Smith and Sick [136] measured the fuel mixture distribution in late injection for stratified mode and found significant mixture inhomogeneity around the spark plug. In a follow up study [137], the authors further studied the impact of spark plug orientation and injector orientation on combustion using mixture distribution images. The authors found that the misfires were due to abnormal spark behaviour. When the spray plumes straddle the spark plug instead of directly hitting it, the misfires were found to greatly increase. Furthermore, Peterson et al. [138] investigated misfire (MF), well-burnt (WB), and partial-burnt (PB) cycles in stratified mode combustion using simultaneous PLIF and PIV. The researchers found that the spark energy was adequate to create a flame kernel in all three cases. In WB cycles, the flame kernel quickly spread into a combustible mixture within the piston bowl, crucial for subsequent combustion. PB cycles exhibited delayed interaction with the combustible mixture, causing it to become lean and leading to incomplete fuel consumption. MF cycles displayed a flame kernel surrounded by fuel-lean mixtures, significantly impeding flame propagation and ultimately causing flame extinction. The authors identified lean mixture clouds, nitrogen dilution, and unfavourable flow fields near the spark plug as key factors contributing to slow flame development and its subsequent propagation into the fuel–air mixture clouds for PB and MF cycles.

In addition to PFI engines, PLIF has also been extensively used to study various mixture formation concepts and the processes involved in gasoline direct injection (GDI) engines. Hiraya et al. [139] investigated mixture formation in a stratified spray-guided mode using a circulation mixture formation concept. In this approach, fuel is injected into a bowl or cavity on the piston during the compression stroke at high pressures. The injected fuel forms a jet that impacts the center of the bowl bottom, then propagates tangentially along the base, curls up along the walls of the bowl, and evaporates, creating a vaporized fuel cloud over the bowl region. This created a fuel-rich mixture near the spark plug region. They varied the injection pressure from 20 to 100 MPa and studied its effect on mixture formation using LIF studies. The results showed that higher injection pressures resulted in faster formation of a fuel vapor cloud, while lower pressures required more time for mixture formation. Additionally, they found that the injection pressure and timing had a combined effect on combustion stability, with stable combustion achieved within a relatively wider operating region at higher pressures and longer time gaps between injection and ignition timing. Conversely, for a smaller time gap between injection and ignition, a mixture cloud had not formed near the spark plug. This study therefore provides a glimpse of the combined effect of injection pressure and timing on combustion stability.

Additionally, fuel–air mixture distributions are greatly affected by in-cylinder flows. Kampanis et al. [140] conducted research on fuel distribution in a small-bore direct injection (DI) engine equipped with a 5-valve arrangement, focusing on early intake injection under different engine speeds and in-cylinder swirl flows. They observed significant fuel impingement on the piston surface (expected because of the small engine size), leading to a rich region near the piston. At 1500 rpm, a weak tumble directed the rich mixture upward, resulting in a central rich region within the cylinder. Additionally, air induction during the end of injection pushed the fuel-rich regions, concentrating them in the center of the cylinder. At 3000 rpm, increased spray dispersion led to slightly less inhomogeneity, but the tumble flow remained insufficient to eliminate the concentration gradient. However, under high swirl conditions (with a swirl ratio of 5.5), rapid vaporization significantly reduced the film and minimized fuel distribution inhomogeneity. Yang et al. [141] studied the qualitative fuel distribution in a stratified mode using flash boiling spray at different swirl ratios. The authors found that a high swirl was beneficial to form a repeatable fuel–air mixture stratification but at low swirl, the fuel–air mixture was more random. A strong organised flow thus has the potential to reduce the CCV of mixture distribution.

Kim et al. [75] further investigated the influence of in-cylinder flow fields on mixture distribution. They observed that mixture distribution developed differently in early injection for both tumble and swirl-dominated flows, but by the late compression stroke, the distributions became similar. For late injection, tumble flow was slightly more effective than swirl for stratified charge formation, while swirl flow had a greater impact on fuel sprays compared to tumble flow. In the works of Ritter et al. [142] difluoro benzene (DFB) was used to perform in-situ calibration PLIF to track the fuel distribution evolution. The charge cloud was found to rotate in a vertical plane along with the tumble motion with continued mixing. Therefore, tumble seems to be quite important in a GDI engine especially for homogeneous operation mode with an early injection as most of the injected fuel settles in the lower cylinder region near the piston crown (fuel spray penetration is higher due to lower in-cylinder pressure). A stable tumble of sufficient strength therefore has the potential to transport the rich mixture from the lower ends to the upper portion of the cylinder near spark plug. Therefore, it can be seen that both swirl and tumble flows have their distinctive effects on mixture formation processes and are

required to be studied individually for engine depending on the specific geometry of the combustion chamber.

Lately, hydrogen as an alternative fuel is receiving attention for its application in DI engines due to reduction in carbon-dioxide emissions. Study of mixture formation in such engines was performed with acetone PLIF. Salazar and Kaiser [143] investigated how different injector designs and injection timings affect fuel distribution. They noted that increasing the number of injector holes led to greater fuel concentration dilution due to increased mixing of ambient air by the fuel jets. However, employing too many holes, such as with a 13-hole injector, resulted in spray collapse due to significant jet–jet interaction caused by their close proximity. Tumble flow played a crucial role in upwardly moving the mixture that had otherwise descended with piston motion during the intake stroke. During injection in the compression stroke, tumble flow weakened and failed to bring up the rich mixture region near the spark plug. In a subsequent study,

An inherent assumption associated with the in-situ calibration technique is the spatial homogeneity of in-cylinder pressure and temperature. Pressure is mostly uniform and can be easily measured with the help of pressure transducer. However, the assumption of uniform temperature must be further looked into. During the intake stroke, a significant amount of residual gas from the previous combustion cycle is trapped inside the cylinder. There can be provisions of recycling of exhaust gases as well. A complete mixing of these residuals with the fresh charge is not possible especially in the intake stroke. Since these residual gases are at a higher temperature than the fresh charge, their insufficient mixing will give rise to a significant amount of non-uniformity in temperature and mixture composition. This will further lead to variations in fluorescence signals even for the same fuel concentration values. This problem can be mitigated by selecting tracers whose fluorescence properties are quite insensitive to bath gas composition. Ketones serve this purpose well owing to their high rates of inter-system crossing making them less susceptible to oxygen quenching. But the change in fluorescence intensity due to temperature variation needs to be accounted for. The methods for temperature imaging using PLIF will be discussed shortly.

For non-fired operations, when the objective is to determine the fuel concentration distribution, the minor temperature inhomogeneity can be taken care with a suitable combination of tracer and excitation wavelength such that the resulting fluorescence signal strength becomes less sensitive to temperature. Fujikawa et al. [129] compared the relative signal strength dependence of acetone, 3-pentanone and toluene with temperature and pressure at 266 and 248 nm excitation in air bath gas. Their results are shown in Fig. 33. At 473 K, the pressure sensitivity of acetone and 3-pentanone are almost same whereas, at 1 MPa, the temperature sensitivity of acetone is slightly less than 3-pentanone. Toluene shows a very high sensitivity for temperature and pressure. The sensitivity at 266 nm was found to be further lower than 248 nm as expected. Therefore, a combination of 266 nm and acetone would be best from the perspective of temperature insensitivity. Pressure sensitivity is less important than temperature sensitivity as pressure remains more or less constant across the cylinder chamber and its effect with changing crank angles during the compression stroke can be captured with the help of suitable flatfield images.

Under firing conditions, neglecting the temperature corrections will adversely affect the uncertainty in measurements. Additionally, using in-situ calibration method involving ketones, under a high presence of exhaust residuals in firing operations, the measured fuel concentration cannot be converted into fuel–air ratio as the distribution of oxygen itself will be highly non-uniform inside the cylinder. To determine fuel–air ratio distribution, FARLIF method using aromatic compounds become helpful.

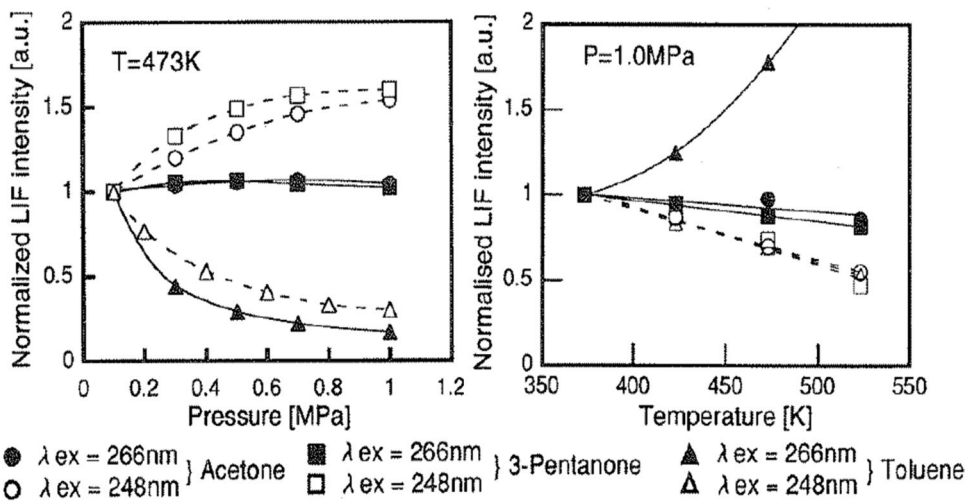

Fig. 33 [129] Relative fluorescence signal intensity for acetone, 3-pentanone and toluene are plotted for 266 and 248 nm excitation in air bath gas. Left image shows pressure dependence at 473 K and the right image shows temperature dependence at 1 MPa. Adapted from [129] with permission from SAE International

FARLIF method for equivalence ratio imaging

FARLIF was introduced in Sect. 1 and it depends on the preponderance of oxygen quenching over other fluorescence deactivation mechanisms. FARLIF has the potential to directly image fuel–air ratio thus providing this crucial information in environment with varied oxygen concentration (in regions dominated by exhaust gas residuals). Since then, the method has become quite popular and has been used to perform several studies. Reboux et al. [16, 40] proposed the FARLIF (fuel–air ratio laser-induced fluorescence) technique to quantitatively obtain the equivalence ratio over a measurement plane using toluene as a tracer. Mederer et al. [144] investigated the charge motion interaction with residual gas concentration in a GDI engine with an overall stoichiometric equivalence ratio. The injection timing was fixed at − 300 CAD ATDC of compression. The authors were able to observe that at − 205 CAD of compression, two separate mixture clouds extended from each intake valve to its corresponding opposite exhaust valve. This bifurcation was still found to exist at −165 CAD. Although, the authors did not provide explanation about the formation of two separated charge clouds, it seems likely that since the injector was positioned almost at the centre, fuel injected from two symmetrical halves of the injector accumulate under two intake valves symmetrically and the tumble motion tries to prevent the mixing of these two clouds along its axis similar to barrel stratification [83]. However, with swirl flow, a rotational motion was imparted to the charge clouds which resulted in their gradual mixing over the swirl plane. Higher the swirl intensity, faster was the mixing of the mixture clouds resulting in a quicker attainment of a homogeneous mixture than the pure tumble case. Better homogenisation improved combustion and thus augmented the EGR tolerance capability which is particularly helpful for controlling NO emission. Koch et al. [145] also studied the impact of different flow fields on mixture distribution using FARLIF technique with triethylamine (TEA) as the tracer. The injection was performed in the intake stroke and resulted in a significant impingement of piston top and subsequent vapourization (close proximity of piston to injector in early intake stroke as well as high spray penetration in the prevailing low in-cylinder pressures). In the first case, when the engine had only tumble flow, the tumble flow was found to convect the mixture from the piston crown to the top near spark plug region by the early compression stroke. After this the tumble flow decomposed towards the later compression stroke resulting in a localisation of a richer mixture near the spark plug. In the second case, the in-cylinder flow had a combined swirl and tumble flow fields, the swirl flow restricts the rich mixture near the piston crown and doesn't allow the tumble to carry it upwards. During compression stroke, the tumble starts to decompose but the swirl persists till late compression stroke. Thus, the swirl creates an axial stratification in which the rich mixture will be restricted at the piston crown and the spark plug region will be relatively leaner. This is not a favourable mixture condition. As a solution to this, the authors split the injection into two such that the large part of fuel was injected in the intake stroke and small part was injected in the late compression stroke. In the late compression stroke, due to high density, the penetration is limited and the spray plume is restricted close to the spark plug. This rich region near the spark plug is then preserved by the swirl flow which now does not allow the fuel to convect to the piston crown area. Therefore, by split injection, a relatively rich and ignitable mixture could be created in the flow conditions persisting in this particular engine. It is to be noted that if the second injection had a larger mass of fuel, then the penetration would be larger and the fuel would no longer localise near the spark plug. Therefore, the injection split ratio is also important to have a favourable mixture at the spark plug.

Lately, usage of biofuels like ethanol as a blend with gasoline is receiving attention due its renewable nature with a potential to reduce carbon-dioxide emissions [146]. Storch et al. [147] studied the mixture distribution for pure iso-octane and E20 (20% ethanol in iso-octane). They found that for E20 the mixture formed at ignition timing is much more stratified as compared to iso-octane. E20 is found to show enhanced evaporation as compared to iso-octane due to non-ideal mixing behaviour. The faster evaporation led the ethanol spray to have very limited penetration during the compression stroke in comparison to iso-octane spray. Since the mixing time available was less in the stratified mode, a very compact mixture cloud was formed for E20 away from the spark plug. For E20, a lean mixture was present in the spark plug vicinity and the rich cloud mixture was located close to intake cylinder walls. This close proximity of walls might result in increased heat losses because of which E20 droplets might remain unevaporated. This was then explained as the reason behind a larger soot formation than iso-octane in the study. For the particular engine condition, E20 generated slower flame speeds and a higher COV (in spite of the fact that laminar flame speeds are higher in ethanol than iso-octane) as the iso-octane mixture cloud was rich near the spark plug region. Later on, Storch et al. (2016) [146] extended this study to different ethanol blends of E20, E85 and E100 along with pure iso-octane and found different extent of mixture stratification for the various blends.

The above works clearly show the utility of FARLIF in mixture distribution studies. Nonetheless, it has certain limitations. Since a high collisional quenching is required, the pressure needs to be large enough, Reboux et al. [16] found that the technique is applicable for pressures above 2 bars. This way they could find the spatial fuel–air ratio distribution during compression stroke between 300 and 350 CAD where the 2 bar pressure criteria is met. Also, it

was explained previously that the k_{SV} represents the relative strength of quenching with respect to other intramolecular deactivation processes. But we have seen that the slope of the Stern–Volmer plots keep on reducing with increasing temperature suggesting that the oxygen quenching might not be the dominant effect. Furthermore, after 500 K, there was a deviation from non-linearity of SV plots as observed in toluene and anisole. Therefore, molecules with large SV factors are especially desirable for FARLIF application. Thus, one should be cautious in applying FARLIF in the elevated temperature regions of IC engine. Koban et al. [17] concluded that in most practically relevant conditions, the fluorescence signals are in a regime where the oxygen quenching is neither too strong nor negligible. So, to extract fuel–air ratio, prior information on oxygen distribution or temperature distribution is needed. Nonetheless, both FARLIF and in-situ calibration technique have been used to perform several fuel distribution studies. With non-aromatic tracers, fuel concentration is imaged, and with aromatic tracers, fuel–air ratio is directly imaged using FARLIF. Next, we briefly review various important aspects of fuel–air mixture formation in SI engines.

In the presence of liquid droplets especially in gasoline direct injection (GDI) engine, there will be charge cooling effect as the droplets vaporise by absorbing heat from the surrounding charge resulting in a temperature decrement. As already discussed, the recirculated and residual hot exhaust gases can further result in temperature stratification in fired operation. Thus, it becomes important to measure the temperature stratification for correcting the fluorescence signals for quantitative mixture distribution studies. For in-cylinder temperature measurements, there have been studies involving single tracer two-line technique, dual tracers single line technique and single line two colour technique.

Single excitation two tracer temperature imaging

In two tracer technique, a single wavelength is used and the tracers are selected such that they have a different monotonic response of fluorescence emission to temperature increment and the fluorescence spectra of the tracers should be well separated. The ratio of fluorescence from the two compounds are obtained as a monotonic function of temperature. This method was used by Kakuho et al. [148] to determine the in-cylinder temperature distribution in a HCCI engine. They selected 3-pentanone and triethylamine (TEA) to carry out this study and could successfully control HCCI combustion by varying the temperature distribution inside the cylinder. However, this method has some difficulties as it is assumed that the two tracers behave similarly throughout the processes of injection, evaporation and mixture formation so that the effect of variation in tracer quantities at each point can be nullified by taking the ratios [149].

Two-line temperature imaging

In two-line temperature measurements, two different laser wavelengths are used with a single tracer. The tracer and the wavelengths are chosen such that at each wavelength there is a monotonic variation in the fluorescence intensity at a particular pressure. The two lasers are fired in the interval of a few microseconds (typical value: 2 μs [145]) which is much smaller than the time scales of in-cylinder processes. So, a ratio of the two-fluorescence intensity values becomes solely a function of temperature if the pressure is known (pressure at a particular crank angle is constant and is generally measured with a reasonable accuracy using suitable pressure transducers). Two different images each corresponding to a particular wavelength are captured in quick successions. The ratio of the images are then obtained which are solely a function of temperature. The intensity ratios with the help of a suitable calibration at a point with known temperature, can be used to determine the temperature over an entire plane inside the cylinder at a particular crank angle. The same procedure can be repeated for other crank angles as well. Studies based on this was performed by Thurber and Hanson [150] for characterising the temperature of a heated turbulent jet using acetone. Einecke et al. [151] were one of the earliest to extend this method into IC engine domain. They performed the temperature imaging using 10% (vol%) 3-pentanone in iso-octane. They found that the ratio of fluorescence signals from 308 and 248 nm excitation wavelengths with 3-pentanone is most sensitive to temperature variation (see Fig. 34 from ref [149]). This is because the two wavelengths belong to opposite side of the maxima point in absorption spectra of 3-pentanon and acetone (refer part A). A notable phenomenon observed in direct injection (DI) engines is the significant charge cooling effect. Fujikawa et al. [149] used the two-line technique and found that these effects are particularly strong in the stratified charge mode where a large amount of charge cooling is observed especially in the rich region. This required a temperature correction of the raw fluorescence signals. Attar et al. [152] conducted two-line PLIF thermometry to measure in-cylinder charge temperature for assessing charge cooling using 3-pentaone with 277 and 308 nm excitation wavelengths. In their work, during the intake stroke at 250 CAD after top dead centre (ATDC), a stratified fuel–air mixture was detected, resulting in an estimated overall in-cylinder temperature drop of approximately 34 K. The study found that charge cooling increased with higher fuel injection quantities.

Koch et al. [145] and Loffler et al. [153] have used acetone for two-line thermometry with 308 and 248 nm excitation. The authors used acetone due to its volatile nature so that it can be seeded to the intake air. This allowed them to perform negative PLIF or N-PLIF to determine the residual gas fractions after temperature distribution was evaluated

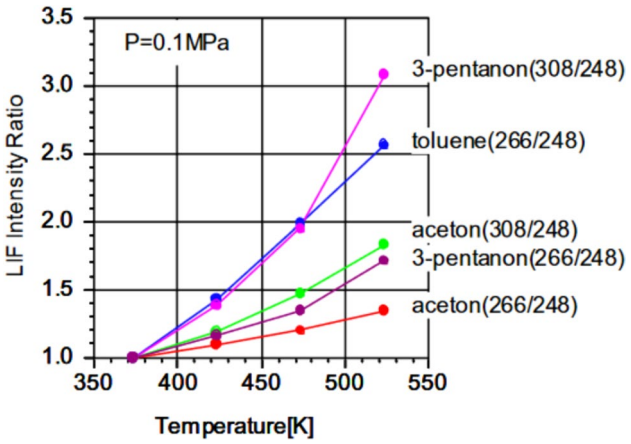

Fig. 34 [149] Fluorescence signal ratios are plotted with temperature at 0.1 MPa. Reprinted from [149] with permission from SAE International

in a tumble plane. Normally, the residual gas fraction and the intake air fraction add up to unity. Thus, the intake air fraction can be determined by acetone PLIF which can then be subtracted from unity to obtain the residual gas fraction. Due to this end subtraction, the technique is called N-PLIF or negative-PLIF. It was found that during the intake stroke there is significant inhomogeneity in the residual gas fraction distribution along with temperature stratification due to the incomplete mixing process. The higher temperature region and the residual gas fraction fields usually overlap on each other as expected. By 50 CAD ATDC of intake stroke [153], the high temperature region was located near the piston crown, and the near cylinder head region had relatively cooler fresh intake charge. This might be due to the incoming fresh charge displacing the residual gases towards the piston as it moves downwards. The inhomogeneity in the temperature field then quickly disappears as the mixing proceeds to provide a homogeneous temperature and residual gas fraction fields during the compression stroke. Temperature measurement also holds significant importance in the context of homogeneous charge compression ignition (HCCI) engines, as temperature variations directly impact controlled autoignition. Rothamer et al. [154] used 3-pentanone and a combination of 277 and 308 nm wavelengths to study the temperature distribution in the swirl plane of a HCCI engine. They also employed N-PLIF method to quantify the distribution of residual hot exhaust gases. Their findings revealed that during the early intake stroke at 24 CAD, a notable amount of exhaust gas residuals were concentrated near the exhaust valves due to inadequate mixing. They also observed an overlap between high-temperature regions and regions with high EGR levels, with EGR temperatures reaching up to 550 K in close proximity to the exhaust valve.

In the studies discussed till now, the two-line thermometry and fuel concentration measurements were not performed simultaneously. Recently, Lind et al. [155] performed simultaneous multi-parameter imaging using a tracer combination of TEA and acetone (1:100 by vol) to perform FARLIF and two-line thermometry (using 308 and 248 nm excitation) respectively. TEA fluorescence signals provided fuel–air ratio information whereas acetone PLIF signal provided air concentration and temperature distribution information. It was found that the fluorescence spectra of acetone and TEA had only a small overlap and thus the signals could be easily separated by a filter. There was no relevant interaction between the two tracers (absorption of TEA fluorescence by acetone). Also, cross-talk by collisional quenching between the two tracers was not detected. A further study was performed by Lind et al. [156] using TEA and 3-pentanone tracer combination both seeded in fuel to perform simultaneous fuel–air ratio and temperature imaging. Single shot images showed evaporative cooling near the fuel spray region as well as temperature stratification near the piston surface due to a strong fuel spray interaction with piston. The authors suggested that such a temperature stratification could lead to a higher CO, unburnt hydrocarbons and soot emissions.

The fluorescence signal of toluene is 90 times stronger at 248 nm excitation and 33 times stronger at 266 nm excitation than acetone at 0.1MPa and 473 K [129]. Fujikawa et al. [149] reported that the high temperature sensitivity of toluene can be exploited to perform temperature measurements using two-line thermometry. However, with increased pressure and temperature, there is a significant decline in toluene fluorescence signal and it becomes comparable to the ketonic counterparts. Normally, ketones have mostly been used for two-line thermometry. The relative insensitivity of ketones to oxygen quenching have made them useful in this regard. However, aromatic molecules like toluene show a temperature induced redshift in fluorescence spectrum which can be utilised to perform temperature imaging using a technique called two-colour temperature imaging.

Two-colour temperature imaging

In two colour technique, a single wavelength and a single tracer is used for temperature determination over a plane. This is performed by the gradual redshift of fluorescence spectrum of the selected tracer with increasing temperature (refer Fig. 35 [43]). In the figure, it can be seen that the fluorescence signal is split into a long (red channel) and a short (blue channel) wavelength part using appropriate filters. The selected tracer must show a broadening of the fluorescence spectrum with temperature. The ratio of the two parts will then depend monotonically on temperature. The single tracer usage removes the difficulty observed in two tracer technique. Furthermore, the ratioing of the fluorescence parts captured by two different cameras also helps to remove the

effects of variations in tracer number densities as well as variations in spatial intensity of laser sheet. Koban et al. [54] studied the temperature sensitivity for toluene by splitting the fluorescence in a region of 280 ± 5 nm region around the spectrum peak and in a long wavelength region greater than 335 nm. A similar 2-colour technique for temperature measurement was also developed using 1-methylnaphthalene as the tracer doped in dodecane as the single quantity fuel surrogate by Kaiser and Long [114]. The temperature induced redshift of 1-Methylnaphthalene fluorescence spectrum was exploited to split the emanating fluorescence into short and a long wavelength image using appropriate dichroic beam splitters and filters. With proper calibration, a spatial temperature distribution was obtained in the region of interest. Once the temperature field was obtained, relevant temperature correction factors were determined to obtain the equivalence ratio distribution in a heated jet flow from the same set of images using FARLIF technique. Zegers et al. [50] also used toluene mixed with air for temperature imaging in an optical diesel engine during fuel injection.

Koban et al. [54] suggested the usage of toluene in two-colour measurement technique owing to the temperature induced redshift in toluene fluorescence spectrum. The measured temperature distribution can be used to correct the equivalence ratio measurement using FARLIF technique. All of these can be obtained using a single laser excitation and two cameras which are much less complex than the two-line thermometry method. However, care must be taken that the total partial pressure of oxygen in surrounding bath gases must be a minimum of 200 mbar [43] since oxygen also introduces a redshift in fluorescence spectrum below 200 mbar. Hence, under such conditions, the oxygen partial pressure in the region of interest has to be determined prior to the application of two-colour technique. To improve SNR for single shot temperature distribution, anisole can be used for 2-colour technique since it has got a larger fluorescence signal than toluene. But it is also known that at lower oxygen partial pressures, the redshift of the fluorescence spectra is dependent on both temperature and oxygen partial pressures (see Fig. 12). Toluene has an advantage over anisole in this regard as the oxygen indued redshift in fluorescence spectrum is only observed at 248 nm and not at 266 nm [54]. A drawback of toluene over anisole in two colour technique is a lower temperature sensitivity as toluene temperature redshift is 2 nm [63] as compared to 2.8 nm for anisole [87]. Due to the low temperature sensitivity, Luong et al. [43] stated that two-line thermometry using 3-pentanone is about three times more sensitive in the temperature range of 368–575 K than the single wavelength scheme based on toluene which has the advantage of less experimental complexity. Luong et al. [43] applied the two-colour technique to IC engines. They used a homogeneous mixture of toluene and air in motoring conditions to perform temperature imaging from 40 to 90 CAD ATDC of intake stroke. The reduction of temperature along the intake stroke could be captured. The authors concluded that the accuracy for single shot temperature measurement was ± 34 K, and for average temperature measurement, it was ± 7 K. Other IC engine studies of two-colour thermometry for in-cylinder temperature determination are discussed in the respective introductory sections of the tracer compounds and are thus not repeated here.

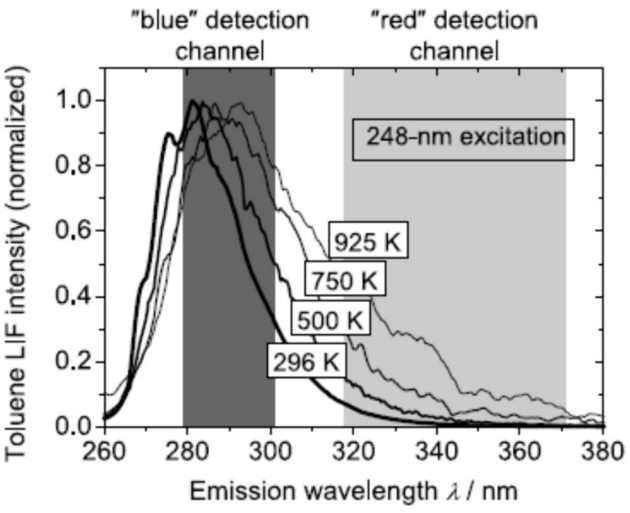

Fig. 35 (from ref [43]) Separation of toluene fluorescence spectrum into two parts- longer wavelength region is referred to as red channel and the lower is referred to as blue channel

In comparison to toluene, the fluorescence signal of 1-methylnaphthalene has a very strong dependence on oxygen partial pressure (Sect. 4.2). The SV factor of di-aromatics like naphthalene and 1-methylnaphthalene at 450 K at 266 nm excitation is 396 and 370 bar^{-1} respectively [105]. On comparison, mono-aromatics like 1,2,4 trimethyl benzene and toluene have SV factors of about 94 bar^{-1} [112] and 88 bar^{-1} [the SV factor of toluene was calculated from the semi-empirical model developed by Koban et al.] [59] for toluene. The value of SV factor provided here is pertaining to the ISC dominated longer lived excited states) respectively at 266 nm and 450 K. Orain et al. suggested that the lifetime of S_1 state in naphthalene is longer (100 ns [106]) than mono-aromatics like 1,2,4-trimethylbenzene (40 ns [157]). This increases the probability of oxygen quenching for naphthalene. The increased oxygen quenching also suggests that naphthalene is more suitable for equivalence ratio measurements in FARLIF technique. The temperature dependence of mono-aromatics was found to be more pronounced. The fluorescence signal intensity was found to have a drop of 1000 times for 1,2,4 trimethylbenzene in the temperature range of 350–900 K [112] as compared to naphthalene which shows a drop of about 10 times in the same temperature range [105]. Faust et al. [35] compares

the normalised FQY dependence with temperature in Fig. 36 for toluene, anisole, naphthalene, acetone and 3-pentanone in a nitrogen bath gas using data from [11, 54, 63, 90, 105].

Even though the Fig. 36 compares the FQY, care must be taken to interpret the behaviour of fluorescence intensity as it also depends on the absorption cross-section behaviour with temperature. However, the absorption cross-section doesn't change to the extent found in FQY (especially at 248 nm). Hence, a large variation in FQY essentially indicates a very high temperature dependence of fluorescence signal intensity and the inclusion of absorption cross-section effect is expected to mildly affect the curves in Fig. 36. It is clearly seen that 3-pentanone is more temperature sensitive compared to acetone as previously discussed in part A. Toluene has a very high temperature dependence followed by anisole than naphthalene. The high temperature sensitivity in mono-aromatics fluorescence intensity make them desirable in terms of two-line thermometry technique. The similar sensitivity of toluene two-line technique with 3-pentanone was observed till 475 K in Fig. 34. Toluene has a temperature induced fluorescence spectrum redshift of about 2 nm per 100 K at 248 nm excitation [54] and 2 nm per 100 K at 266 nm [63] in comparison to naphthalene and 1-methylnaphthalene which have a redshift of about 5 nm per 100 K [63] and 3–4 nm per 100 K [104] at 266 nm excitation respectively. The larger redshift in di-aromatics than toluene provides an opportunity of increased accuracy to the temperature measurement using two-colour technique [104].

Multi component imaging using two tracer technique

It is a common practice for PLIF studies to replace the actual gasoline fuel with a non-fluorescent surrogate in which a tracer compound is whose fluorescence characteristics are well characterised. This is however not a very correct representation of the actual mixing process since gasoline is made up of a number of components with varying volatility. It is expected that the fuel distribution might show some spatial stratification between the high and low volatile components owing to their different vapourization rates. Zhang and Sick ([158] used acetone and p-xylene with iso-octane to represent the low and high volatile fractions. Stevens et al. [159] proposed a new six component surrogate fuel for representing three different volatile groups (two fuel component each) and three tracers, i.e., acetone, toluene and 1,2,4 trimethylbenzene (TMB), representing the three volatile groups. However, since the fluorescence signal intensity of aromatic tracers is much stronger than the ketonic counterparts, there is cross-talk of signals from aromatic tracers in the fluorescence spectral regime of the ketonic tracers [160, 161]. Also, an excited state energy transfer between aromatics and ketones also affect their respective signal intensities [161].

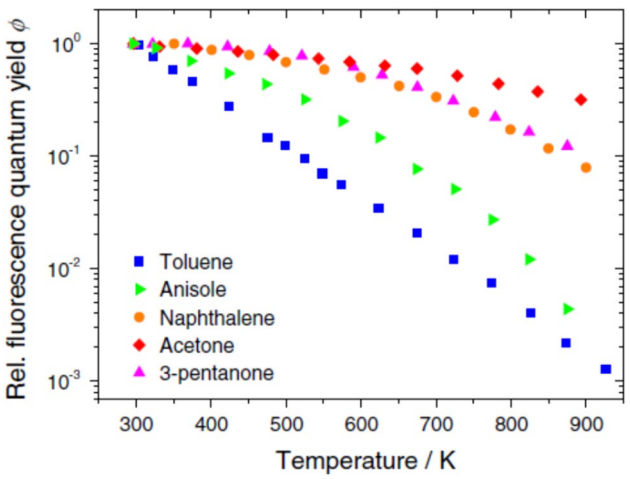

Fig. 36 [35] Normalised FQY values plotted for comparison of various tracers in terms of temperature dependence in a nitrogen bath gas at 1 bar total pressure. Each curve is normalised to the lowest investigated temperatures

Therefore, a new two-tracer technique for multi-component imaging was developed by Bardi et al. [162] using aromatic tracers. They developed a mixture of n-pentane (36% by vol.), iso-octane (46% by vol.) and n-undecane (18% by vol.) to represent low, medium and high volatile fractions respectively such that the three-component surrogate mixture matches with commercial gasoline's distillation curve. Two different aromatic tracers: difluorobenzene (DFB) (0.02 vol%) and 1-methylnaphthalene (0.1 vol%) were added to represent the light to medium and heavy volatile components respectively. The fluorescence spectra of the tracer compounds are quite different which allows their respective signals to be separated with the help of suitable filters and different cameras. A ratio of the captured fluorescence signals of the two tracer compounds is obtained. For complete co-evaporation, the ratio should be same over the entire region of interest. Therefore, any spatial variation of this ratio indicates a variation in the distribution of the different volatile components.

This method was used by Itani et al. [163] used the above mentioned tracer-surrogate mixture to perform LIF studies on mixture formation using a piezo-actuated DI fuel injector inside a high-temperature high-pressure test cell. Such injectors are characterised by the formation of counter-rotating vortex rings with rich-fuel mixture at the periphery of the spray cone due to entrainment of spray and surrounding air. The vortex cores were found to be rich in high-volatile components and the spray centre region was rich in low-volatile components for 550 K. At a higher temperature of above 600 K, the stratification was lower. Cordier et al. [164] extended the technique to a multi-hole DI injector. They also observed preferential evaporation and observed that the spray tail (downstream) was rich in high volatile component and the spray tip (upstream near injector) was rich in low volatile component. This stratification was found

to increase as more ethanol is added (from E00 to E20 and E85) to the surrogate. The stratification was found to reduce with increase in temperature and injection pressure. The authors concluded that an earlier vapourization of the high volatile components led it to be entrained by the surrounding air which brings it to the downstream of the spray plume sooner than the yet to be vapourised low volatile component. Finally, Kranz and Kaiser [25] performed the two tracer technique with a multi-hole injector in an optical engine at stratified operation mode. They found similar segregation of the different boiling fractions and observed that the segregation reduces as the injection timing is delayed from − 68 to − 48 CAD ATDC of compression stroke due to faster evaporation at a higher temperature. As the mixing continues, at later crank angles, the stratification of low and high volatile components reduced.

Scope of future work

Use of tracer based PLIF studies are also receiving increasing attention to perform simultaneous multi-parameter imaging of both temperature and fuel–air ratio distribution to identify inhomogeneities that might have a direct role to play in misfires, auto-ignition, etc. Towards this, a combination of an amine like TEA has been used with acetone [155] and 3-pentanone [156] using two-line thermometry. Nonetheless, multi-parameter imaging studies have also been proposed by using two-colour thermometry of aromatic compounds. Such studies were performed with 1-methylnaphthalene for diesel sprays [104] and with p-xylene [165]. From the studies discussed in this work, it is clear that there are various other aromatic tracer molecules that have found extensive usage in IC engine applications. Some of the popular tracers for which studies on fluorescence characterisation are available are triethylamine [166], p-difluorobenzene [167], p-xylene [168], 1,2,4 trimethylbenzene [112, 169], etc. However, we didn't include them in this review for the sake of conciseness. Due to the ongoing work by several researchers, new tracers with attractive fluorescence properties are coming to attention. One such example is anisole, which has recently found usage and is covered in this work. It is found to emit strong fluorescence signals [63] which is expected to improve the signal-to-noise ratio. Therefore, the search for new tracers with conducive fluorescence properties should continue. Tracers with a high intensity of fluorescence and a large Stokes shift will definitely improve the quality of the experimental results.

A major shortcoming of PLIF studies is the very limited temporal resolution which is either due to limitations of laser or image acquisition systems. Lately, much focus is being put for obtaining images in quick successions to obtain multiple images in the same cycle. Double pulse PLIF setups with multiple laser heads was developed [170–172]. In some works, sequential images have also been obtained [135, 173–175]. Furthermore, continuous wave laser systems coupled with a high FQY tracer like toluene was used to obtain images in turbulent gaseous systems [176]. These will enhance temporal resolution and allow to track the relevant parameters of interest in a particular cycle, further improve our understanding. Bohm et al. [177] have reviewed the feasibility and potential of laser diagnostics at high temporal resolution as well as the possibilities and limitations of the modern laser and camera systems. However, there are certain difficulties with high speed (kHz) measurement. For high speed PLIF at 12 kHz, Fajardo et al. ([178] and Peterson and Sick [179] utilized DPSS Nd-YAG lasers operating at 355 nm with 0.5 mJ pulse energy. Such low pulse energy requires the use of high speed intensifiers which may lead to scalar gradient blurring, spatial resolution degradation, and potential introduction of additional noise [180, 181]. Gordon et al. [180] advised against the use of high-speed intensifiers whenever possible. Newer pulse burst system lasers have been developed that are able to provide much higher energy per pulse at kHz rates (15 mJ/pulse at 266 nm at 10 kHz for acetone PLIF by Miller et al. [182], 145 mJ/pulse at 266 nm at 10 kHz by Papageorge and Sutton [183]). But with this, there are issues of photolysis of tracers [183] and change of boundary layer flow properties by surface heating [164] [184]. Therefore, the assumption of 'non-intrusiveness' may not hold for high-energy, high-repetition-rate laser measurement systems, warranting further investigation in this area.

Due to the potential for emission reduction and enhanced efficiency, GDI engines are also receiving increased attention for their application in small-bore engine segments (currently mostly operated on PFI mode) which hold a significant market share especially in the developing world [185, 186]. However, there are significant challenges to the adoption of DI technology in small-bore segments especially due to an increased fuel impingement (that might deteriorate emissions) owing to the small size of combustion chamber. Methods to study impingement and its quantification in an optical engine were developed [187] and can be extended to small-bore optical engines. Furthermore, fuel jet penetration can be restricted using multiple injections (as much as three injections) and used to limit impingement in small-bore GDI engines [188]. Increasing the number of injections per cycle [189–191] is being actively pursued which has also brought the focus on developing a fast-acting multi-hole solenoid or multi-hole piezo injector. Additionally, multi-dimensional CFD studies over the entire engine cylinder region have also been extensively used to study various in-cylinder processes. The experimental data obtained from the laser-based in-situ techniques at a particular operating condition can be used to validate the CFD models for flow studies [192], mixture distribution studies [82, 193] which can later be extended to various operating conditions greatly augmenting the process of engine optimisation. Such a combination of experiments and simulations can also be helpful to validate newer CFD

models for mixture distribution using large eddy simulation (LES) [142] that is capable enough to characterise CCV and is becoming popular in both industry and academia for the study of combustion variability in lean burn engines.

Lately, newer combustion concepts like low temperature combustion (LTC) have emerged which have the potential to increase efficiency and reduce engine out emissions. Among them, HCCI engines have received a lot of attention and were found to have a critical dependence of combustion stability on temperature stratification. Therefore, further studies to extend their stable operating regime will require non-intrusive PLIF based studies for temperature imaging. Also, gasoline partially premixed combustion (PPC) concepts in LTC combustion have newly emerged [194]. In order to understand the auto-ignition processes, high speed PLIF studies will be very important [195]. Since formaldehyde is formed as a result of LTC in auto-ignition [195], high-speed PLIF of formaldehyde might receive increased attention. The difficulties of performing high-speed measurements with high repetition rates lasers have already been discussed in this work. The issue of low pulse energy at high kHz frequency can be tackled with advanced pulse-burst laser systems. High pulse energies at kHz frequencies have potential ramifications on the 'non-intrusive' assumption of PLIF based measuring techniques. Also, due to the size and complexity of pulse-burst systems, high-speed PLIF measurements using them become quite capital intensive and are therefore restricted to a handful of dedicated optical laboratories.

In aerospace industry too, alternative fuels are receiving increased attention due to their lower costs and a potential to mitigate climate change [196]. Since aromatic compounds are the constituents of both the conventional (alkylnaphthalenes in jet-A [197]) as well as alternative fuels (like 1,2,4 trimethylbenzene in C5 alternative jet fuel [197]), recently PLIF studies were performed to evaluate their spray characteristics [198]. Fluorescence characteristics of 1,2,4 trimethylbenzene were studied by Orain et al. [112] and Benzler et al. [169]. While the diagnostic techniques discussed here find their primary application in internal combustion (IC) engines, they hold potential for extension to other combustion systems like for the jet fuels in gas turbines and in other fundamental research endeavours. Advancements in laser and image acquisition systems promise enhanced experiment accuracy and deeper insights into the studied processes. Consequently, the ongoing enhancement of PLIF diagnostic methods and the exploration of the underlying photophysics of fluorescence from existing tracers will remain a dynamic and vibrant area of research.

7 Conclusion

This paper offers a comprehensive overview of fluorescent tracer compounds that play a crucial role in non-intrusive diagnostics for IC engines using PLIF. Numerous studies by various researchers have significantly advanced our understanding of how these compounds behave under the extreme conditions of temperature and pressure typically encountered during the compression stroke of an IC engine. Currently, there is a wide array of organic compounds available as potential tracers, with a substantial body of literature detailing their fluorescence characteristics. Therefore, it is essential to provide a comprehensive review of the fluorescence characteristics of these tracer molecules, as this knowledge is fundamental in the development of new diagnostic techniques. This work specifically focuses on tracers utilized in IC engines over the years, with an emphasis on organic tracers. The review categorizes these tracers into carbonyl and aromatic compounds. Part A of this work centres on carbonyl compounds, while the current article (Part B) concentrates on aromatic compounds. This division is primarily due to the varying susceptibility of carbonyl and aromatic compounds to oxygen quenching. Within the aromatic compounds category, three subgroups are identified: mono-aromatics, di-aromatics, and poly-aromatics. Toluene and anisole are selected to represent the mono-aromatic group. Similarly, naphthalene and 1-methylnaphthalene are chosen to represent di-aromatics, while fluoranthene is chosen to represent the poly-aromatic group. Table 2 provides a summary of the photophysical properties of toluene, anisole, naphthalene, 1-methylnaphthalene and fluoranthene.

To comprehend the intensity of the fluorescence signal, the basic approach involves breaking it down into absorption cross-section and FQY, and then examining their individual variations. The absorption cross-section is influenced by the excitation wavelength and temperature, making it relatively straightforward to quantify its changes. On the other hand, FQY is contingent on the excitation wavelength, temperature, pressure, and the composition of the bath gas mixture, rendering it more complex to quantify and model. The study yielded the following insights into the fluorescence characteristics of the discussed molecules-

- The absorption cross-section values of aromatic molecules (see Table 2) are orders of magnitude higher than ketones (around 10^{-19} cm^2 under ambient conditions: refer part A). Also, the FQY values are several orders of magnitude higher than ketones (ex: 0.0011 for 3-pentanone [202], refer part A). This results in much larger fluorescence signal for aromatic compounds than their ketonic counterparts. This not only increases the signal-to-noise ratio but also enables their doping in minimal

quantities as compared to ketones (ex: 25% by vol. for 3-pentanone [132, 203], refer part A). Such low doping quantities result in a minimal change in the physical and chemical properties of the surrogate/fuel necessary for evaluating engine performance in firing tests. Another major difference in the aromatic and ketonic tracer compounds is the large susceptibility of aromatic tracers towards oxygen quenching. This is due to the large energy gap between the excited state and ground state of aromatic molecules that provide sufficient energy to the oxygen molecule for its transition from ground triplet state to an excited singlet state.

- Typically, as temperature increases, the absorption spectrum widens towards longer wavelengths. This phenomenon holds true for all the ketonic and aromatic tracers discussed in parts A and B. Normally, the absorption spectra are observed to grow stronger with increasing temperature for all the aromatic molecules discussed here except for anisole. Strangely, for anisole, a decrease in the absorption cross-section is observed with an increase in temperature. The reason behind this behaviour for anisole is not yet clear. For all other tracer compounds discussed in this work, depending on the molecule and the excitation wavelength, the absorption cross-section at a particular wavelength might increase, remain constant or show a non-monotonic behaviour. Sometimes, the absorption spectra for excitations concerning different energy levels (example as S_0 to S_1 and S_0 to S_2) may overlap at high temperatures. This will bring about temperature dependency to wavelengths which show temperature insensitivity at lower temperatures.
- Apart from absorption spectra, fluorescence spectra also show some changes with temperature. Typically, fluorescence spectra exhibit a structured pattern for aromatic molecules. However, with increasing temperature, the peaks broaden and blend together, leading to a loss of distinct structure. Unlike ketones, which show no redshift, aromatic molecules show a redshift in their fluorescence spectra with temperature. This temperature induced redshift was later used to develop a two-colour temperature imaging technique. The redshift values were found to be higher for the di-aromatics as compared to the mono-aromatics (refer Table 2). The spectra also show a redshift with an increase in oxygen content. The discernible structures in fluorescence spectrum observed in an environment without quenching agents tend to fade with higher oxygen partial pressures. This type of redshift due to oxygen presence was also not observed for ketones.
- For all the tracers discussed in parts A and B, the FQY values are found to reduce with temperature as non-radiative rates increase with the vibrational energy level in the excited state molecule. The reduction with temperature is normally sharper than ketones due the onset of internal conversion. However, the behaviour of the molecules with pressure increase is found to be different for ketones and aromatic molecules. In ketones, where the FQY is found to increase with pressure, in aromatics, the

Table 2 Photophysical properties of toluene, anisole, naphthalene, 1-methylnaphthalene and fluoranthene

Photophysical properties	Toluene	Anisole	Naphthalene	1-methylnaphthalene	Fluoranthene
Absorption spectrum (nm)	225–275 [199]	240–310 [87]	200–320 [108]	230–330 @350 K [109]	200–400 [200]
Absorption cross-section at 266 nm (in cm^2)	1.9×10^{-19} [54]	3.35×10^{-18} [87]	1.4×10^{-17} [107]	2.45×10^{-17} @ 450 K [109]	~5×10^{-17} @ 473 K [119]
Fluorescence spectrum range (nm)	260–340 [59]	270–360 [80]	307–378 @ 673 K [19]	300–400 @ 398 K [20]	401–557 @ 673 K [19]
Fluorescence spectrum (peak) (nm)	280 [54]	290 [80]	323, 336 @ 673 K [19]	328, 338 @ 398 K [20]	454 @ 673 K [19]
Absolute FQY (at NTP in non-oxygen environment)	0.22 [25]	0.36 [89]	0.42 [89]	0.4 [89]	–
K_sv at 266 nm (at 450 K in bar^{-1})	88 [59]	–	396 [105]	370 [105]	–
Temperature induced redshift (nm/100 K)	2 [63]	2.8 [87]	5 [104]	3–4 [63]	4 [19]
Typical doping amounts	5% [40, 41], 3% [42] (by vol) in iso-octane	2% [81], 2.5% (by vol.) [85, 86] with iso-octane	5 wt % in gasoline [98]	1 vol % in iso-octane [201],	~1% by mass [26]

All values are at room temperature unless specified otherwise

FQY might decrease or increase with increasing pressure depending on the laser excitation and temperature. This is due to the fact that the energy gap between electronic states is larger in aromatics as compared to ketones. Increase in FQY with pressure applies effectively to molecules where the excitation energy is sufficient to elevate the molecule to a vibrational level significantly above the thermalised level within the same singlet state. This is typically the case for ketonic compounds, where the transition involves a shift from $\mathbf{n} \rightarrow \boldsymbol{\pi}^*$ orbitals. However, the scenario may differ for aromatic molecules, as they undergo a $\boldsymbol{\pi} \rightarrow \boldsymbol{\pi}^*$ transition. Since a n orbital is energetically higher than a pi orbital, the energy gap for $\boldsymbol{\pi} \rightarrow \boldsymbol{\pi}^*$ transition is larger. Consequently, the wavelength required to effectively excite a ketonic molecule well above the thermalised level in the excited singlet state (e.g., 266 nm in 3-pentanone) may only be sufficient to just reach the thermalised levels in an aromatic molecule (e.g., 266 nm in toluene). Therefore, for longer wavelengths, the energy is not sufficient for transition to the thermalised levels and under such conditions, a reduction should be found in FQY values with increasing pressures.

- At extremely low pressures (around 10 mbar), collisions are infrequent, and fluorescence arises from a vibrational level determined by the interplay of temperature and excitation wavelength. This low FQYvalue represents the limit under low-pressure conditions. As pressure increases, collisions become more frequent, causing the FQY value to deviate from the low-pressure limit. It subsequently rises or falls with pressure and eventually reaches a high-pressure limit. This is a result of the molecule relaxing to the thermalised level of the excited electronic state. The high-pressure limit is solely influenced by temperature, while the low-pressure limit is determined by both temperature and excitation wavelength. Nevertheless, both limits are unaffected by the composition of the surrounding gas. The more the number of atoms in the collider molecule, the better is the relaxation. However, if the surrounding gas contains molecules that exhibit quenching behaviour, such as oxygen, then as pressure rises, FQY values decrease due to increased collisions and greater deactivation of the excited molecule. This behaviour is similar to ketones.

After a thorough exposition of fluorescence characteristics of various tracers, popular techniques used for thermometry and fuel distribution imaging were discussed briefly in Sect. 6. Based on the fluorescence characteristics of molecules, different diagnostic techniques have been proposed for imaging both temperature and fuel distribution. Multi-component fuel distributions have also been imaged by using multiple tracers used to represent a particular boiling fraction. It was found that each tracer has certain set of advantages and limitations concerning with usage in a particular diagnostic technique. Hence, the combination of tracer and excitation wavelength selected should be such that the fluorescence behaviour obtained is tailor suited for the type of experimental technique selected, the fuel surrogate being used, the allowed complexity depending on the constraints of cost and available equipment limitations as well as the desired accuracy. Using the diagnostic techniques, various studies were discussed mostly relating to PFI and GDI engines. A good amount of attention was provided on discussions pertaining to impact of flow-field, injection timing, pressures and multiple injections on mixture formation as well as their CCV. Evolution of in-cylinder temperature distribution right from the gas exchange process to the compression stroke was also discussed.

The step-ladder photophysical model for toluene, anisole and naphthalene are more or less developed. However, such a model for 1-methylnaphthalene is yet to be seen in the literature. There is a dearth of studies for combined high pressure and temperature regimes of both naphthalene and 1-methylnaphthalene. Also, there is a lack of parametric studies of fluorescence for the case of 1-methylnaphthalene. Further studies in these topics could provide the much-needed information that can be used to develop accurate step ladder models for the di-aromatics. Nonetheless, it should be noted that this tracer is already in a supercritical state from thermodynamic point of view at typical diesel engine injection conditions. Then the calibration is usually done in rapid compression machines as in [109]. Similarly, more studies have to be performed for fluoranthene fluorescence as till now only the work of Kuhni et al. [119] is available as a parametric study of fluorescence dependence. More data is needed to develop a robust photophysical model for the same.

Acknowledgements The authors would like to acknowledge several researchers working in the field of tracer based LIF and their fluorescence characterisation. Their relentless efforts over the years have led to a significant improvement in the understanding of photophysics behind fluorescent tracer molecules.

Author contributions S.N wrote the main manuscript text and M.M reviewed the manuscript

Data availability The datasets generated during and/or analysed during the current study are available from the corresponding author on reasonable request.

Declarations

Competing interests The authors declare no competing interests.

References

1. C. Schulz, V. Sick, Prog. Energy Combust. Sci. **31**, 75 (2005)
2. F. W. Bowditch, SAE Technical Paper 610002 (1961)
3. R. M. Richman and W. C. Reynolds, SAE Technical Paper 840379 (1984)
4. S. C. Bates, SAE Technical Paper 880520 (1988)
5. M. Mittal and P. Mehta, SAE Technical Paper 2018-01-1775 (2018)
6. V.G. McDonell, G.S. Samuelsen, Meas. Sci. Technol. **11**, 870 (2000)
7. S. T. Seitz, Thermal Boundary Layer Measurements Using Planar Laser Induced Fluorescence, 2018
8. R. Bazile, D. Stepowski, Exp. Fluids **20**, 1 (1995)
9. K. Kohse-Höinghaus, Prog. Energy Combust. Sci. **20**, 203 (1994)
10. B.H. Failor, S. Chantrenne, P.L. Coleman, J.S. Levine, Y. Song, H.M. Sze, Rev. Sci. Instrum. **74**, 1070 (2003)
11. J.D. Koch, R.K. Hanson, Appl. Phys. B **76**, 319 (2003)
12. K. Rohatgi, Fundamentals of Photochemistry (New Age International, New Delhi, India, 2014)
13. B. Valeur, M.N. Berberan-Santos, *Molecular fluorescence*, 2nd edn. (Wiley-VCH Verlag, Weinheim, Germany, 2013)
14. M. Klessinger, J. Michl, *Excited states and photochemistry of organic molecules* (Wiley-VCH Verlag, Weinheim, Germany, 1995)
15. J. Scholz, T. Wiersbinski, and V. Beushausen, SAE technical paper 2007-01-0645 (2007)
16. J. Reboux, D. Puechberty, F. Dionnet, SAE Technical Paper **94**, 1994 (1988)
17. W. Koban, J.D. Koch, R.K. Hanson, C. Schulz, Appl. Phys. B **80**, 147 (2005)
18. K.H. Tran, C. Morin, M. Kühni, P. Guibert, Appl. Phys. B **115**, 461 (2014)
19. Y. Zhang, L. Wang, P. Liu, Y. Li, R. Zhan, Z. Huang, and H. Lin, Appl. Phys. B **125**, 5 (2019)
20. U. Retzer, W. Fink, T. Will, S. Will, and L. Zigan, Appl. Phys. B **125**, 124 (2019)
21. S. Budavari, Drugs and biologicals (1989)
22. M. J. O'neil, The Merck index-an encyclopedia of chemicals, drugs, and biologicals (Royal Society of Chemistry, Cambridge, UK, 2013)
23. W.M. Haynes, *CRC handbook of chemistry and physics* (CRC Press LLC, Boca Raton, 2014), pp.3–272
24. J. P. Styron, P. L. Kelly-Zion, C. F. Lee, J. E. Peters, R. A. White, and R. P. Lucht, 2000-01-0243 (2000)
25. P. Kranz, S.A. Kaiser, Proc. Combust. Inst. **37**, 1365 (2019)
26. J. Meyer, M. Haug, M. Schreiber, and S. Unverzagt, SAE technical paper 950107 (1995)
27. D. R. Lide, CRC handbook of chemistry and physics, 85th Edition (CRC Press, 2004)
28. J. A. Riddick, W. B. Bunger, and T. K. Sakano, Techniques of chemistry 4th edn., Volume II. Organic solvents (John Wiley and Sons, New York, NY, 1985)
29. H. Zhao, P. Unhannanant, W. Hanshaw, J.S. Chickos, J. Chem. Eng. Data **53**, 1545 (2008)
30. J.J.H. Haftka, J.R. Parsons, H.A.J. Govers, J. Chromatogr. A **1135**, 91 (2006)
31. M.A.V. Ribeiro da Silva, J.R.B. Gomes, A.I.M.C.L. Ferreira, J. Phys. Chem. B **109**, 13356 (2005)
32. U. S. Coast Guard, Department of Transportation. CHRIS-hazardous chemical data (U.S. Government Printing Office, Washington, D.C., n.d.), pp. 1984–1985
33. M. Balcan, S. Arzik, T. Altunata, Thermochim. Acta **278**, 49 (1996)
34. W.-K. Wong, E.F. Westrum, J. Chem. Thermodyn. **3**, 105 (1971)
35. S. Faust, M. Goschütz, S.A. Kaiser, T. Dreier, C. Schulz, Appl. Phys. B **117**, 183 (2014)
36. A.B. Macknick, J.M. Prausnitz, J. Chem. Eng. Data **24**, 175 (1979)
37. W.-Y. Shiu, D. Mackay, J. Chem. Eng. Data **42**, 27 (1997)
38. S. V. Vulimiri, M. M. Pratt, S. Kulkarni, S. Beedanagari, and B. Mahadevan, in Reproductive and developmental toxicology (Elsevier, 2017), pp. 379–396
39. IARC Working Group on the Evaluation of Carcinogenic Risks to Humans, DIESEL FUELS (International Agency for Research on Cancer, 1989)
40. J. Reboux, D. Puechberty, and F. Dionnet, SAE technical paper 961205 (1996)
41. J. C. Sacadura, L. Robin, F. Dionnet, D. Gervais, P. Gastaldi, and A. Ahmed, SAE technical paper 2000-01-1794 (2000)
42. D. Frieden, V. Sick, J. Gronki, C. Schulz, Appl. Phys. B **75**, 137 (2002)
43. M. Luong, R. Zhang, C. Schulz, V. Sick, Appl. Phys. B **91**, 669 (2008)
44. C. Willman, R. Stone, M. Davy, B. A. O. Williams, P. Ewart, L. Shen, D. L. S. Hung, M. Liu, and J. Camm, SAE technical paper 2019-01-0722 (2019)
45. C. Gessenhardt, C. Schulz, S.A. Kaiser, Proc. Combust. Inst. **35**, 3697 (2015)
46. B. Peterson, E. Baum, B. Böhm, V. Sick, A. Dreizler, Proc. Combust. Inst. **34**, 3653 (2013)
47. C.L. Genzale, R.D. Reitz, M.P.B. Musculus, Proc. Combust. Inst. **32**, 2767 (2009)
48. D. Sahoo, B. R. Petersen, and P. C. Miles, in ASME 2012 Internal combustion engine division spring technical Conference (American Society of Mechanical Engineers, 2012)
49. G. Nyrenstedt, Q. Tang, R. Sampath, A. AlRamadan, M. Ben Houidi, E. Cenker, G. Magnotti, and B. Johansson, Fuel (Lond.) 295, 120638 (2021)
50. R.P.C. Zegers, M. Yu, C. Bekdemir, N.J. Dam, C.C.M. Luijten, L.P.H. de Goey, Appl. Phys. B **112**, 7 (2013)
51. B. Petersen, P.C. Miles, D. Sahoo, S.A.E. Int, J. Engine **5**, 526 (2012)
52. M. P. B. Musculus, T. Lachaux, L. M. Pickett, and C. A. Idicheria, (2007)
53. A. Gilbert, J.E. Baggott, *Essentials of molecular photochemistry* (Blackwell Science, Philadelphia, PA, 1990)
54. W. Koban, J.D. Koch, R.K. Hanson, C. Schulz, Phys. Chem. Chem. Phys. **6**, 2940 (2004)
55. H. Hippler, J. Troe, and H. J. Wendelken, J. Chem. Phys. (1983)
56. C. S. Burton and W. A. Noyes Jr, J. Chem. Phys. (1968)
57. W. B. Richardson, S. H. Lin, and D. L. Evans, J. Chem Soc. Faraday Trans. 2. **78**, 1 (1982)
58. N. Wermuth and V. Sick, SAE technical paper 2005–01–2090 (2005).
59. W. Koban, J.D. Koch, R.K. Hanson, C. Schulz, Appl. Phys. B **80**, 777 (2005)
60. B. H. Cheung, R. Hanson, C. F. Edwards, M. G. Mungal, and Stanford University. Department of Mechanical Engineering, *Tracer-based planar laser-induced fluorescence diagnostics: quantitative photophysics and time-resolved imaging* (Stanford University, 2011)
61. J. Yoo, D. Mitchell, D.F. Davidson, R.K. Hanson, Exp. Fluids **49**, 751 (2010)
62. R. Devillers, G. Bruneaux, C. Schulz, Appl. Phys. B **96**, 735 (2009)
63. S. Faust, G. Tea, T. Dreier, C. Schulz, Appl. Phys. B **110**, 81 (2013)
64. B. Rossow, Institut Des Sciences Moléculaires d'Orsay, Université (2011).

65. H. Frerichs, T. Lenzer, K. Luther, D. Schwarzer, Phys. Chem. Chem. Phys. **7**, 620 (2005)
66. P. Farmanara, V. Stert, W. Radloff, I.V. Hertel, J. Phys. Chem. A **105**, 5613 (2001)
67. M. Jacon, C. Lardeux, R. Lopez-Delgado, A. Tramer, Chem. Phys. **24**, 145 (1977)
68. S. F. Fischer, A. L. Stanford, and E. C. Lim, J. Chem. Phys. (1974)
69. M.G. Prais, D.F. Heller, K.F. Freed, Chem. Phys. **6**, 331 (1974)
70. R.E. Smalley, Annu. Rev. Phys. Chem. **34**, 129 (1983)
71. M.C. Thurber, F. Grisch, R.K. Hanson, Opt. Lett. **22**, 251 (1997)
72. J. Koch and R. Hanson, in 41st Aerospace sciences meeting and exhibit (American Institute of Aeronautics and Astronautics, Reston, Virigina, 2003)
73. T. Benzler, S. Faust, T. Dreier, C. Schulz, Appl. Phys. B **121**, 549 (2015)
74. Q. Wang, K. H. Tran, C. Morin, J. Bonnety, G. Legros, and P. Guibert, Appl. Phys. B **123**, 199 (2017)
75. H. Hippler, J. Troe, H.J. Wendelken, J. Chem. Phys. **78**, 6709 (1983)
76. M.C. Thurber, R.K. Hanson, Appl. Phys. B **69**, 229 (1999)
77. B.H. Cheung, R.K. Hanson, Appl. Phys. B **106**, 755 (2012)
78. P. Guibert, V. Modica, C. Morin, Exp. Fluids **40**, 245 (2006)
79. T. Hirasawa, T. Kaneba, Y. Kamata, K. Muraoka, Y. Nakamura, J. Vis. (Tokyo) **10**, 197 (2007)
80. S. Faust, T. Dreier, C. Schulz, Appl. Phys. B **112**, 203 (2013)
81. J. Laichter, S.A. Kaiser, Appl. Sci. Res. **110**, 171 (2023)
82. P. Kranz, D. Fuhrmann, M. Goschütz, S. Kaiser, S. Bauke, K. Golibrzuch, H. Wackerbarth, P. Kawelke, J. Luciani, L. Beckmann, J. Zachow, M. Schuette, O. Thiele, and T. Berg, SAE technical paper 2018-01-0633 (2018)
83. S. Nayek and M. Mittal, J. Eng. Gas Turbine. Power **145**, 070801 (2023)
84. S. Hokimoto, T. Kuboyama, Y. Moriyoshi, M. Iida, and T. Watanabe, SAE technical paper 2017-01-2213 (2013)
85. K.H. Tran, P. Guibert, C. Morin, J. Bonnety, S. Pounkin, G. Legros, Combust. Flame **162**, 3960 (2015)
86. M.A. Shahbaz, S. Jahangir, S.A. Kaiser, Exp. Fluids **64**, 196 (2023)
87. S. Zabeti, M. Aghsaee, M. Fikri, O. Welz, C. Schulz, Proc. Combust. Inst. **36**, 4525 (2017)
88. L.J.H. Hoffmann, S. Marquardt, A.S. Gemechu, H. Baumgärtel, Phys. Chem. Chem. Phys. **8**, 2360 (2006)
89. N. Nijegorodov, R. Mabbs, D.P. Winkoun, Spectrochim. Acta A **59**, 595 (2003)
90. M.C. Thurber, F. Grisch, B.J. Kirby, M. Votsmeier, R.K. Hanson, Appl. Opt. **37**, 4963 (1998)
91. J. Hartwig, G. Mittal, K. Kumar, C.-J. Sung, Appl. Phys. B **123**, 191 (2017)
92. J. Hartwig, M. Raju, C.-J. Sung, Appl. Phys. B **123**, 193 (2017)
93. T. Baranowski, T. Dreier, C. Schulz, T. Endres, Phys. Chem. Chem. Phys. **21**, 14562 (2019)
94. P. Baranger, M. Orain, and F. Grisch, in 43rd AIAA Aerospace sciences meeting and exhibit (American Institute of Aeronautics and Astronautics, Reston, Virigina, 2005)
95. L.C. Marr, T.W. Kirchstetter, R.A. Harley, A.H. Miguel, S.V. Hering, S.K. Hammond, Environ. Sci. Technol. **33**, 3091 (1999)
96. T. Ni, L.A. Melton, Appl. Spectrosc. **50**, 1112 (1996)
97. S. Kaiser, D.C. Kyritsis, P. Dobrowolski, M.B. Long, A. Gomez, J. Mass Spectrom. Soc. Jpn. **51**, 42 (2003)
98. R. Shimizu, S. Matumoto, S. Furuno, M. Murayama, and S. Kojima, SAE technical paper 922356 (1992)
99. J. Trost, L. Zigan, A. Leipertz, D. Sahoo, P.C. Miles, Int. J. Engine Res. **15**, 741 (2014)
100. J.-P. Leininger, F. Lorant, C. Minot, F. Behar, Energy Fuels **20**, 2518 (2006)
101. J. Trost, L. Zigan, A. Leipertz, D. Sahoo, P.C. Miles, Appl. Opt. **52**, 8001 (2013)
102. L. Melton, J. Verdiect, *Twentieth symposium (International) on combustion* (The Combustion Institute, Pittburgh, 1984), pp.1283–1290
103. F. Payri, J.V. Pastor, J.M. Pastor, J.E. Juliá, Int. J. Engine Res. **7**, 77 (2006)
104. S. Lind, U. Retzer, S. Will, L. Zigan, Proc. Combust. Inst. **36**, 4497 (2017)
105. M. Orain, P. Baranger, B. Rossow, F. Grisch, Appl. Phys. B **102**, 163 (2011)
106. F. M. Behlen, D. B. McDonald, and V. Sethuraman, J. Chem. (1981)
107. M. Suto, X. Wang, J. Shan, L.C. Lee, J. Quant. Spectrosc. Radiat. Transf. **48**, 79 (1992)
108. H. Grosch, Z. Sárossy, H. Egsgaard, A. Fateev, J. Quant. Spectrosc. Radiat. Transf. **156**, 17 (2015)
109. U. Retzer, H. Ulrich, F. J. Bauer, S. Will, and L. Zigan, Appl. Phys. B **126**, 50 (2020)
110. J.B. Birks, *Photophysics of Aromatic Molecules* (Wiley- Interscience, New York, 1970)
111. F. Ossler, T. Metz, M. Aldén, Appl. Phys. B **72**, 465 (2001)
112. M. Orain, P. Baranger, B. Rossow, F. Grisch, Appl. Phys. B **100**, 945 (2010)
113. J.O. Uy, E.C. Lim, Chem. Phys. Lett. **7**, 306 (1970)
114. S.A. Kaiser, M.B. Long, Proc. Combust. Inst. **30**, 1555 (2005)
115. J. C. Hsieh, C. S. Huang, and E. C. Lim, J. Chem. Phys. (1974)
116. L.M. Hall, T.F. Hunter, M.G. Stock, Chem. Phys. Lett. **44**, 145 (1976)
117. G.S. Beddard, S.J. Formosinho, G. Porter, Chem. Phys. Lett. **22**, 235 (1973)
118. I.B. Berlman, *Handbook of fluorescence spectra of aromatic molecules*, 2nd edn. (Academic Press, San Diego, CA, 1971)
119. M. Kühni, C. Morin, P. Guibert, Appl. Phys. B **102**, 659 (2011)
120. T.Q. Ni, L.A. Melton, Appl. Spectrosc. **47**, 773 (1993)
121. A.A. Ruth, M.T. Wick, Chem. Phys. Lett. **266**, 206 (1997)
122. J. Kolc, E.W. Thulstrup, J. Michl, J. Am. Chem. Soc. **96**, 7188 (1974)
123. L. Sassu, L. Perezzani, W.A. Ivancic, R.H. Barnes, B.W. Wabuyele, Appl. Spectrosc. **55**, 307 (2001)
124. D.L. Philen, R.M. Hedges, Chem. Phys. Lett. **43**, 358 (1976)
125. K.M. Bark, R.K. Force, J. Phys. Chem. **93**, 7985 (1989)
126. K.-M. Bark, R.K. Forcé, Spectrochim. Acta A **49**, 1605 (1993)
127. R. Pradheep, M. Mittal, P. S. Mehta, V. Balaji, and Others, in 18th Annual Conference on liquid atomization and spray systems (ILASS-Asia 2016) (2016)
128. F. Medaerts and D. Puechberty, SAE technical paper 982524 (1998)
129. T. Fujikawa, Y. Hattori, and K. Akihama, SAE technical paper 972944 (1997)
130. C. Weaver, S. Wooldridge, S. Johnson, V. Sick, and G. Lavoie, SAE technical paper 2003-01-3236 (2003).
131. B. Johansson, H. Neij, M. Aiden, and G. Juhlin, SAE technical paper 950108 (1995)
132. M. Berckmüller, N. P. Tait, and D. A. Greenhalgh, SAE technical paper 970826 (1997)
133. S. Garg, M. Mittal, S. Sahu, and V. Lakshminarasimhan, SAE technical paper 2020-01-0786 (2020)
134. S. Haramiishi, T. Watanabe, M. Iida, and S. Hokimoto, SAE technical paper 2019-32-0552 (2019)
135. J.D. Smith, V. Sick, Appl. Phys. B **81**, 579 (2005)
136. J.D. Smith, V. Sick, Proc. Combust. Inst. **31**, 747 (2007)
137. J. D. Smith and V. Sick, SAE technical paper 2006-01-1264 (2006)
138. B. Peterson, D.L. Reuss, V. Sick, Combust. Flame **161**, 240 (2014)

139. K. Hiraya, I. Hotta, E. Takahashi, H. Tsuchida, and T. Urushihara, SAE technical paper 2004-01-2944 (2004)
140. N. Kampanis, C. Arcoumanis, S. Kometani, R. Kato, H. Kinoshita, Int. J. Engine Res. **7**, 143 (2006)
141. J. Yang, M. Xu, D.L.S. Hung, Q. Wu, X. Dong, Energy Convers. Manag. **138**, 565 (2017)
142. M. Ritter, L.-M. Malbec, and O. Laget, SAE Int. J. Adv. Curr. Prac. Mobil. 3, 95 (2020)
143. V.M. Salazar, S.A. Kaiser, S.A.E. Int, J. Engines **2**, 119 (2009)
144. T. Mederer, M. Wensing, and A. Leipertz, SAE technical paper 2013-01-0558 (2013)
145. P. Koch, M.G. Löffler, M. Wensing, A. Leipertz, Int. J. Engine Res. **11**, 455 (2010)
146. M. Storch, S. Lind, S. Will, L. Zigan, Appl. Opt. **55**, 8532 (2016)
147. M. Storch, F. Hinrichsen, M. Wensing, S. Will, L. Zigan, Appl. Energy **156**, 783 (2015)
148. A. Kakuho, M. Nagamine, Y. Amenomori, T. Urushihara, and T. Itoh, SAE technical paper 2006-01-1202 (2006).-
149. T. Fujikawa, K. Fukui, Y. Hattori, and K. Akihama, SAE technical paper 2006-01-3336 (2006)
150. M.C. Thurber, R.K. Hanson, Exp. Fluids **30**, 93 (2001)
151. S. Einecke, C. Schulz, V. Sick, Appl. Phys. B **71**, 717 (2000)
152. M. Anbari Attar, M. R. Herfatmanesh, H. Zhao, and A. Cairns, Exp. Therm. Fluid Sci. 59, 96 (2014)
153. M. Löffler, K. Kröckel, P. Koch, F. Beyrau, A. Leipertz, S. Grasreiner, and A. Heinisch, SAE technical paper 2009-01-0656 (2009)
154. D.A. Rothamer, J.A. Snyder, R.K. Hanson, R.R. Steeper, S.A.E. Int, J. Fuels Lubr. **1**, 520 (2008)
155. S. Lind, J. Trost, L. Zigan, A. Leipertz, S. Will, Proc. Combust. Inst. **35**, 3783 (2015)
156. S. Lind, L. Zigan, J. Trost, A. Leipertz, S. Will, Int. J. Engine Res. **17**, 120 (2016)
157. R. G. Brown and D. Phillips, J. Chem. Soc. Faraday Trans. 2. **70**, 630 (1974)
158. R. Zhang and V. Sick, SAE technical paper 2007-01-1826 (2007)
159. R. E. Stevens, H. Ma, C. R. Stone, H. L. Walmsley, and R. Cracknell, Proc. Inst. Mech. Eng. Pt. D. 221, 713 (2007)
160. H. Krämer, S. Einecke, C. Schulz, V. Sick, S. R. Nattrass, and J. S. Kitching, SAE technical paper 982467 (1998)
161. W. Koban, J. Schorr, C. Schulz, Appl. Phys. B **74**, 111 (2002)
162. M. Bardi, A. Di Lella, G. Bruneaux, Fuel (Lond.) **239**, 521 (2019)
163. L.M. Itani, G. Bruneaux, A. Di Lella, C. Schulz, Proc. Combust. Inst. **35**, 2915 (2015)
164. M. Cordier, L. Itani, G. Bruneaux, Int. J. Engine Res. **21**, 185 (2020)
165. Q. Wang, Y. Zhang, L. Jiang, D. Zhao, Combust. Sci. Technol. **190**, 949 (2018)
166. S. Lind, S. Aßmann, L. Zigan, S. Will, Appl. Opt. **55**, 1551 (2016)
167. T. Benzler, T. Dreier, and C. Schulz, Appl. Phys. B **123**, (2017)
168. Q. Wang, Y. Zhang, L. Jiang, D. Zhao, P. Guibert, and S. Yang, Appl. Phys. B **123**, (2017)
169. T. Benzler, T. Endres, T. Dreier, and C. Schulz, Appl. Phys. B **124**, (2018)
170. J. Hult, M. Richter, J. Nygren, M. Aldén, A. Hultqvist, M. Christensen, B. Johansson, Appl. Opt. **41**, 5002 (2002)
171. J. Hult, Development of time resolved laser imaging techniques for studies of turbulent reacting flows, Lund University, 2002
172. C.F. Kaminski, J. Hult, M. Aldén, Appl. Phys. B **68**, 757 (1999)
173. M.D. Rosa, A.Y. Chang, R.K. Hanson, Appl. Opt. **32**, 4074 (1993)
174. A.Y. Chang, B.E. Battles, R.K. Hanson, Opt. Lett. **15**, 706 (1990)
175. N. Jiang, W.R. Lempert, Opt. Lett. **33**, 2236 (2008)
176. B.H. Cheung, R.K. Hanson, Appl. Phys. B **98**, 581 (2010)
177. B. Böhm, C. Heeger, R.L. Gordon, A. Dreizler, Appl. Sci. Res. **86**, 313 (2011)
178. C.M. Fajardo, J.D. Smith, V. Sick, Appl. Phys. B **85**, 25 (2006)
179. B. Peterson, V. Sick, Appl. Phys. B **97**, 887 (2009)
180. R.L. Gordon, C. Heeger, A. Dreizler, Appl. Phys. B **96**, 745 (2009)
181. M.J. Papageorge, T.A. McManus, F. Fuest, J.A. Sutton, Appl. Phys. B **115**, 197 (2014)
182. J.D. Miller, J.B. Michael, M.N. Slipchenko, S. Roy, T.R. Meyer, J.R. Gord, Appl. Phys. B **113**, 93 (2013)
183. M. Papageorge and J. A. Sutton, Exp. Fluids. **58**, 40 (2017)
184. M. Brusnahan, L. Lu, V. Sick, Appl. Phys. B **111**, 651 (2013)
185. M. F. Hushim, A. J. Alimin, H. Selamat, and M. T. Muslim, Int. J. Environ. Sci. Dev. 375 (2013)
186. D.B. Gohil, A. Pesyridis, J.R. Serrano, Appl. Sci. (Basel) **10**, 3604 (2020)
187. M. Mittal, D.L.S. Hung, G. Zhu, H.J. Schock, J. Vis. (Tokyo) **14**, 149 (2011)
188. J. V. Jose, M. Mittal, and A. Ramesh, SAE Int. J. Engines **14** (1), pp115:133 (2020)
189. J. King, L. Schmidt, J. Stokes, J. Seabrook, F. Nor, and S. Sahadan, in Internal combustion engines: improving performance, fuel economy and emission (Elsevier, 2011), pp. 13–26
190. S. Hemdal, M. Andersson, P. Dahlander, R. Ochoterena, I. Denbratt, Int. J. Engine Res. **12**, 549 (2011)
191. L. Schmidt, J. Seabrook, J. Stokes, M. F. Ahmad Zuhdi, S. Begg, M. Heikal, and J. King, SAE technical paper 2011-01-1228 (2011)
192. A. Alam, M. Mittal, and V. Lakshminarasimhan, SAE technical paper 2020-01-0793 (2020)
193. B. Williams, P. Ewart, X. Wang, R. Stone, H. Ma, H. Walmsley, R. Cracknell, R. Stevens, D. Richardson, H. Fu, S. Wallace, Combust. Flame **157**, 1866 (2010)
194. V. Ravaglioli, F. Ponti, G. Silvagni, D. Moro, F. Stola, and M. De Cesare, SAE technical paper 2022-01-0456 (2022)
195. Z. Wang, P. Stamatoglou, M. Lundgren, L. Luise, B.M. Vaglieco, A. Andersson, M. Aldén, Ö. Andersson, M. Richter, Proc. Combust. Inst. **37**, 4751 (2019)
196. M. Colket, J. Heyne, M. Rumizen, M. Gupta, T. Edwards, W.M. Roquemore, G. Andac, R. Boehm, J. Lovett, R. Williams, J. Condevaux, D. Turner, N. Rizk, J. Tishkoff, C. Li, J. Moder, D. Friend, V. Sankaran, AIAA J. **55**, 1087 (2017)
197. J. T. Edwards, in 55th AIAA Aerospace sciences meeting (American Institute of Aeronautics and Astronautics, Reston, Virginia, 2017)
198. D. Shin, A. Satija, R.P. Lucht, Exp. Therm. Fluid Sci. **130**, 110511 (2022)
199. Williams, B., Ewart, P., Stone, R., Ma, H. et al., SAE technical paper 2008-01-1073 (2008)
200. Y. Li, H. Zhao, B. Leach, T. Ma, and N. Ladommatos, SAE technical paper 2004-01-1354 (2004)
201. U. Retzer, H. Ulrich, S. Will, and L. Zigan, Appl. Phys. B **128**, 201 (2022)
202. J.D. Koch, R.K. Hanson, W. Koban, C. Schulz, Appl. Opt. **43**, 5901 (2004)
203. M. Berckmüller, N.P. Tait, D.A. Greenhalgh, SAE Tech. Pap. **96**, 1996 (1929)